

Department of Physics  
Indian Institute of Technology Guwahati  
Ph.D. Thesis



# Quantum dynamics of low dimensional interacting systems using the continuous-time quantum walk

Mrinal Kanti Giri

Thesis Supervisor: Dr. Tapan Mishra  
Nov, 2022



# Quantum dynamics of low dimensional interacting systems using the continuous-time quantum walk

A

Thesis Submitted

in Fulfillment of the Requirements

for the Degree of

PHD

By

**MRINAL KANTI GIRI**

Under the Supervision of **Dr. TAPAN MISHRA**



Department of Physics

Indian Institute of Technology Guwahati

Nov, 2022



# Declaration

This is to certify that the thesis entitled “**Quantum dynamics of low dimensional interacting systems using the continuous-time quantum walk**”, submitted by me to the *Indian Institute of Technology Guwahati*, for the award of the degree of PhD, is a bonafide work carried out by me under the supervision of Dr. Tapan Mishra. The content of this thesis, in full or in parts, have not been submitted to any other University or Institute for the award of any degree or diploma. Works presented in the thesis are all my own unless referenced to the contrary in the thesis.

Signed: **Mrinal Kanti Gisi**

---

Mrinal Kanti Giri  
Department of Physics,  
Indian Institute of Technology Guwahati,  
Guwahati-781039, Assam, India.

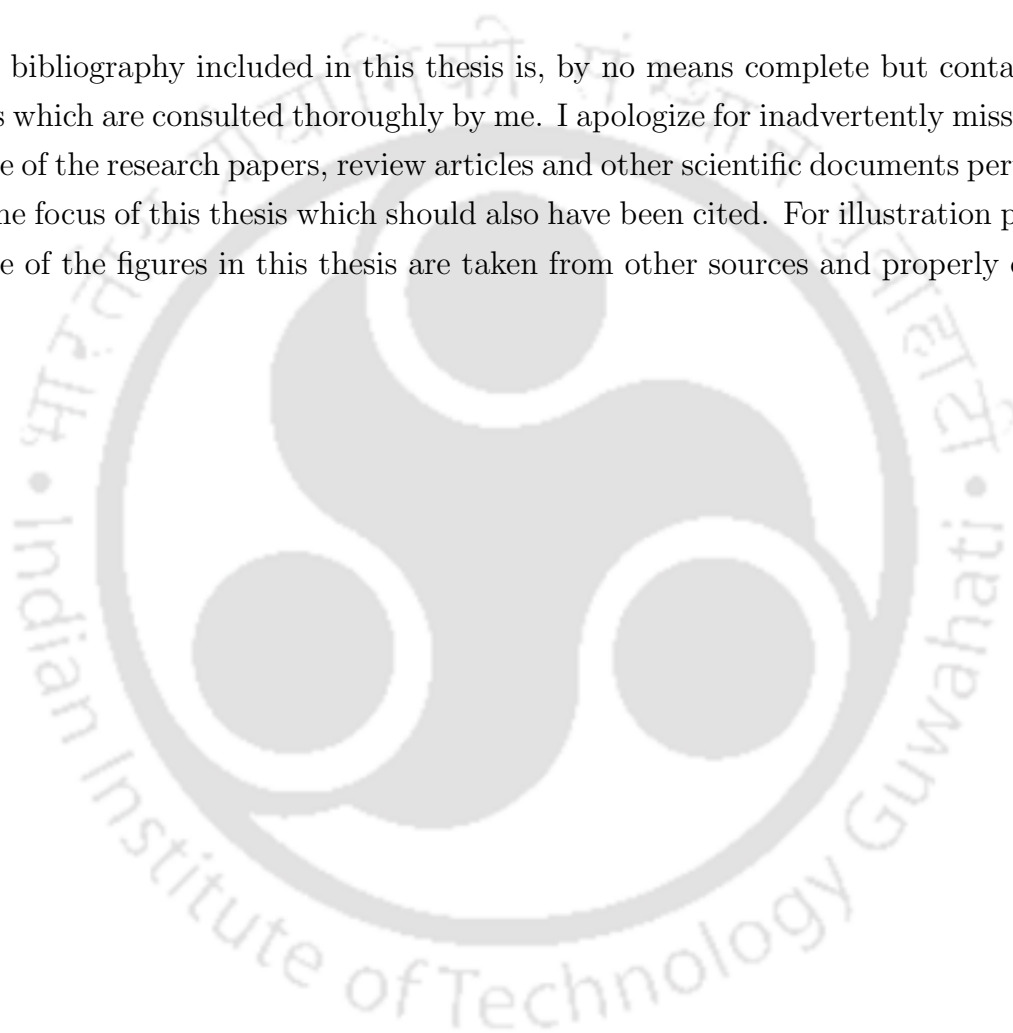
Date: **18/11/2022**

---



# Disclaimer

The bibliography included in this thesis is, by no means complete but contains the ones which are consulted thoroughly by me. I apologize for inadvertently missing out some of the research papers, review articles and other scientific documents pertaining to the focus of this thesis which should also have been cited. For illustration purpose some of the figures in this thesis are taken from other sources and properly cited.





# Certificate

This is to certify that the thesis entitled “**Quantum dynamics of low dimensional interacting systems using the continuous-time quantum walk**”, submitted by Mrinal Kanti Giri (186121015), a research scholar in the *Department of Physics, Indian Institute of Technology Guwahati*, for the award of the degree of PhD, is a record of an original research work carried out by him under my supervision and guidance. The thesis has fulfilled all requirements as per the regulations of the institute and in my opinion has reached the standard needed for submission. The results embodied in this thesis have not been submitted to any other University or Institute for the award of any degree or diploma.

Signed: \_\_\_\_\_

*Tapan Mishra*

**Supervisor: Dr. Tapan Mishra**  
**Department of Physics,**  
**Indian Institute of Technology Guwahati,**  
**Guwahati-781039, Assam, India.**

Date: **18/11/2022**



*“Where the mind is without fear and the head is held high;  
Where knowledge is free;  
Where the world has not been broken up into fragments by narrow domestic walls;  
Where words come out from the depth of truth;  
Where tireless striving stretches its arms towards perfection;  
Where the clear stream of reason has not lost its way into the dreary desert sand of  
dead habit;  
Where the mind is led forward by thee into ever-widening thought and action—  
Into that heaven of freedom, my Father let my country awake”*

**—Rabindranath Tagore**



*To my family*  
(“Maa”, “Papa” and “Sister”)

*To my all teachers...*





# Acknowledgement

I will infinitely be indebted to my supervisor Dr. Tapan Mishra for giving me an opportunity to explore this exciting field of research. His brilliant ideas and continual supervision have always helped me to progress with my thesis work. I have always revered his punctuality and sincerity towards diversified research. He always tries to make me independent in research. Besides all this professional work, he also helps me to build my character and how to deal with tough times. However, if I get a chance to choose my supervisor by moving four years back, I will approach him again with a better version of me, being more punctual and attentive.

I am grateful to the doctoral committee members, Dr. Kanhaiya Pandey, Dr. Pankaj Mishra, and Prof. Aditya Narayan Panda, for reviewing my progress every year and their unblocked directive and valuable suggestions.

I want to thank Prof. Bhanupratap Das, one of our collaborators, for his immense and valuable input into my work.

I want to present my gratitude to all other faculty members and the HoDs of the Physics department for their gracious behavior. A major thanks to the faculty members for their excellent teaching during my M.Sc (2016- 2018) and motivating me to pursue Ph.D at IIT, Guwahati. Especially I would like to thank Prof. Subhradip Ghosh, Prof. Sourabh Basu, Prof. Santabrata Das, Prof. U.N Maity, Dr. Subhaditya Bhattacharya, Dr. Debaprasad Maity and Dr. Pankaj Mishra for their consistent backing.

I am also thankful to Basab B Purakayastha, Hemanta Medhi, Mridupawan, Aditya Kalita, and all technical team members of the department for their support.

Thanks to Suman da and Sayan da, with whom I've worked extensively and I've learned many things. I also thankful to them for their consistent motivation, guidance and encouragement. I will miss your companion. It was a great pleasure to work with my research lab members Ashirbad da, Soumya, Rajashri, and Biswajit for their discussions, suggestions, time, kindness, and tolerance towards me throughout my Ph.D.

---

I want to thank my school friend Supriya for his forever support. My Special thanks go to Krishnendu Dandapat, Chayanika Sarkar, and Shirshendu Nanda (friend cum listener) for their assistance and support from B.Sc till now.

Thanks to my B.Sc. friends, Rabi, Santanu, Suryakanta, and Snehasis, for being my first and foremost fun companion in Midnapore.

Thanks to my M.Sc. friends Chandan, Chiranjit, Atanu, Shubhendu, Arnob, Chitrak, Jonmani, and Upasana for being my first and foremost fun companion on this campus.

I feel myself blessed for having my beloved friend Sudeshna in my life. I want to thank her for continuous support at every moment of my life and tolerating my unnecessary stubbornness. Besides her research work, she also helps me a lot by bringing my lunch, checking student copies, correcting my English, and many more so that I can give more time to my research work.

Special thanks to Shilpi di for supporting, motivating, and encouraging me like an elder sister whenever I needed.

Special thanks to Sumana di, Debabrata Majhi, Shantanu, Chinmoy, Dipankar, Sheshadri, Lipika, and others for boosting the fun factor in every moment in the lab and “Khoka tea stall”.

Special thanks to Sayan, my PUBG partner, who always protects me in the reel Battleground.

I am deeply thankful to all my seniors, friends, and juniors at IIT Guwahati; Joydip Da, Nagendra Da, Surojit Da, Sanket Da, Riazul Da, Rajesh Da, Arghyajit Da, Rony Da, Abhisek Da, Kajal Da, Sayandeep Da, Pronoy Da, Parth Da, Golam, Rajnandan, Debu, Angana, Nikhil, Sahabub, Sourav, Sumit, Monu, Suruj, Pushpesh, Pushpa, Mandira, Prantik, Tarik, Sashi, Akanshu, Shubhangi, Ravi, Sahona, Sampreet, Banashree, Sonali, Samik, Swarup, Himangshu, Mijanur, Sunil, Likun, Ankan, Arka, Himansu, Swargiary, Sanu, Shalini, Shilpa, Sirsendu, Utsab, Harekrushna, Sanjib, Dipendu, Nayan, Sourav, Shubankar and others for providing a soothing environment.

Thanks to all the RS-4 lab members for the tolerance and support.

I am grateful to all my family members, parents, and sister for their love and encouragement during my entire academic career. No word is enough to express their love and constant support throughout my endeavor.

Finally, I would like to thank the MHRD, Govt. of India, for providing Scholarship and financial support to carry out the present thesis work.

–Mrinal

# Abstract

The quantum walk (QW) is the quantum analog of the classical random walk where an initial state undergoes reversible, unitary time evolution leading to a dynamical evolution of the quantum states. The study of QW has attracted a great deal of attention in recent years, not only in the context of studying the dynamical properties of quantum systems but also due to its possible application in quantum technologies. Numerous studies have been performed theoretically and experimentally to investigate the QW of single and two interacting particles using various systems.

In this thesis, we theoretically study the QW of interacting particles in the framework of the two-component Bose-Hubbard model in one-dimensional lattices. In the first part of the thesis, we explore the QW of two-component hardcore bosons / spinless fermions with hopping imbalance. We show that the hopping imbalance and interaction play an essential role in exhibiting exciting phenomena for different initial states, such as the formation of repulsively bound pairs, reflection and transmission of the wavefunction, etc.

Further, we study the QW of interacting two-component bosons with hopping imbalance. In this case, we show the fascinating phenomenon of onsite bound pair formation of two different species which start their QW from the nearest neighbour sites. We also predict the existence of non-trivial three-particle bound state and nearest neighbour pairs.

In the final part of the thesis, we study the QW of interacting bosons in a Harper-Hofstadter ladder. We explore the chiral dynamics in the single- and two-particle QW by considering uniform and staggered flux threading the ladder. We show that the uniform flux facilitates a chiral motion which disappears in the presence of the staggered flux. On the other hand, we find that the staggered flux significantly affects the spreading of the particle's wavefunction both for single and two-particle QW. We further analyse the effect of flux on the bound state formation.

These studies are carried out using the exact diagonalization and the time-evolving block decimation methods.



# List of Publications

## Publications included in the thesis

1. **Mrinal Kanti Giri**, Suman Mondal, Bhanu Pratap Das, Tapan Mishra, *Two component quantum walk in one-dimensional lattice with hopping imbalance*, Scientific Reports **11**, 22056 (2021).
2. **Mrinal Kanti Giri**, Suman Mondal, Bhanu Pratap Das, Tapan Mishra, *Signatures of non-trivial pairing in the quantum walk of two-component bosons*, Phys. Rev. Lett. **129**, 050601 (2022).
3. *Quantum walk of interacting bosons in Harper-Hofstadter ladder*, To be submitted.

## Publications outside thesis

4. Ashirbad Padhan, **Mrinal Kanti Giri**, Suman Mondal, Tapan Mishra, *Emergence of multiple localization transitions in a one-dimensional quasiperiodic lattice*, Phys. Rev. B **105**, L220201 (2022).

## Schools/Workshops/Conferences attended

1. Attended *Recent Trends in Cold and Ultracold Matter*, March 2018, Department of Physics, IIT Guwahati, India.
2. Attended *2nd Annual conference on quantum condensed matter*, July 2019, Department of Physics, IISc Bangalore, India.
3. Attended *Novel Phases of Quantum Matter*, December 2019, ICTS Bangalore, India.
4. Attended and presented poster at, *Fundamental Sciences & Quantum Technologies using Atomic Systems*, September 2020, PRL, India.
5. Attended *Online School and discussion meeting on trapped atoms, molecules and ions*, April 2021, ICTS Bangalore, India.
6. Attended *Bangalore school on statistical physics -XII (Online)*, July 2021, ICTS Bangalore, India.
7. Attended *Annual conference on quantum condensed matter (QMAT 2022)*, Sept 2022, IIT Kanpur, India.
8. Attended *"Young Investigators Meet on Quantum Condensed Matter Theory-2022" (YIMQCMT-2022)*, Oct 2022, NISER, India.

# Contents

List of publications	xv
<b>1 Introduction</b>	<b>1</b>
1.1 Quantum Walk (QW)	1
1.1.1 Discrete-time QW (DTQW)	2
1.1.2 Continuous-time QW (CTQW)	5
1.2 Distribution of the CTQW and CTRW in one-dimension	8
1.3 Multi-particle QW	11
1.4 Experimental observations	13
1.4.1 Optical lattice	13
1.4.2 Tight-binding regime	14
1.5 Chapter-wise outline of the thesis	21
<b>2 Numerical methods</b>	<b>23</b>
2.1 Exact Diagonalization	23
2.1.1 Construction of basis	24
2.1.2 Construction of Hamiltonian matrix	25
2.2 Time-evolving block-decimation (TEBD)	27
2.2.1 Matrix Product State (MPS)	27
2.2.2 Implementation of the TEBD method	30
<b>3 Two-component quantum walk in one-dimensional lattice with hopping imbalance</b>	<b>33</b>
3.1 Model and approach	34
3.2 Results	35
3.2.1 Two particles at the same site	35
3.2.2 Two particles at two different sites	40
3.2.2.1 Density evolution	41

## CONTENTS

---

3.2.2.2	Correlation function . . . . .	45
3.2.2.3	Effect of distance . . . . .	45
3.2.2.4	Transmission coefficient . . . . .	48
3.3	Conclusions . . . . .	49
<b>4</b>	<b>Signatures of non-trivial pairing in the quantum walk of two-component bosons</b>	<b>51</b>
4.1	Introduction . . . . .	51
4.2	Model . . . . .	52
4.3	Two $\uparrow$ and one $\downarrow$ particles . . . . .	54
4.4	One $\uparrow$ and two $\downarrow$ particles . . . . .	58
4.5	Two $\uparrow$ and two $\downarrow$ particles . . . . .	61
4.6	Repulsive $U$ and attractive $U_{\uparrow\downarrow}$ . . . . .	67
4.6.1	Two $\uparrow$ and one $\downarrow$ particles . . . . .	67
4.6.2	Two $\uparrow$ and two $\downarrow$ particles . . . . .	67
4.7	Conclusions . . . . .	68
<b>5</b>	<b>Quantum walk of interacting bosons in Harper-Hofstadter ladder</b>	<b>71</b>
5.1	Introduction . . . . .	71
5.2	Model . . . . .	73
5.3	Results . . . . .	75
5.3.1	Single-particle Quantum walk . . . . .	75
5.3.2	Two-particle Quantum Walk . . . . .	81
5.4	Effect on Repulsively Bound Pairs . . . . .	88
5.5	Conclusion . . . . .	92
<b>6</b>	<b>Summary and Outlook</b>	<b>93</b>
6.1	Outlook . . . . .	95
	<b>Bibliography</b>	<b>97</b>

# List of Figures

1.1	In classical random walk, (a) the walker continues walking through an iterative process. (b) After many iterative processes, the walker traces out a single path (black line) on a decision tree. . . . .	3
1.2	In quantum walk, (a) the walker continues walking through an iterative process. (b) In quantum walk, the walker moves simultaneously to the left and to the right with complex amplitude without measuring the outcome of the coin in each step. After many iterations, there is a finite probability of the walker to be present everywhere. . . . .	4
1.3	The figure shows the decision tree with 4 nodes indexed as $i = 0, 1, 2$ and 3. The transition probabilities in different nodes are shown here.	5
1.4	The figure shows the pictorial representation of the CTQW on a one-dimensional node. (a) The CTQW takes place on discrete nodes. (b) The CTQW takes place on a continuous line, where the width ( $\Delta x$ ) of the walker does not overlap with each other. (c) The CTQW takes place on a continuous space, where the width ( $\Delta x$ ) of the walker overlaps with each other. . . . .	8
1.5	The figure shows a quantum walker walking on a 1d lattice. . . . .	9
1.6	The figure shows the probability distribution of the classical random walk (black line) and quantum walk (red line) in 1d after 50 steps. . .	12
1.7	The figure shows the Bose-Hubbard model. The nearest-neighbour hopping amplitude is $J$ and on-site interaction is $U$ when two particles resides at the same site. . . . .	14
1.8	The figure shows the particle distribution in (a) SF and (b) MI state.	14

- 1.9 Absorption images of multiple matter wave interference patterns. These were obtained after suddenly releasing the atoms from an optical lattice potential with different potential depths  $V_0$  after a time of flight of 15 ms. Values of  $V_0$  were: a,  $0E_r$ ; b,  $3E_r$ ; c,  $7E_r$ ; d,  $10E_r$ ; e,  $13E_r$ ; f,  $14E_r$ ; g,  $16E_r$ ; and h,  $20E_r$ . In superfluid regime, atoms are delocalized throughout the lattice with equal phases between the different sites and obtained high-contrast three dimensional interference pattern as expected for a periodic array of phase coherent matter wave sources. In Mott insulator regime, atoms are tightly localized at each sites, as a result there no phase coherence and no interference occurs. This picture has been taken from [1]. . . . . 15
- 1.10 (a) A state with two atoms located on the same site of an optical lattice has an energy offset  $\sim U$  with respect to states where the atoms are separated. (b) Due to lattice band structure and energy conservation restrict the atom pairs to break up as individual atoms. The atoms will remain together and tunnel through the lattice as a bound composite object. (c) Long lifetime of repulsively bound atom pairs that are held in a 3d optical lattice. For repulsive interaction ( $a_s = 100a_0$ ), the atom pair exhibits the remarkably long lifetime (open diamond). On turning off the on-site interaction by tuning the scattering length near zero ( $a_s \sim 0a_0$ ), it observed a much faster decay in the number of doubly occupied sites showing the the rapid diffusion of unbound atoms through the lattice (filled circles). This picture has been taken from [2] . . . . . 17
- 1.11 The figure shows the single-particle and two-particle QW in a one-dimensional lattice of length  $L = 21$ . (I) The density evolution of the single particle. (II) the density evolution of the two non-interacting particles placed at the same site. (III) The density evolution of the two-particle with onsite interaction  $U = 10$  place at the same site. . . 18

1.12	The Figure shows the two-particle correlations $\Gamma_{i,j}$ during the evolution of the two-particle QW placed at the same site. The two particles perform as independent single-particle quantum walk for weak interactions ( $U = 0.7J$ ). The corresponding two-particle correlation is the direct product of the single-particle densities. On increasing interaction strength, repulsively bound pairs form and two particles move as a composite object which can be reflected from the finite diagonal elements of the correlation matrix. This picture has been taken from [3].	19
1.13	The figure shows the HBT interference and fermionization when two bosons start the QW from the two nearest-neighbour sites. (I) For weak interaction, $U = 0.7J$ , the correlation shows the spatial bunching of the bosons indicating that two bosons have tendency to stay close to each other. (II) Strong on-site interaction, $U = 5.1J$ , fermionize the bosons in one-dimension display the anti-bunching in correlation, indicating that the two atoms repel each other. This picture has been taken from [3].	20
2.1	The graphical representation of the left canonical MPS formation using SVD process for a system of length $L = 5$ .	28
2.2	The figure shows the graphical representation of “A” matrices at the ends and in the bulk of the chain for a system of length $L = 5$ . The left diagram represents $A_{i_1}^{n_1}$ , the row vector at the left of the MPS end, the right diagram represents $A_{i_4}^{n_5}$ , the column vector at the right end of the MPS. The center diagram represents $A_{i_2,i_3}^{n_3}$ .	29
2.3	The graphical representation of the TEBD1 (first order) algorithm for a quantum lattice system of 5 sites with nearest neighbour interactions for a small time ( $\delta t$ ). The corresponding Hamiltonian $\hat{H}$ can be written as, $\hat{H} = \hat{H}_{even} + \hat{H}_{odd}$ where $\hat{H}_{even} = \hat{h}_{2,3} + \hat{h}_{4,5}$ and $\hat{H}_{odd} = \hat{h}_{1,2} + \hat{h}_{3,4}$ . The even and odd numbered two-site local time evolution operators are alternatively applied to the wave function represented by a matrix product state (MPS).	31
2.4	The figure shows a key step in TEBD1 is the contraction of a two site time-evolution operator into a pair of MPS tensors and splitting back into a new pair of MPS tensors with smaller singular values.	32
3.1	The schematic description of the initial state given in Eq. 3.5.	35

3.2	The figure shows the QW of two particles with the initial state given in Eq. 3.5 and $\delta = 0.2$ . (a) Shows the time evolution of the normalized on-site density for different values of $U$ . (b) Shows the normalized correlation functions $\Gamma_{ij}$ at time $t = 7J^{-1}$ , which correspond to the dashed lines in (a). (c) and (d) shows the on-site density evolution of $\uparrow$ particle and $\downarrow$ particle respectively corresponding to the QW shown in (a). . . . .	36
3.3	(a) $R(t)$ and (b) $v(t)$ are plotted for $U = 0, 2$ and $10$ corresponding to the expansion of the wave function of $\uparrow$ particle when $\delta = 0.2$ . . .	37
3.4	The figure shows the time evolution of $S_A(t)$ for $U = 0, 2, 5, 10, 20, 50$ . 38	
3.5	Figure shows the behaviour of (a) $P$ and (b) $SDI$ as a function of $U$ for different $\delta$ after a time evolution of the initial state given in Eq. 3.5 up to $t = 7J^{-1}$ . . . . .	39
3.6	(a), (b) and (c) depict the schematic description of the initial states given in Eq. 3.11, Eq. 3.12 and Eq. 3.13 respectively. . . . .	41
3.7	Figure shows the QWs for different initial states and different values of $U$ . Here (a), (b) and (c) depict the total density (normalized) evolution for the three initial states Eq. 3.11, Eq. 3.12 and Eq. 3.13 respectively. For results depicted in (a) and (b) $\delta = 0.2$ and for (c) $\delta = 0.4$ has been considered. . . . .	42
3.8	The figure shows the time evolution of $P$ for different values of $\delta$ and (a) for $U = 0$ , (b) for $U = 2$ and (c) for $U = 10$ . . . . .	42
3.9	Figure shows the onsite densities of $\downarrow$ (dashed curves) and $\uparrow$ particle (solid curves) in the lattice for different regimes of interaction such as small (I), intermediate (II) and large (III) after evolving the initial state up to a certain time ( $t$ ). (a-d) correspond to the initial states given in Eq. 3.5, Eq. 3.11, Eq. 3.12 and Eq. 3.13 respectively. For (a-c) $t = 7J^{-1}$ , $\delta = 0.2$ and for (d) $t = 20J^{-1}$ , $\delta = 0.4$ are considered. . . . .	43
3.10	Evolution of half-length occupation $N_{\frac{L}{2},\uparrow}$ (dashed curves) and $N_{\frac{L}{2},\downarrow}$ (solid curves) are shown for different interaction strengths such as $U = 0$ (circles), $U = 2$ (triangles) and $U = 10$ (squares). (a), (b) and (c) correspond to the initial states given in Eq. 3.11, 3.12 and 3.13 respectively. For (a-b) $\delta = 0.2$ and for (c) $\delta = 0.4$ is considered. . . . .	44

- 3.11 Normalized correlation functions  $\Gamma_{ij}$  are plotted corresponding to the parameters considered in Fig. 3.7 at a particular instant during the time evolution.  $\Gamma_{ij}$  in (a), (b) and (c) correspond to the initial states of Eq. 3.11, Eq. 3.12 and Eq. 3.13 respectively. While  $\Gamma_{ij}$  is computed at  $t = 7J^{-1}$  for (a) and (b), for (c) it is computed at  $t = 20J^{-1}$ . . . . . 46
- 3.12 (a)  $I_P$  and  $\frac{dI_P}{dt}$  are plotted with respect to time. Black dashed line represents the time at which  $\frac{dI_P}{dt}$  is maximum. Here we consider the initial state  $|\Psi_0\rangle = a_{-14,\uparrow}^\dagger a_{14,\downarrow}^\dagger |vac\rangle$  and  $\delta = 0.2$ . (b) The point of contact is shown by plotting  $\langle n_{i,\uparrow} n_{i,\downarrow} \rangle$  with respect to the site at different times. The time  $t = 12.28J^{-1}$  corresponds to the black dashed line of (a). (c) Point of contact of the two-particle wave functions are plotted with different  $d$  of the initial state  $|\Psi_0\rangle = a_{-d,\uparrow}^\dagger a_{d,\downarrow}^\dagger |vac\rangle$ . The red squares and blue circles are the data for  $\delta = 0.2$  and  $0.6$ , respectively. The dashed lines are the fitted functions. . . . . 47
- 3.13 The transmission coefficient  $T$  is plotted with respect to  $U$  for different values of  $\delta$  by evolving the initial state  $|\Psi(0)\rangle$  to (a)  $t = 7J^{-1}$ , (b)  $t = 7J^{-1}$  and (c)  $t = 23J^{-1}$ . (a), (b) and (c) correspond to the results obtained using the initial states given in Eq. 3.11, Eq. 3.12 and Eq. 3.13 respectively. . . . . 48
- 3.14 (a) The transmission coefficient  $T$  is plotted as a function of  $U$  for different values of  $\delta$  in the log-log scale for the initial state given in Eq. 3.13 at  $t = 23J^{-1}$ . The dashed line marks  $T = 10^{-2}$  which is considered as the critical  $T$  for zero transmission and its point of intersection with different curves are the corresponding  $U_c$ . (b) The plot between  $U_c$  and  $\delta$  is obtained by evolving the initial states given in Eq. 3.11 to  $t = 7J^{-1}$  (red stars), Eq. 3.12 to  $t = 7J^{-1}$  (blue squares) and Eq. 3.13 to  $t = 23J^{-1}$  (magenta diamonds). . . . . 49
- 4.1 The lattice diagrams (a), (b) and (c) represent the initial state  $|\Psi(0)\rangle_I = a_{0,\uparrow}^\dagger a_{1,\downarrow}^\dagger |vac\rangle$ ,  $|\Psi(0)\rangle_{II} = a_{0,\uparrow}^\dagger a_{1,\downarrow}^\dagger |vac\rangle$  and  $|\Psi(0)\rangle_{III} = a_{0,\uparrow}^\dagger a_{1,\downarrow}^\dagger |vac\rangle$ , respectively. . . . . 53
- 4.2 Panel (a) shows the onsite density evolution with the initial state  $|\Psi(0)\rangle_I$  for (I)  $U_{\uparrow\downarrow} = 0J_\uparrow$ , (II)  $U_{\uparrow\downarrow} = 5J_\uparrow$ , (III)  $U_{\uparrow\downarrow} = 10J_\uparrow$  and (IV)  $U_{\uparrow\downarrow} = 20J_\uparrow$ . Panel (b) and (c) show the correlation functions  $\Gamma_{ij}^{\downarrow\uparrow}$  and  $\Gamma_{ij}^\uparrow$ , respectively. Here  $U = 10J_\uparrow$  and  $\delta = 1$  are considered and the correlation functions are plotted at  $t = 5J_\uparrow^{-1}$ . . . . . 54

- 4.3 Panel (a) shows the normalised density evolution of the initial state  $|\Psi_0\rangle = a_{0,\uparrow}^{\dagger 2} a_{1,\downarrow}^{\dagger} |vac\rangle$  for  $U_{\uparrow\downarrow} = 0J_{\uparrow}, 5J_{\uparrow}, 10J_{\uparrow}$  and  $20J_{\uparrow}$ . Here  $U = 10J_{\uparrow}$  and  $\delta = 0.2$ . Panel (b) and (c) show the correlation functions  $\Gamma_{ij}^{\downarrow\uparrow}$  and  $\Gamma_{ij}^{\uparrow}$  respectively at time,  $t = 5J_{\uparrow}^{-1}$ . . . . . 56
- 4.4 Panel (a) and (b) show the normalised density evolution of  $n_{\uparrow}$  and  $n_{\downarrow}$ , respectively for  $U_{\uparrow\downarrow} = 0J_{\uparrow}, 5J_{\uparrow}, 10J_{\uparrow}$  and  $20J_{\uparrow}$ . Here  $U = 10J_{\uparrow}$  and  $\delta = 0.2$ . . . . . 57
- 4.5 (a)  $P_{\uparrow\downarrow}$  (red circles) and  $P_{\uparrow\uparrow}$  (blue squares) are plotted against  $U_{\uparrow\downarrow}/J_{\uparrow}$  for  $\delta = 1$  (dashed curve) and  $\delta = 0.2$  (solid curve) at  $t = 10J_{\uparrow}^{-1}$ . (b) Shows the time evolution of  $P_{\uparrow\downarrow}$  (red circles) and  $P_{\uparrow\uparrow}$  (blue squares) for  $\delta = 0.2$  and  $U_{\uparrow\downarrow} = 10J_{\uparrow}$  indicating complete inter-component pair formation and breaking up of  $\uparrow\uparrow$  pair. (Inset) The time evolution of  $P_{\uparrow\downarrow}$  for different  $\delta$  such as  $\delta = 0.2$  (red circles),  $\delta = 0.4$  (green squares) and  $\delta = 1$  (black stars). . . . . 58
- 4.6 Panel (a) shows the normalised density evolution of the initial state  $|\Psi_0\rangle_{II} = a_{0,\uparrow}^{\dagger} a_{1,\downarrow}^{\dagger 2} |vac\rangle$  for  $U_{\uparrow\downarrow} = 0J_{\uparrow}, 5J_{\uparrow}, 10J_{\uparrow}$  and  $20J_{\uparrow}$ . Here  $U = 10J_{\uparrow}$  and  $\delta = 0.2$ . In Panel (b) and (c) are shown the correlation functions  $\Gamma_{ij}^{\downarrow\uparrow}$  and  $\Gamma_{ij}^{\downarrow}$  respectively at time,  $t = 5J_{\uparrow}^{-1}$ . . . . . 59
- 4.7 Panel (a) and (b) show the normalised density evolution of  $n_{\uparrow}$  and  $n_{\downarrow}$ , respectively for  $U_{\uparrow\downarrow} = 0, 5, 10$  and  $20$ . Here  $U = 10$  and  $\delta = 0.2$ . . . 60
- 4.8 (a)  $P_{\uparrow\downarrow}$  (circles) and  $P_{\downarrow\downarrow}$  (squares) against  $U_{\uparrow\downarrow}/J_{\uparrow}$  for  $\delta = 1$  (dashed curve) and  $\delta = 0.2$  (solid curve) at  $t = 10J_{\uparrow}^{-1}$ . (b) Shows the time evolution of  $P_{\uparrow\downarrow}$  (circles) and  $P_{\downarrow\downarrow}$  (squares) for different  $\delta = 0.2$  and  $U_{\uparrow\downarrow} = 10J_{\uparrow}$  indicating that there are no inter-component pair formation and dissociation of  $\downarrow\downarrow$  pair. (Inset) The time evolution of  $P_{\uparrow\downarrow}$  for different  $\delta$  such as  $\delta = 0.2$  (circle),  $\delta = 0.4$  (square) and  $\delta = 1$  (star). . . 60
- 4.9 Panel (a) shows the density evolution of the initial state  $|\Psi_0\rangle = a_{0,\uparrow}^{\dagger 2} a_{1,\downarrow}^{\dagger 2} |vac\rangle$  for  $U_{\uparrow\downarrow} = 0J_{\uparrow}, 2J_{\uparrow}, 5J_{\uparrow}, 8J_{\uparrow}, 10J_{\uparrow}$  and  $20J_{\uparrow}$ . Here  $U = 10J_{\uparrow}$  and  $\delta = 0.2$ . Panel (b) shows the correlation functions  $\Gamma_{ij}^{\downarrow\uparrow}$  at time,  $t = 10J_{\uparrow}^{-1}$ . . . . . 61
- 4.10 Panel (a) and (b) show the density evolution of  $n_{\uparrow}$  and  $n_{\downarrow}$ , respectively for  $U_{\uparrow\downarrow} = 0J_{\uparrow}, 2J_{\uparrow}, 5J_{\uparrow}, 8J_{\uparrow}, 10J_{\uparrow}$  and  $20J_{\uparrow}$ . Here  $U = 10J_{\uparrow}$  and  $\delta = 0.2$ . 62
- 4.11 Panel (a) shows the density evolution of the initial state  $|\Psi_0\rangle = a_{0,\uparrow}^{\dagger 2} a_{1,\downarrow}^{\dagger 2} |vac\rangle$  for  $U_{\uparrow\downarrow} = 0J_{\uparrow}, 2J_{\uparrow}, 5J_{\uparrow}, 8J_{\uparrow}, 10J_{\uparrow}$  and  $20J_{\uparrow}$ . Here  $U = 10J_{\uparrow}$  and  $\delta = 1.0$ . Panel (b) shows the correlation functions  $\Gamma_{ij}^{\downarrow\uparrow}$  at time,  $t = 10J_{\uparrow}^{-1}$ . . . . . 62

- 4.12 Figure shows (a)  $\langle n_i \rangle$ , (b)  $\Gamma_{ij}^{\downarrow\uparrow}$  and (c)  $\Gamma_{ij}^{\downarrow}$  for the QWs with the initial state  $|\Psi(0)\rangle_{\text{II}}$  for  $U_{\uparrow\downarrow} = 5J_{\uparrow}$ ,  $U = 10J_{\uparrow}$  and  $\delta = 0.2$  at  $t = 10J_{\uparrow}^{-1}$ . (d-f) Show the values of  $\Gamma_{ij}^{\uparrow}$ ,  $\Gamma_{ij}^{\downarrow}$  and  $\Gamma_{ij}^{\downarrow\uparrow}$ , respectively for  $U_{\uparrow\downarrow} = 10J_{\uparrow}$  at  $t = 17J_{\uparrow}^{-1}$ . (g) Shows the behavior of  $P_{\uparrow\downarrow}$  (red circles),  $P_{\uparrow\uparrow}$  (blue squares) and  $P_{\downarrow\downarrow}$  (black diamond) as a function of  $U_{\uparrow\downarrow}$  at  $t = 10J_{\uparrow}^{-1}$ . The time evolution of  $P$ 's are plotted in (h) and (i) for  $U_{\uparrow\downarrow} = 5J_{\uparrow}$  and  $10J_{\uparrow}$ , respectively with  $L = 82$  sites. . . . . 63
- 4.13 (a)  $P_{\uparrow\downarrow}$  (red circles),  $P_{\uparrow\uparrow}$  (blue squares) and  $P_{\downarrow\downarrow}$  (black diamonds) against  $U_{\uparrow\downarrow}$  for  $\delta = 1$  at  $t = 10J_{\uparrow}^{-1}$ . (b) Shows the time evolution of  $P_{\uparrow\downarrow}$  (red circles),  $P_{\uparrow\uparrow}$  (blue squares) and  $P_{\downarrow\downarrow}$  (black diamonds) for  $U_{\uparrow\downarrow} = 5J_{\uparrow}$  indicating the formation of inter-component pair and dissociation of  $\downarrow\downarrow$  pair. (c) The time evolution of  $P_{\uparrow\downarrow}$  (red circles),  $P_{\uparrow\uparrow}$  (blue squares) and  $P_{\downarrow\downarrow}$  (black diamonds) for  $U_{\uparrow\downarrow} = 10J_{\uparrow}$ . . . . . 64
- 4.14 Figure shows  $P_{\uparrow\downarrow}$  as a function of  $t(J_{\uparrow}^{-1})$  (a), and  $tJ_{\downarrow}$  (b) for different  $\delta$  with  $U_{\uparrow\downarrow} = U_{\uparrow} = U_{\downarrow} = 10J_{\uparrow}$ . . . . . 65
- 4.15  $\Gamma_{ij}^{\downarrow\uparrow}$ ,  $\Gamma_{ij}^{\uparrow}$  and  $\Gamma_{ij}^{\downarrow}$  are plotted at time  $t = 70J_{\uparrow}^{-1}$  for  $U_{\uparrow\downarrow} = U = 10J_{\uparrow}$  and  $\delta = 1$ . . . . . 66
- 4.16 Panel (a) shows the density evolution of the initial state  $|\Psi_0\rangle = a_{0,\uparrow}^{\dagger 2} a_{1,\downarrow}^{\dagger} |vac\rangle$  for  $U_{\uparrow\downarrow} = 0J_{\uparrow}$ ,  $-5J_{\uparrow}$ ,  $-10J_{\uparrow}$  and  $-20J_{\uparrow}$ . Here  $U = 10J_{\uparrow}$  and  $\delta = 0.2$ . In Panel (b) and (c) are shown the correlation functions  $\Gamma_{ij}^{\downarrow\uparrow}$  and  $\Gamma_{ij}^{\uparrow}$  respectively at time,  $t = 5J_{\uparrow}^{-1}$ . . . . . 68
- 4.17 Panel (a) shows the density evolution of the initial state  $|\Psi_0\rangle = a_{0,\uparrow}^{\dagger 2} a_{1,\downarrow}^{\dagger 2} |vac\rangle$  for  $U_{\uparrow\downarrow} = 0J_{\uparrow}$ ,  $-2J_{\uparrow}$ ,  $-5J_{\uparrow}$ ,  $-8J_{\uparrow}$ ,  $-10J_{\uparrow}$  and  $-20J_{\uparrow}$ . Here  $U = 10J_{\uparrow}$  and  $\delta = 0.2$ . Panel (b) shows the correlation functions  $\Gamma_{ij}^{\downarrow\uparrow}$  at time,  $t = 10J_{\uparrow}^{-1}$ . . . . . 69
- 5.1 The figure describes the two component bosons in one dimensional lattice resembling to a two-leg Bose-Hubbard ladder. . . . . 72
- 5.2 Schematic diagram depicting two-leg Bose-Hubbard ladder in the presence of (a) uniform flux and (b) staggered flux. . . . . 73
- 5.3 The figure shows the single-particle QW in the two-leg ladder system of length  $L = 41$ . Panel (a) and (b) correspond to the uniform and staggered flux, respectively. Here we consider  $J = 1$  and  $K = 3$ . . . . . 75

LIST OF FIGURES

---

5.4 The figure shows the radius of propagation  $R_n(t)$  in the presence of the uniform (dashed line) and staggered (solid line) flux in a two-leg ladder system of length  $L = 41$ . Here we consider  $J = 1$  and  $K = 3$ . . . . . 76

5.5 The figure shows the dispersion curve for different  $\phi$  values. Figures (a) and (b) correspond to the uniform and staggered flux, respectively. Here we consider  $J = 1$  and  $K = 3$ . . . . . 77

5.6 The figure shows the single-particle QW in the presence of (a) the uniform flux and (b) the staggered flux. Left: In the uniform flux, chiral motion is present in QW. Right: In the staggered flux, chiral motion is absent in QW. . . . . 77

5.7 This figure shows the chirality defined in Eq. 5.6. (a)-(b) correspond to the uniform flux case and (c)-(d) corresponds to the staggered flux case. Here we consider  $J = 1$ ,  $K = 3$  and flux values  $\phi = (0.3\pi, 0.5\pi)$ . 78

5.8 The figures show the chirality of the Bloch bands. The dispersion relations of the two Bloch bands are plotted for  $J = 1$  and  $K = 3$ . (a)-(b) correspond to the uniform flux, and (c)-(d) corresponds to the staggered flux. The color code indicates the chirality  $C(k)$  of the two bands. For each case we have considered  $\phi = 0.3\pi$  and  $\phi = 0.5\pi$ . . . . . 79

5.9 The figure shows the evolution of  $n_a$  and  $n_b$  defined in Eq. 5.8. (a) and (b) correspond to  $\phi = 0.3\pi$  and  $0.5\pi$ , respectively. The symbols are for staggered flux case and the black dashed line is for uniform flux case. Here we consider  $J = 1$  and  $K = 3$ . . . . . 80

5.10 Figures (a) and (c) show the density evolution of leg-a and leg-b in the presence of the uniform flux, respectively. Figures (b) and (d) show the density evolution of leg-a and leg-b in the presence of the staggered flux, respectively. Here  $J = 1$ ,  $K = 3$  and flux value is  $\phi = \frac{3\pi}{4}$ . . . . . 80

5.11 Figure shows the density evolution of the two particles with the initial state  $|\Psi_0\rangle = a_{a,0}^\dagger a_{b,0}^\dagger |vac\rangle$  in a ladder system of length  $L = 25$ . Panel (a) and (b) show the density evolution in the presence of the uniform flux and the staggered flux, respectively. Here we consider  $U = 4$ ,  $J = 1$ ,  $K = 3$  and the length of the ladder is  $L = 25$ . . . . . 82

5.12 The figure shows the radius of propagation  $R_n(t)$  in the presence of the uniform and staggered flux in a ladder system of length  $L = 25$ . Here we consider  $J = 1$  and  $K = 3$ . . . . . 83

- 5.13 The figure shows the radial velocity  $V$  of the wavefunction as a function of  $U$  in the presence of (a) the uniform flux and (b) the staggered flux. Here we consider  $J = 1$ ,  $K = 3$  and the length of the ladder is  $L = 25$ . . . . . 83
- 5.14 The figure shows the radial velocity  $V$  of the wavefunction as a function of  $\phi$  in the presence of (a) the uniform flux and (b) the staggered flux for different values of  $U$ . Here we consider  $J = 1$ ,  $K = 3$  and length of the ladder is  $L = 25$ . . . . . 84
- 5.15 The chirality is plotted as a function of time. Figures (a) and (b) correspond to the uniform flux. Figures (c) and (d) correspond to the staggered flux. Here  $J = 1$ ,  $K = 3$ ,  $\phi = \frac{\pi}{4}$  and the length of the ladder is  $L = 25$ . . . . . 85
- 5.16 The shearing,  $Y_{CM}$  is plotted as a function of time for different repulsive and attractive interaction strengths. Here  $J = 1$ ,  $K = 3$ ,  $\phi = \frac{\pi}{4}$  and the length of the ladder is  $L = 25$ . . . . . 86
- 5.17 The figure shows the evolution of  $n_a$  and  $n_b$  defined in Eq. 5.8 for attractive and repulsive interaction strength. The symbols are for staggered flux case and the black dashed line is for uniform flux cases. Here  $J = 1$ ,  $K = 3$ ,  $\phi = \frac{\pi}{4}$  and the length of the ladder is  $L = 25$ . . . . . 87
- 5.18 The figure shows the entire two particles energy spectrum of the ladder as a function of flux. The color scale represents the overlap of the initial state  $|\Psi_0\rangle = a_{a,0}^\dagger a_{b,0}^\dagger |vac\rangle$  with all the energy eigenstates of the system. Figures (a), (b) and (c) correspond to the uniform flux with  $U = 0, 4$  and  $10$ , respectively. Figures (c), (d) and (e) correspond to the staggered flux with  $U = 0, 4$  and  $10$ , respectively. Here we consider  $J = 1$ ,  $K = 3$  and length of the ladder is  $L = 25$ . . . . . 88
- 5.19 Panel (a) figure shows the density evolution of the initial state,  $|\Psi_0\rangle = (a_{a,0}^\dagger)^2 |vac\rangle$  in the presences of the uniform flux. Panel (b) shows the corresponding two-particle correlation at time,  $t = 50(1/J)$ . Here  $J = 1$ ,  $K = 5$ ,  $U = 2$  and length of the ladder is  $L = 25$ . . . . . 89
- 5.20 (a) The figure shows the energy spectrum as a function  $\phi/\pi$ . Here we consider  $J = 1$ ,  $K = 5$ ,  $U = 2$  and length of the ladder is  $L = 25$ . . . . . 90
- 5.21 The figure shows the energy spectrum as a function of  $K$  at a flux strength,  $\phi = \pi$ . Here we consider  $J = 1$ ,  $U = 2$  and length of the ladder is  $L = 25$ . . . . . 90

- 5.22 The figure shows  $P_{avg}$  plotted as a function of  $K$  for the initial state,  $|\Psi_0\rangle = (a_{a,0}^\dagger)^2|vac\rangle$  by taking the average of time between  $t = 90(1/J)$  and  $t = 100(1/J)$ . Here  $J = 1$ ,  $\phi = \pi$  and length of the ladder  $L = 25$ . 91



# List of Tables

2.1	The table shows the memory requirement in exact diagonalization for a system. We assumed the Hamiltonian is stored as a double-precision floating-point numbers square matrix. . . . .	24
2.2	The table shows the basis vectors for $N = 4$ and $L = 4$ with each row representing one basis state of the system. For example, $ 4, 0, 0, 0\rangle$ , $ 3, 1, 0, 0\rangle$ and $ 0, 0, 0, 4\rangle$ are the basis vectors with basis index 1,2 and 35, respectively. . . . .	25
2.3	The table shows the basis vectors and corresponding unique id for $N = 4$ and $L = 4$ . . . . .	26



# Chapter 1

## Introduction

Recent experimental progress in creating and manipulating artificial quantum systems such as atomic, molecular, optical, and condensed matter systems have paved the path for studying the physics of complex many-body systems in and out of equilibrium. The high degree of control of system parameters and high accuracy measurements have led to the successful simulations of several quantum mechanical phenomena and resulted in many seminal observations. Out of many important research frontiers, the study of non-equilibrium dynamics in a closed quantum system has attracted a great deal of attention in recent years. While there are several ways to drive an interacting quantum many-body system out of equilibrium, one of the clean and easy setups is a local or global quench. In this process, an initial state is prepared, which may or may not be the ground state of the Hamiltonian, and then a system parameter of the Hamiltonian is suddenly or slowly changed. These quench dynamics reveal various physical realizations such as the quantum phase transitions, thermalization, integrability, localization, spreading of entanglement and correlation etc. [4–13]. While studying the dynamical evolution of the many-body ground state is a difficult task, recently, a great deal of effort has been made to understand the system's physical properties from the time evolution of a few particle states subjected to a quantum mechanical Hamiltonian. This phenomenon is known as the Quantum Walk [14].

### 1.1 Quantum Walk (QW)

The study of quantum walk (QW), the quantum analog of the classical random walk, has recently attracted a great deal of attention. Based on the fundamental laws of the superposition principle in quantum mechanics, the phenomenon of QW is found to be

important not only in studying the dynamical properties of the quantum mechanical systems but also due to its possible technological applications [15–25]. Numerous studies have been performed in recent years, both theoretically and experimentally, to understand the QW at the single-particle level and also with few interacting particles [26–36].

It is well known that the classical random walk is a stochastic process in which the walker occupies a definite position state and randomness arises due to stochastic transition between the states. It has applications in different fields such as fluid dynamics [37], biology [38], economics [39], and the development of the classical algorithm [40]. On the other hand, in the case of QW, randomness arises due to

1. the quantum superposition of states,
2. non-random, reversible unitary evolution and
3. the collapse of the wave function due to state measurements.

These features generate considerable interest in quantum information algorithms [41–45] and quantum simulations of various systems [46]. In one dimension, the QWs provide superior transport properties as compared to its classical counterpart [47], making them promising candidates for implementing fast and efficient quantum algorithms [41, 48, 49], e.g., search algorithms [42, 43, 50–54]. The coherence properties of the QWs are found to be crucial in simulating energy transport in the photosynthetic process [55, 56]. The dynamical features of the QW also provide an essential framework for modelling perfect quantum state transfer [57–59], studying localization properties [60–62], characterizing topological phases [63–65] and many-body quantum phases [66–68].

Based on the construction, there are two types of QWs possible exhibiting similar physical behaviour such as (a) the discrete-time QW (DTQW) and (b) the continuous-time QW (CTQW).

### 1.1.1 Discrete-time QW (DTQW)

Discrete-time QW is the quantum counterpart of the discrete-time random walk (DTRW). In DTRW, the walker walks in the position space depending upon the outcome of the coin. The coin operation decides the walker’s direction and a subsequent shift operation moves the walker in the position space. For example, a classical walker walks in one dimension sitting at the origin,  $x = 0$ , with a coin. Since the

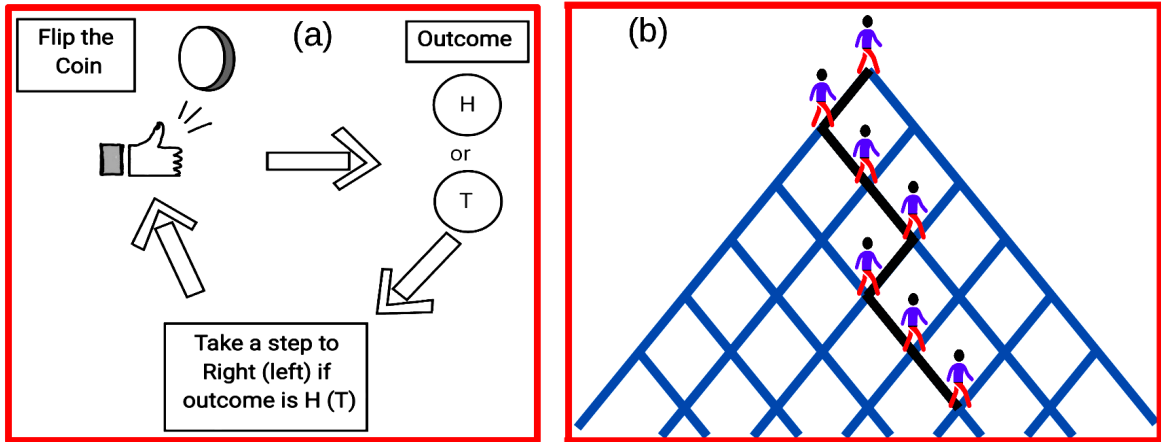


**Figure 1.1:** In classical random walk, (a) the walker continues walking through an iterative process. (b) After many iterative processes, the walker traces out a single path (black line) on a decision tree.

coin has two possible outcomes, e.g., Head (H) and Tail (T), with an equal probability of  $1/2$ , the walker move to the left (L) or to the right (R) with certainty, depending on the outcome. As a result, the walker continues walking through an iterative process as shown in Fig. 1.1(a). After many iterations, the walker traces out a single path of the decision tree graph, as shown in Fig. 1.1(b). However, in the case of the DTQW, the walker evolves with simultaneous operation of the two unitary operators: (a) “quantum coin flip” operator and (b) “shift” operator in the discrete-time domain. The quantum coin flip operation defines the superposition of the direction in which the walker moves simultaneously.

For example, in the case of a one-dimensional DTQW the following steps have to be followed:

1. Define a position space  $H_p$  and a coin space  $H_c$  so that the total space becomes  $H = H_c \otimes H_p$ .
2. The position space of the walker is spanned by the complete orthonormal basis  $\{|x\rangle : x \in \mathbb{Z}\}$ . The coin space is represented by the coin states which has two orthogonal basis states  $\{|L\rangle = \begin{bmatrix} 0 \\ 1 \end{bmatrix}$  and  $|R\rangle = \begin{bmatrix} 1 \\ 0 \end{bmatrix}\}$ .
3. Prepare the system in some initial state,  $|\psi_0\rangle = |\phi_0\rangle \otimes |x\rangle$ , where  $|\phi_0\rangle$  is the initial coin state i.e.,  $|L\rangle$ ,  $|R\rangle$  or superposition of  $|L\rangle$  and  $|R\rangle$  states and  $|x\rangle$  is the initial position state.
4. Introduce the unitary coin operator such as the well known Hadamard operator

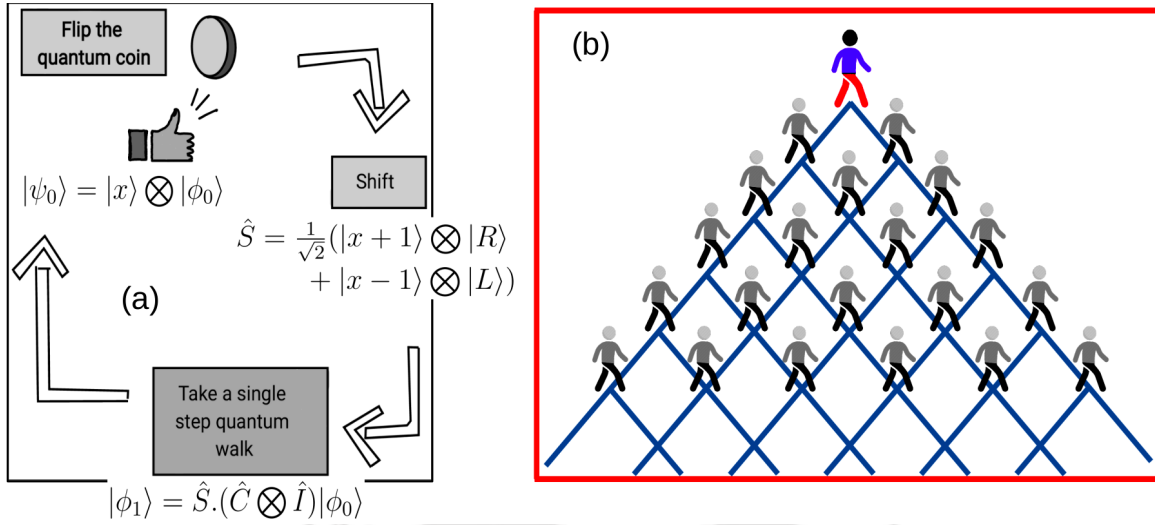


**Figure 1.2:** In quantum walk, (a) the walker continues walking through an iterative process. (b) In quantum walk, the walker moves simultaneously to the left and to the right with complex amplitude without measuring the outcome of the coin in each step. After many iterations, there is a finite probability of the walker to be present everywhere.

$$\text{given by } \hat{C} = \frac{1}{\sqrt{2}} \begin{bmatrix} 1 & 1 \\ 1 & -1 \end{bmatrix}.$$

5. Besides the coin operator there is a shift operator that takes a step forward based on the result of the quantum coin toss. The shift operator is given by

$$\hat{S} = (|R\rangle\langle R| \otimes \sum_x |x+1\rangle\langle x| + |L\rangle\langle L| \otimes \sum_x |x-1\rangle\langle x|) \quad (1.1)$$

In the process, the final state of a single step QW can be written as,

$$|\psi_1\rangle = \hat{S} \cdot (\hat{C} \otimes \hat{I}) |\psi_0\rangle \quad (1.2)$$

which after n-steps takes the form

$$|\psi_n\rangle = \{\hat{S} \cdot (\hat{C} \otimes \hat{I})\}^n |\psi_0\rangle. \quad (1.3)$$

Similar results can be obtained by using different unitary coin operators  $\hat{C}$  and changing the initial state  $|\psi_0\rangle$ .

In summary, starting from an initial state, one can reach a final state after a finite number of time steps using Eq. 1.3.

### 1.1.2 Continuous-time QW (CTQW)

The continuous-time quantum walk (CTQW), which is the quantum counterpart of the continuous-time random walk (CTRW) [22], takes place entirely in the position space and formulates in terms of a decision tree. Each decision tree has an associated transition matrix ( $T$ ), which decides the transition probability of the walker from one node to another. Consider a decision tree graph  $\mathcal{G}$  having  $N$  nodes indexed by integers  $i = 1, 2, \dots, N$  with corresponding  $N \times N$  transition matrix  $T$  with elements

$$T_{ij} = \begin{cases} P_{ij}, & \text{for } i \neq j \text{ if node } i \text{ is connected to node } j. \\ 0, & \text{otherwise,} \end{cases} \quad (1.4)$$

where  $P_{ij}$  is the probability of going from node  $i$  to node  $j$  satisfying the condition  $\sum_{i=1}^N P_{ij} = 1$  and  $P_{ij} \geq 0$  for all  $j$ .

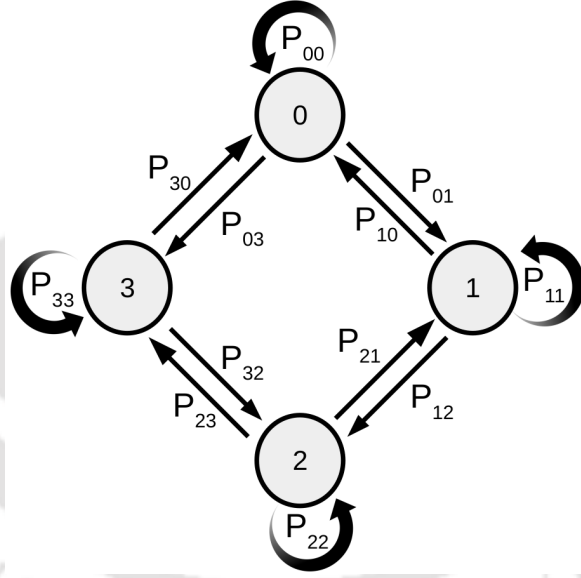


**Figure 1.3:** The figure shows the decision tree with 4 nodes indexed as  $i = 0, 1, 2$  and  $3$ . The transition probabilities in different nodes are shown here.

For example in Fig. 1.3, a decision tree graph with 4 nodes indexed as  $i = 0, 1, 2$  and  $3$  and non-zero transition probabilities in different nodes are shown. The corresponding transition matrix  $T$  can be written as

$$T = \begin{bmatrix} P_{00} & P_{01} & 0 & P_{03} \\ P_{10} & P_{11} & P_{12} & 0 \\ 0 & P_{21} & P_{22} & P_{23} \\ P_{30} & 0 & P_{32} & P_{33} \end{bmatrix}$$

Now each step of the classical walker through the graph  $\mathcal{G}$  is given by

$$\mathbf{V}(n+1) = T\mathbf{V}(n), \quad (1.5)$$

where  $\mathbf{V}(n)$  is the state vector or the probability distribution vector for the nodes at step  $n$ , along with constraints  $\sum_{i=1}^N \mathbf{V}_i(n) = 1$  and  $\mathbf{V}_i(n) \geq 0$ . This is known as a discrete-time Markov process, where the system's state at  $(n+1)$  step is only dependent on the previous step at  $n$  and is independent of any past states. To make the process continuous in time, the transition must occur at all times, and the transition rate to its neighbouring nodes is given by  $P$ , which is uniform and independent of time. The transition rate matrix in which all transition occurs at the uniform rate  $P$  is given by

$$T = -PL, \quad (1.6)$$

where  $L = A - D$  is the Laplacian matrix of the decision tree graph,  $A$  is the graph's adjacency matrix with non-diagonal elements, and  $D$  is a diagonal matrix whose elements  $D_i$  represent the degree of vertex or nodes  $i$ . Here  $L$  is a discrete approximation of the Laplacian operator  $\nabla^2$  in the continuum. Now the continuous-time random walk over  $\mathcal{G}$  is a stochastic Markovian process that evolves as per the master equation,

$$\frac{d\mathbf{V}(t)}{dt} = -T\mathbf{V}(t) \quad (1.7)$$

with solution  $\mathbf{V}(t) = e^{-Tt}\mathbf{V}(t=0)$ .

Based on the ideas of CTRW, *Farhi and Gutmann* in 1998, for the first time formulated the CTQW in terms of the decision trees where the classically constructed transition rate matrix  $T$  to evolve the continuous-time state transitions quantum mechanically [22]. This would involve replacing the real-valued probability distribution vector  $\mathbf{V}(n)$  with a complex-valued wave vector  $\Psi(t)$ . So unlike the CTRW, which propagates as per the master equations, the CTQW instead has its time evolution governed by the Schödinger equation,

$$i\hbar \frac{d}{dt} |\Psi(t)\rangle = H |\Psi(t)\rangle, \quad (1.8)$$

where  $H$  is the transition matrix or the Hamiltonian of the system, which encodes the discrete structure of the underlying graph  $\mathcal{G}$  and the probability distribution vector  $\mathbf{V}(t) = |\Psi(t)|^2$ . Here,  $|\Psi(t)\rangle$  is a complex-valued vector with elements  $\Psi(i, t)$  representing the quantum walker's amplitude on node  $i$  of the graph at time  $t$ . The

general solution of Eq. 1.8 is

$$|\Psi(t)\rangle = e^{-i\hat{H}t}|\Psi(0)\rangle = \hat{U}(t)|\Psi(0)\rangle. \quad (1.9)$$

Here we consider  $\hbar = 1$  and  $m = 1$ . The operator  $\hat{U}(t) = e^{-i\hat{H}t}$  is called as the quantum mechanical time evolution operator and the transition probability between two adjacent nodes  $i$  and  $j$  is given by

$$P_{ij}(t) = |\langle\Psi(j,t)|e^{-i\hat{H}t}|\Psi(i,0)\rangle|^2. \quad (1.10)$$

Like the DTQW, in the CTQW, the walker can simultaneously exist at all possible states or nodes of the decision tree as long as its position state remains unmeasured, as shown in Fig. 1.1. The interference of these complex amplitudes as the walker evolves is responsible for the non-classical propagation characteristics of the QW. Note that this formulation of the CTQW is not limited to the decision trees and can be applied to any general uni-directed graph or system. The CTQW has properties of quantum systems, such as the time reversibility and superposition of the states. Unlike the DTQW, the quantum states do not incorporate any coin states in the CTQW. Hence, in this case, no coin operator is required for the evolution of the walker.

In the above formulation of the QW, an arbitrary graph with  $N$  nodes can be represented as  $N$  position states with coordinate vectors  $|\vec{r}_i\rangle$ , for  $i = 1, 2, \dots, N$ . These state vectors form an orthonormal basis in the  $N$ -dimensional Hilbert space, i.e.

$$\langle\vec{r}_i|\vec{r}_j\rangle = \delta_{ij} \quad (1.11)$$

and the spacing between two adjacent neighboring nodes or position states is  $d$ . In the CTQW, if the walker has an infinitely narrow width and moves in discrete space or nodes, as shown in Fig. 1.4(a) then the nodes can be made arbitrarily close by making  $d \rightarrow 0$  without affecting the outcome. On the other hand, the Hilbert space becomes an infinite-dimensional continuum when the state space is continuous. As a result of this, the quantum walker's position at any point can have a finite uncertainty  $\Delta x$  associated with it, as depicted in Fig 1.4(b). In this scenario, the necessary condition for the QW to retain its characteristic features is  $d \gg \Delta x$ , suggesting that the QW requires a discrete or orthonormal state space [69]. In other words, when a finite width walker performs a walk on a continuous-time-space using an arbitrary transition rate matrix  $H$ , the resulting propagation displays the

characteristic QW signature if and only if the relationship  $d \gg \Delta x$  satisfies.

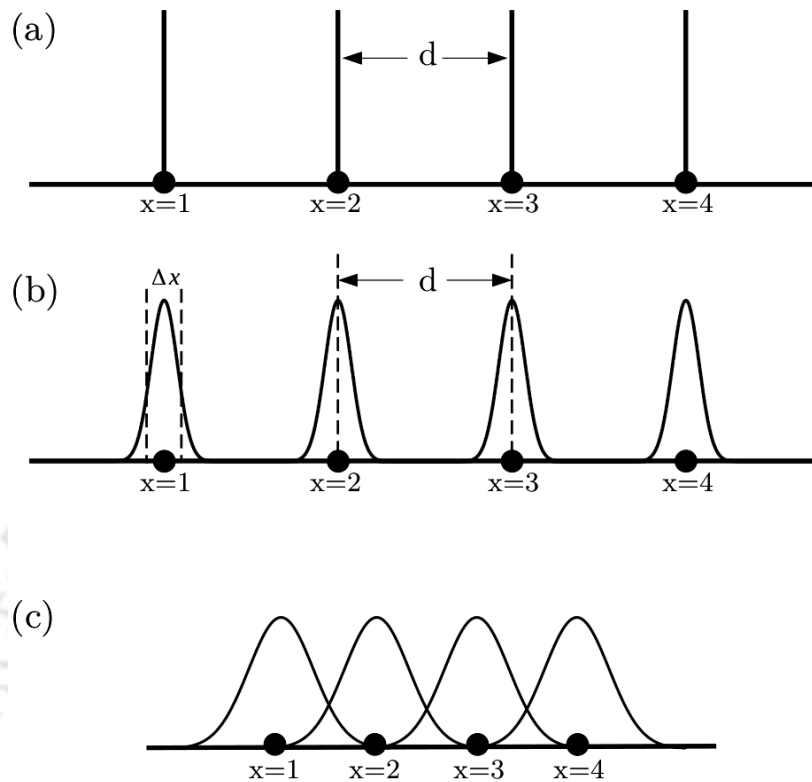


**Figure 1.4:** The figure shows the pictorial representation of the CTQW on a one-dimensional node. (a) The CTQW takes place on discrete nodes. (b) The CTQW takes place on a continuous line, where the width ( $\Delta x$ ) of the walker does not overlap with each other. (c) The CTQW takes place on a continuous space, where the width ( $\Delta x$ ) of the walker overlaps with each other.

When the state is a continuum, i.e.,  $d \rightarrow 0$  and  $\Delta x$  remains finite (see Fig. 1.4(c)), propagation of the walker in a continuous space-time begins to alter. As a result, we would not get the characteristic signature of the QW. In the CTQWs,  $d \gg \Delta x$  is not only for theoretical interest but also an essential condition for the physical implementation in real systems [70, 71].

## 1.2 Distribution of the CTQW and CTRW in one-dimension

In this section, we discuss the distribution of the CTQW on a one-dimensional (1d) lattice. One-dimensional lattice is a straightforward graph in which the nodes are connected in a very regular manner, and each node has exactly two neighbours as shown in Fig. 1.5. As discussed before, for every graph, there exists a Laplacian

matrix,  $L = A - D$ , where  $A$  is the transition or adjacency matrix that contains a finite number of non-zero elements  $a_{ij}$  if node  $i$  is connected to the node  $j$  by a bond and  $D$  is the diagonal matrix representing the degree of the nodes. In the CTQW, the Hamiltonian of the system is equivalent of the Laplacian matrix,  $\mathbf{H} = -\mathbf{L}$  and the quantum mechanical transition probability  $T_{ij}$  between two neighbouring nodes  $i$  and  $j$  as already discussed in previous section.

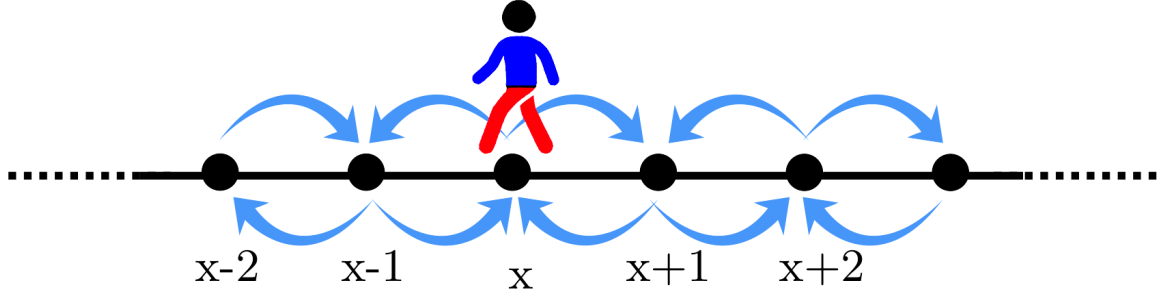


**Figure 1.5:** The figure shows a quantum walker walking on a 1d lattice.

Now consider a 1d lattice of length  $L$  on which a particle performs a CTQW with transition rate matrix elements  $\gamma_{ij} = \gamma$  and each node has  $q$  degrees of freedom. If the whole accessible Hilbert space spanned by the basis vector  $|x\rangle$  is associated with the node  $x$ , then the state of the particle at time  $t$  is given by

$$|\Psi(t)\rangle = \sum_{x=1}^L \psi(x, t)|x\rangle, \quad (1.12)$$

and the Hamiltonian acting on state  $|x\rangle$  is given by

$$H|x\rangle = q|x\rangle - \gamma|x-1\rangle - \gamma|x+1\rangle. \quad (1.13)$$

The Eq. 1.13 is the discrete version of the Hamiltonian for a free particle moving on a lattice. For simplicity, we consider  $\gamma = 1$  and since each node has two neighbours, it means  $q = 2$ . Here we consider the periodic boundary condition and  $H$  is a  $L \times L$  matrix defined as

$$H = \begin{bmatrix} 2 & -1 & \dots & -1 \\ -1 & 2 & -1 & \vdots \\ \vdots & -1 & 2 & -1 \\ -1 & \dots & -1 & 2 \end{bmatrix}.$$

When a particle moves in a periodic lattice potential, it experiences a quantized energy spectrum. The discrete energy bands are the Bloch bands, and the corre-

sponding eigenstates are called the Bloch states. In our case, the Bloch states can be written as a linear combination of states  $|x\rangle$  localized at site  $x$  and are given by

$$|\Phi_k\rangle = \frac{1}{\sqrt{L}} \sum_{x=1}^L e^{ikx} |x\rangle, \quad (1.14)$$

where  $k = 1, 2, \dots, L$ . Since the basis vectors satisfy the relation  $\langle x'|x\rangle = \delta_{x',x}$ , the Eq. 1.14 also satisfy  $\langle \phi_{k'}|\phi_k\rangle = \delta_{k',k}$ . Now putting this  $|\Phi_k\rangle$  on the time independent Schrödinger equation,

$$H|\Phi_k\rangle = E_k|\Phi_k\rangle \quad (1.15)$$

one obtains the energies

$$E_k = 2 \cos k - 2. \quad (1.16)$$

The inverse Fourier transformation of the the Eq. 1.14 is given by

$$|x\rangle = \frac{1}{\sqrt{L}} \sum_{k=1}^L e^{-ikx} |\Phi_k\rangle. \quad (1.17)$$

The transition amplitude between two nearest-neighbour nodes  $x$  and  $y$  is then given by

$$\begin{aligned} \gamma_{xy}(t) &= \frac{1}{L} \sum_{k',k} \langle \Phi_{k'} | e^{ikx} e^{-iHt} e^{-ik'y} | \Phi_k \rangle \\ &= \frac{1}{L} \sum_k e^{-iE_k t} e^{ik(x-y)}. \end{aligned} \quad (1.18)$$

Periodic boundary condition suggests  $\Phi_k(L+1) = \Phi_k(1)$  and  $k = \frac{2n\pi}{L}$ , where  $n = 1, 2, \dots, L$ . Substituting the values of  $E_k$  from Eq. 1.16 and  $k = \frac{2n\pi}{L}$  in Eq. 1.18 gives

$$\begin{aligned} \gamma_{xy}(t) &= \frac{1}{L} \sum_n e^{-i(2 \cos \frac{2n\pi}{L} - 2)t} e^{i\frac{2n\pi}{L}(x-y)} \\ &= \frac{e^{i2t}}{L} \sum_n e^{-i2(\cos \frac{2n\pi}{L})t} e^{i(\frac{2n\pi}{L})(x-y)} \end{aligned} \quad (1.19)$$

In the limit of  $L \rightarrow \infty$ , Eq. 1.19 can be written as

$$\begin{aligned} \lim_{L \rightarrow \infty} \gamma_{xy}(t) &= \frac{e^{i2t}}{2\pi} \int_{-\pi}^{\pi} e^{-i2t \cos k} e^{ik(x-y)} dk \\ &= e^{i2t} (-i)^{x-y} J_{x-y}(2t) \\ &= e^{ip} (-i)^\nu J_\nu(p) \quad [\text{here } \nu = x - y \text{ and } p = 2t.], \end{aligned} \quad (1.20)$$

where  $J_{x-y}(2t)$  is the Bessel's function of the first kind of order  $(x - y)$ . So, when a quantum walker evolves from node  $x$  to node  $y$  at time  $t$ , then corresponding transition probability  $P_{xy}$  is given by

$$P_{xy}(t) = |\gamma_{xy}(t)|^2 = J_{x-y}^2(2t). \quad (1.21)$$

On the other hand, probability theory suggests that the probability distribution of the classical random walker in 1d after a long time  $t$  is given by

$$P(x, t) = \frac{1}{\sqrt{(2\pi t)}} e^{-\frac{(x-x_0)^2}{2t}}, \quad (1.22)$$

where  $x_0$  is the mean position of the walker. The standard deviation of the Gaussian distribution given in Eq. 1.22 is  $\sigma = \sqrt{t}$ , which indicates that the spreading of the walker from the mean position is proportional to  $\sqrt{t}$ . In Fig 1.6, we plot the probability distribution of the quantum and classical random walker in 1d with the position after 50 steps. The probability distribution shows that the quantum walk is no longer a stochastic process like the classical random walk. The quantum walker's speed is also quadratically faster than its classical counterpart.

### 1.3 Multi-particle QW

In this section, we present the generalised framework of the multi-particle QW. In a multi-particle QW,  $p$  distinguishable particles interact locally in a graph  $\mathcal{G}$  with  $N$  nodes. The Hilbert space in this case is spanned by the basis

$$\{|x_1, x_2, \dots, x_p\rangle\}, \quad (1.23)$$

where  $x_i$  is the location of the  $i$ th particle. The Hamiltonian  $\hat{H}$  of the system is given by

$$\hat{H} = \hat{H}_1 \oplus \hat{H}_2 \oplus \dots \oplus \hat{H}_p + \hat{U}, \quad (1.24)$$

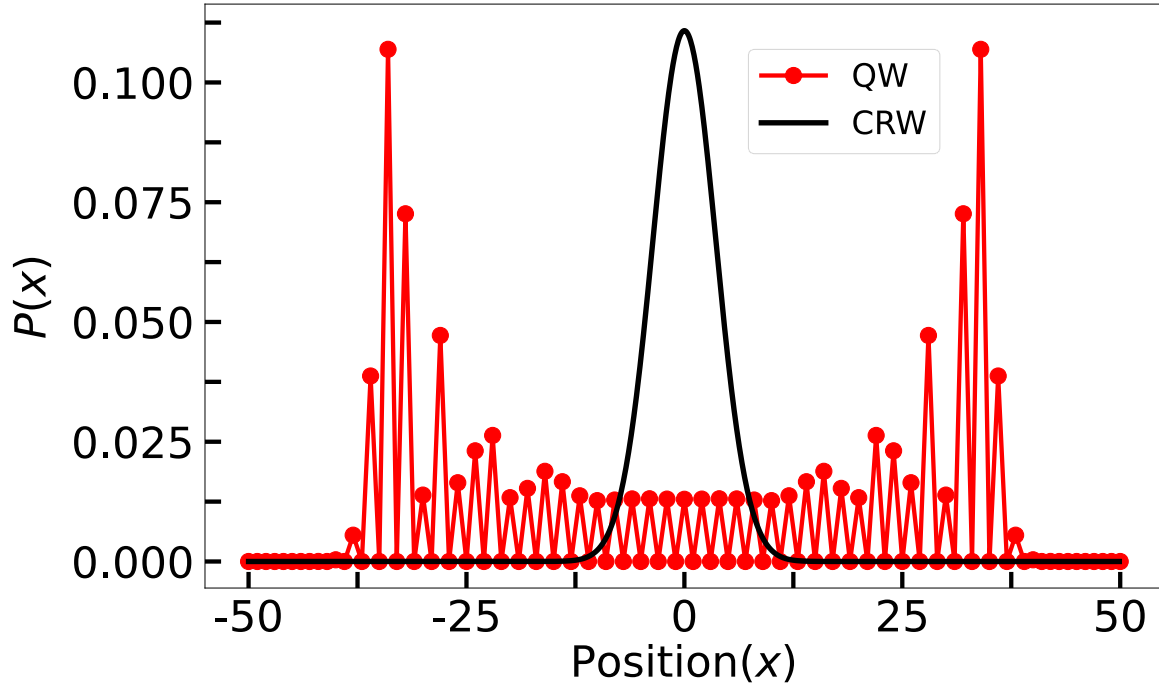


**Figure 1.6:** The figure shows the probability distribution of the classical random walk (black line) and quantum walk (red line) in 1d after 50 steps.

where  $\hat{H}_i$  is the free-particle Hamiltonian matrix of the  $i$ th particle on graph  $\mathcal{G}$ ,  $U$  represents the potential between the particles acting on the entire Hilbert space, and  $\oplus$  is the Kronecker sum defined via the Kronecker product,

$$\hat{H}_1 \oplus \hat{H}_2 = \hat{H}_1 \otimes I + I \otimes \hat{H}_2, \quad (1.25)$$

where  $I$  is the identity matrix of size of the entire Hilbert space. The unitary time-evolution operator is then given by

$$\hat{U}(t) = e^{-i\hat{H}t} = e^{-i(\hat{H}_1 \oplus \hat{H}_2 \oplus \dots \oplus \hat{H}_p)t} = e^{-i\hat{H}_1 t} \otimes \dots \otimes e^{-i\hat{H}_p t}. \quad (1.26)$$

For simplicity, we consider that each particle is walking over the same graph such that the free particle Hamiltonians are identical i.e.,

$$\hat{H}_1 = \hat{H}_2 = \dots = \hat{H}_p \quad (1.27)$$

and the Eq. 1.24 can be written as

$$\hat{H} = \hat{H}^{\oplus p} + \hat{U}. \quad (1.28)$$

Now on applying this time evolution operator  $\hat{U}(t)$  on some state vector  $|\Psi(t_0)\rangle$  one gets

$$|\Psi(t)\rangle = \hat{U}(t - t_0)|\Psi(t_0)\rangle. \quad (1.29)$$

Moreover, proper care has to be taken during the time evolution depending on the statistics followed by the walkers.

## 1.4 Experimental observations

In recent years various different artificial quantum systems known as quantum simulators have facilitated the observation of the QW both at single and two-particle levels [3, 31, 66, 72–77]. One of the most successful quantum simulators in this direction is the system of ultracold atoms in optical lattices. Due to the exquisite control over the system parameters, geometry as well as measurement, these systems have offered a wide range of opportunities to observe fundamental physical problems in various areas such as condensed matter physics, quantum optics, nuclear physics, astrophysics, quantum information and quantum computation.

### 1.4.1 Optical lattice

An optical lattice is a periodic potential formed by superimposing two counter-propagating, coherent, far-detuned laser beams. The neutral atoms can be trapped in the standing wave patterns by exploiting the optical dipole force. Since the laser field induces an oscillating electric dipole moment in an atom, this oscillating dipole interacts with the external laser field and creates a dipole potential  $V_{dip}(\vec{r})$  for the atoms, which is defined as

$$V_{dip}(\vec{r}) = -\vec{d} \cdot \vec{E}(\vec{r}) \propto \alpha(\omega_L) |\vec{E}(\vec{r})|^2, \quad (1.30)$$

where  $\alpha(\omega_L)$  is atomic polarizability,  $\omega_L$  is the frequency of the laser field and  $\vec{E}(\vec{r})$  is the electric field amplitude at position  $\vec{r}$ . Since the intensity of the laser field,  $I \propto |\vec{E}(\vec{r})|^2$ , the strength of this dipole potential is proportional to the intensity of the laser field. Depending upon the laser frequency, atoms in an optical lattice are trapped in either nodes or anti-nodes of the dipole force. By tuning the laser intensity, it is possible to control the interaction and kinetic energy of the atoms in an optical lattice [1]. This flexibility in controlling the system parameter has resulted in the seminal observation of the superfluid to Mott insulator state of bosons in

optical lattices.

### 1.4.2 Tight-binding regime

The periodic potential generated by the optical lattice gives rise to a series of Bloch bands. By making the optical lattice sufficiently deep, one can describe the quantum gases in an optical lattice within a tight-binding approximation. If the interaction energy between the particles is small enough compared to the separation between the lowest and higher energy bands, the particles occupy the lowest Bloch band. Under this circumstance, the particles move around the lattice through tunneling

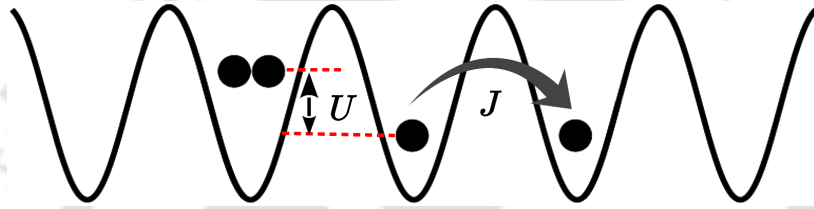


**Figure 1.7:** The figure shows the Bose-Hubbard model. The nearest-neighbour hopping amplitude is  $J$  and on-site interaction is  $U$  when two particles resides at the same site.

and interact locally via scattering. The movement of the atoms is mainly within the nearest neighbour sites with tunneling amplitude  $J$ , and the interaction between the atoms is approximated as onsite only with an interaction strength  $U$ . The onsite interaction strength depends on the s-wave scattering length. The simplest model that describes such a situation is known as the Bose-Hubbard (BH) model (see fig. 1.7) which is represented by the Hamiltonian;

$$H = -J \sum_{\langle i,j \rangle} \hat{a}_i^\dagger \hat{a}_j + h.c + \frac{U}{2} \sum_i \hat{n}_i (\hat{n}_i - 1) - \mu \sum_i \hat{n}_i. \quad (1.31)$$

where  $\hat{a}_i^\dagger$  and  $\hat{a}_i$  are the creation and annihilation operator of the atom at site  $i$ ,  $\hat{n}_i$  is the on-site number operator at site  $i$  and  $\mu$  is the chemical potential. The  $\langle i, j \rangle$  indicates the possible hopping between the nearest neighbour sites.

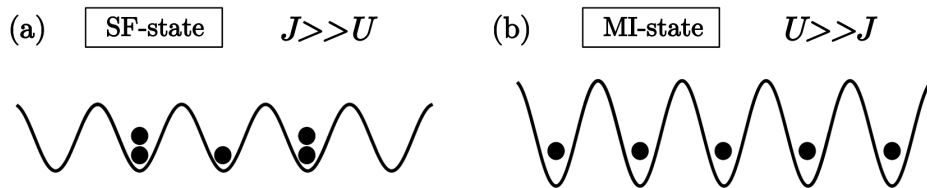


**Figure 1.8:** The figure shows the particle distribution in (a) SF and (b) MI state.

The BH model exhibits a quantum phase transition (QPT) from the superfluid (SF) phase to the Mott insulator (MI) phase of bosons [78]. This QPT was then predicted in the context of ultracold bosonic atoms in optical lattices by *Jaksch et al.* in 1998 [79]. Later the SF-MI transition was observed in a seminal experiment by *Greiner et al.* in 2002 using the Bose-Einstein condensate (BEC) of  $^{87}\text{Rb}$  atoms in a three-dimensional cubic optical lattice [1]. The SF phase appears when the kinetic energy  $J$  dominates over the interaction energy  $U$  ( $J \gg U$ ). In such a scenario, the bosons are delocalized throughout the lattice and there is no restriction on the per site particle number as depicted in Fig. 1.8(a). Since it has a high degree of phase coherence, one can observe a sharp matter-wave interference pattern by looking at the absorption images in the experiment shown in Fig. 1.9(a-c). On the other hand, the MI phase appears when the interaction energy  $U$  dominates over the kinetic energy  $J$  ( $U \gg J$ ). In this case, the bosons are highly localized at individual sites, and a fixed integer number of particles resides per lattice site, as shown in Fig. 1.8(b). The particle fluctuation in the MI phase is significantly less compared to the SF phase, and there is a suppressed phase coherence between the individual matter waves. As a result, no interference pattern appeared in the time-of-flight absorption imaging experiment shown in Fig. 1.9(f-h).

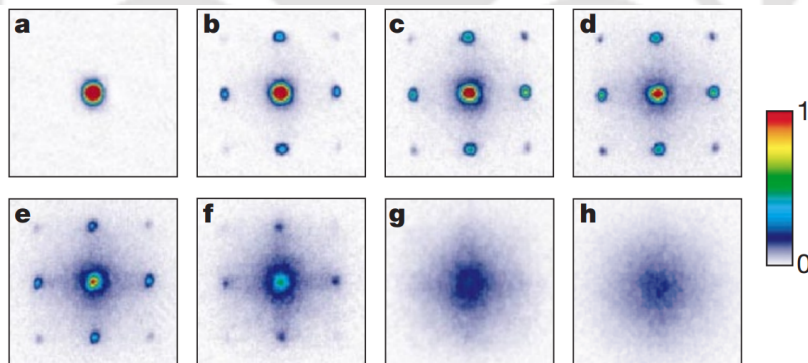


**Figure 1.9:** Absorption images of multiple matter wave interference patterns. These were obtained after suddenly releasing the atoms from an optical lattice potential with different potential depths  $V_0$  after a time of flight of 15 ms. Values of  $V_0$  were: a,  $0E_r$ ; b,  $3E_r$ ; c,  $7E_r$ ; d,  $10E_r$ ; e,  $13E_r$ ; f,  $14E_r$ ; g,  $16E_r$ ; and h,  $20E_r$ . In superfluid regime, atoms are delocalized throughout the lattice with equal phases between the different sites and obtained high-contrast three dimensional interference pattern as expected for a periodic array of phase coherent matter wave sources. In Mott insulator regime, atoms are tightly localized at each sites, as a result there no phase coherence and no interference occurs. This picture has been taken from [1].

Interestingly, the two-body onsite interaction strength  $U$  between the atoms can

be controlled by exploiting the Feshbach resonances [80–83]. This has allowed the successful tuning of the interaction from repulsive to attractive regimes [84]. On the other hand, it has been shown that strong two and three-body onsite interactions can be achieved, which provide scopes to explore interesting physics. Strong two-body interaction leads to the hardcore constraints on bosons ( $a^{\dagger 2} = 0$ ), as a result, they behave like fermions on a lattice site. On the other hand, the three-body constraint ( $a^{\dagger 3} = 0$ ) provides stability against a collapse of the two-body attractively interacting bosons. This has resulted in the prediction of the SF phase of attractively bound boson pairs in optical lattices [85]. In general attractive interaction is responsible for formation of a bound state of composite particles by lowering their energy than the individual components. In contrast in free space, it is impossible to form bound particles by a repulsive interaction because interaction energy between the particles can be freely converted to kinetic energy. However, in a structured environment, such as a periodic potential and in the absence of dissipation, stable bound states can be formed even with repulsive interaction between the atoms. *Winkler et al.* in 2006, reported the first clear observation of such bound state, in the form of repulsively bound pairs (RBP) of ultracold  $^{87}\text{Rb}$  atoms in an optical lattice [2]. The observation of the RBP is a novel property exhibited by the BH Hamiltonian defined in Eq. 1.31. This is an interesting manifestation of competing interaction and kinetic energy of the bosons in a periodic potential. In the limit of strong repulsive interaction  $U \gg J$ , when two particles are placed at the same site, then the two particles can not separate from each other due to non-resonant condition and prefer to remain as onsite pairs. If a state is prepared with two atoms occupying a single site, then it will have a potential energy offset  $\sim U$  with respect to states where the atoms are separated, as shown in Fig. 1.10(a). The width of the Bloch band restricts the kinetic energy of the particles in a lattice. In the case of two atoms on a single site, the maximum kinetic energy is  $8J$  and in this case  $8J \ll U$ . As a result, the two-particle state will not be able to decay by converting the potential energy into kinetic energy. The atoms will remain together and tunnel through the lattice as a bound composite object, as shown in Fig. 1.10(c). In the experiment, a long lifetime of repulsively bound atom pairs has been observed in a three-dimensional optical lattice [2]. Figure 1.10 shows that for repulsive interaction (s-wave scattering length  $a_s = 100a_0$ , where  $a_0$  is the Bohr radius), the atom pair exhibits a remarkably long lifetime (open diamond). On turning off the onsite interaction by tuning the scattering length near zero ( $a_s \sim 0a_0$ ), a much faster decay in the number of doubly occupied sites has been observed, showing the rapid

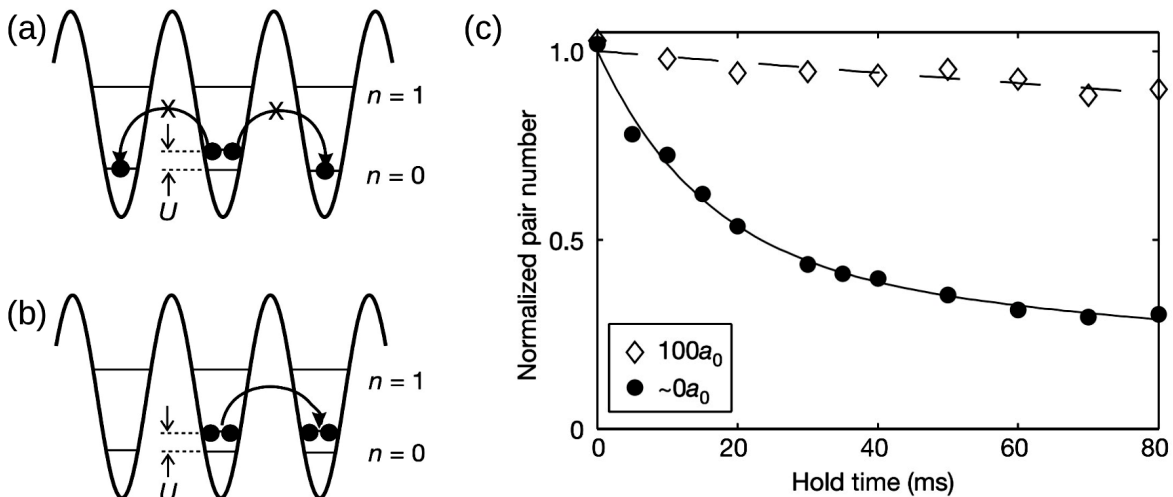


**Figure 1.10:** (a) A state with two atoms located on the same site of an optical lattice has an energy offset  $\sim U$  with respect to states where the atoms are separated. (b) Due to lattice band structure and energy conservation restrict the atom pairs to break up as individual atoms. The atoms will remain together and tunnel through the lattice as a bound composite object. (c) Long lifetime of repulsively bound atom pairs that are held in a 3d optical lattice. For repulsive interaction ( $a_s = 100a_0$ ), the atom pair exhibits the remarkably long lifetime (open diamond). On turning off the on-site interaction by tuning the scattering length near zero ( $a_s \sim 0a_0$ ), it observed a much faster decay in the number of doubly occupied sites showing the the rapid diffusion of unbound atoms through the lattice (filled circles). This picture has been taken from [2]

diffusion of unbound atoms through the lattice (filled circles).

While the full many-body dynamics provide a clear picture of the dynamical properties of the system, QW on the other hand provides a simpler approach to gaining insights into the system at a few particle levels. Considerable efforts have been made to investigate the role of interactions in the case of QWs for more than one indistinguishable particle in various physical contexts [3, 27, 72, 86–95]. The combined effect of the inter-particle interaction and indistinguishability results in interesting features in different systems such as quantum gases in optical lattice [3], correlated photon pairs [72, 73, 96], trapped ions [97], and superconducting qubits [76, 77]. One such revelation is the spatial bunching of bosons in QWs due to the interaction between the two particles initially located at the same site and the Hanbury-Brown and Twiss (HBT) type interference when the two non-interacting bosons are located at two nearest neighbor sites [3, 96]. In contrast, the presence of strong interactions between two nearest neighbour bosons leads to spatial anti-bunching due to fermionization [3, 96]. This experiment reveals a clear signature of RBP in QW of interacting bosons in the framework of the BH model [28].

In Fig. 1.11 (II-III), we plot of the density evolution of the two-particle CTQW

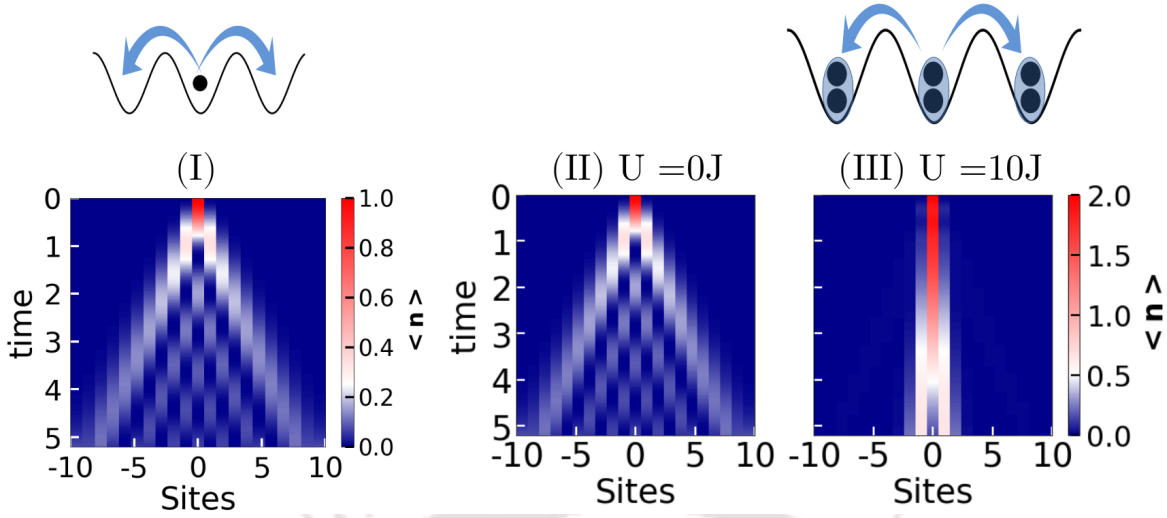


**Figure 1.11:** The figure shows the single-particle and two-particle QW in a one-dimensional lattice of length  $L = 21$ . (I) The density evolution of the single particle. (II) the density evolution of the two non-interacting particles placed at the same site. (III) The density evolution of the two-particle with onsite interaction  $U = 10J$  placed at the same site.

for zero ( $U = 0J$ ) and strong interaction ( $U = 10J$ ), where the particles are considered as bosons. When  $U = 0J$ , the two particles perform independent particle QW in which a particle is initially localized at a chosen site of a lattice tunnel to the neighbouring sites with equal probabilities as depicted in Fig. 1.11(II). In the process, coherent interference of all single-particle paths leads to ballistic expansion with a well-defined wavefront, as shown in Fig. 1.11(I). For  $U = 10J$ , however, the two particles perform QW as a composite object with a very slow spreading of the wavefunction (Fig. 1.11(III)). In the actual experiment, the dynamics of RBP through the CTQW of two ultracold atoms prepared in the same state in the optical lattice were investigated in 2015 by *Preiss et al.* [28]. It was found that when the interaction is weak (i.e.  $U = 0.7J$ ), two atoms perform an independent single-particle quantum walk. This signature was observed using the two-particle correlation, which is the direct product of the single-particle densities as shown in Fig. 1.12(I). The finite elements in the correlation matrix's symmetric position indicate the free particle QW. However, when the interaction is strong enough (i.e.  $U = 5.1J$ ), a repulsively bound pair is formed, and the two particles move as a composite object with reduced hopping strength. This is reflected in the finite diagonal elements of the correlation matrix as shown in Fig. 1.12(II).

Interestingly, when two bosons start the QW from two nearest neighbour sites, then the interplay between interactions and quantum two-particle HBT interference

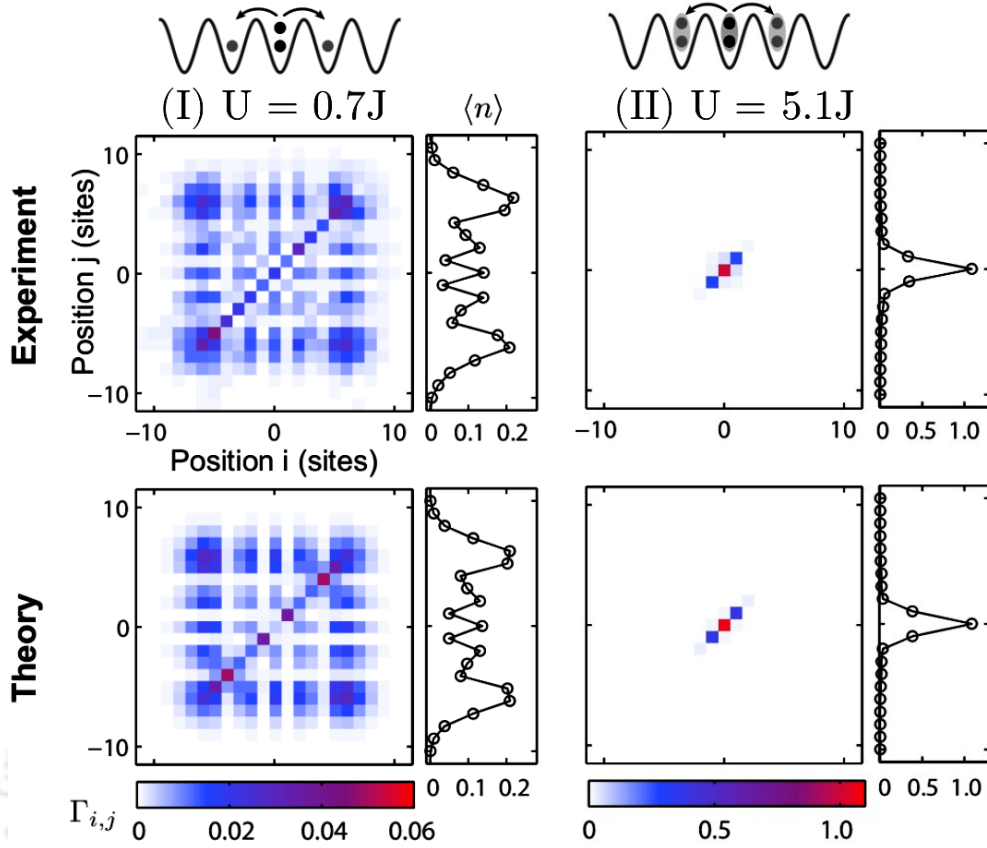


**Figure 1.12:** The Figure shows the two-particle correlations  $\Gamma_{i,j}$  during the evolution of the two-particle QW placed at the same site. The two particles perform as independent single-particle quantum walk for weak interactions ( $U = 0.7J$ ). The corresponding two-particle correlation is the direct product of the single-particle densities. On increasing interaction strength, repulsively bound pairs form and two particles move as a composite object which can be reflected from the finite diagonal elements of the correlation matrix. This picture has been taken from [3].

results in a continuous transition from bosonic spatial bunching to fermion like spatial anti-bunching correlations between the particles, as shown in Fig. 1.13. Where the two-particle correlations is defined as  $\Gamma_{i,j} = \langle a_i^\dagger a_j^\dagger a_i a_j \rangle$ . When  $U = 0.7J$ , the correlation shows the spatial bunching indicating that two bosons tend to stay close to each other (see Fig. 1.13(I)). At strong interactions ( $U = 5.1J$ ), the correlation is transformed from spatial bunching to anti-bunching, indicating that the two atoms repel each other, as shown in Fig. 1.13(II). This anti-bunching correlation is similar to the correlation exhibited by two non-interacting fermions initially placed at the nearest-neighbour sites.

These developments have paved the paths for quantum simulations involving a few particles, and this provides a platform to have a bottom-up approach to understanding the physics of many-body systems. Owing to their remarkable efficacy in

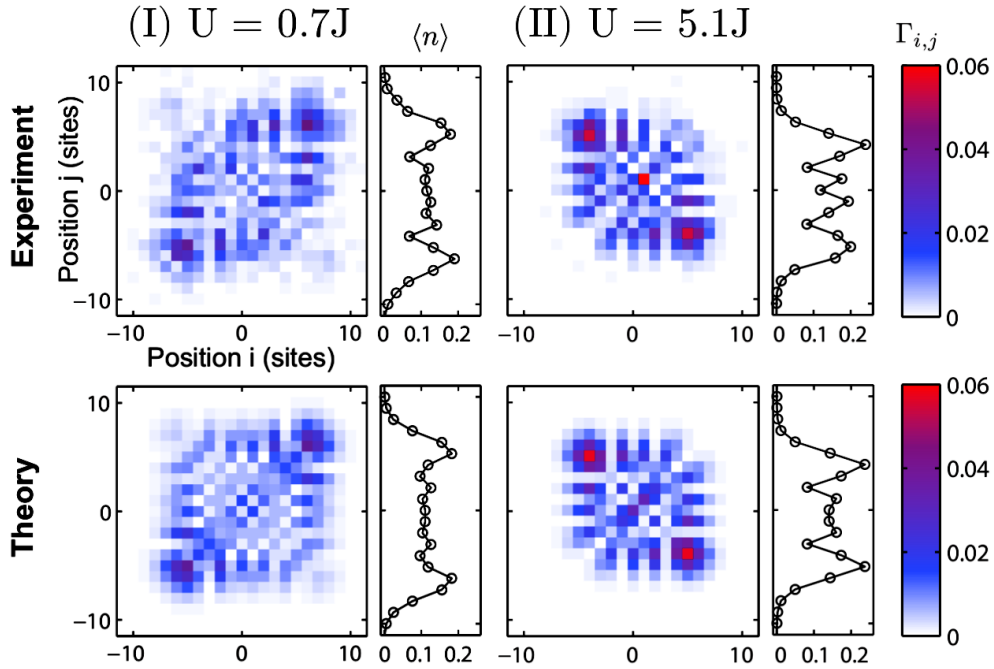


**Figure 1.13:** The figure shows the HBT interference and fermionization when two bosons start the QW from the two nearest-neighbour sites. (I) For weak interaction,  $U = 0.7J$ , the correlation shows the spatial bunching of the bosons indicating that two bosons have tendency to stay close to each other. (II) Strong on-site interaction,  $U = 5.1J$ , fermionize the bosons in one-dimension display the anti-bunching in correlation, indicating that the two atoms repel each other. This picture has been taken from [3].

probing many-body physics, QWs have been widely used to study different physical phenomena using both theoretical and experimental approaches [3, 27, 94, 98–101].

On the other hand, the physics of two-component systems host a completely different scenario compared to single-particle systems. The combined role of inter and intra-component interaction, correlation and statistics play a crucial role in revealing novel physics, which has been explored in great detail in the context of the Hubbard models. However, the experimental realization of such systems was made possible in systems of ultracold atoms in optical lattices. Considerable progress has been made in creating and manipulating binary atomic mixtures in optical lattices. Although the experiments using atomic mixtures are extremely complex compared to the single species systems, recent progress on the experimental front has made it possible to access Bose-Bose, Fermi-Fermi and Bose-Fermi mixtures in the absence and presence of optical lattices [102–108]. The complexities of such binary mixtures yield significant insights into the interacting spin model, atom-molecule interactions, quantum entanglement, topological phase transitions etc [109–120]. Interestingly, the two-component systems with hopping imbalance have shown to reveal exciting

new physics in various context [109, 111, 121–124]. Moreover, the dynamics of these constrained systems under proper conditions may reveal a different scenario in terms of transport properties and relaxation, which has been investigated in a recent experiment [125]. While the many-body simulations of such dynamical systems are challenging, the dynamics in the context of QW in such systems may reveal completely different physics, which have gained attention in recent years [126–129].

Apart from the two-particle QW in the presence of interaction, several other studies have been performed in recent years to study the effect of interaction, topology, and disorder in many different artificial systems. While the experimental observation of such findings is limited, many theoretical studies have been performed in recent years.

In this thesis, we have considered two-component bosonic systems with hopping imbalance (or mass imbalance) in one-dimensional lattices and predicted various interesting physics in the context of the QW. In the following, we provide a brief outline of the different chapters of the thesis.

## 1.5 Chapter-wise outline of the thesis

The organization of the thesis is as follows:

In Chapter 2, we discuss the numerical methods used for simulating CTQW. We briefly discuss the Exact diagonalization and Time-evolving Block Decimation (TEBD) methods based on the framework of matrix product states (MPS) that are primarily used to perform CTQW.

In Chapter 3, we discuss the two-component QW in a one-dimensional lattice with hopping imbalance. We consider a one-dimensional system in which two interacting particles with different hopping strengths perform QW. This situation is equivalent to the QW of two interacting particles with different masses. We show that the combined effect of hopping imbalance and interaction exhibits exciting physics in the context of two-particle QW. We also show that the choice of the initial state plays an essential role in the two-component QW. We have employed the Exact diagonalization methods to perform CTQW numerically.

In Chapter 4, we show that the signatures of non-trivial pairing in the QW of two-component bosons in a one-dimensional lattice. We show that in the case of the QW of two-component bosons in one-dimension, non-trivial local bound pairs

can be formed due to the interplay of inter-and intra-component interactions. By considering different initial states of more than two particles, we show that the quantum two-particle correlation and competing interactions favor the formation of onsite inter-component bound pairs even if the two components start their QW from the nearest-neighbour sites. Depending on the initial conditions, the formation of bound pairs is more robust when suitable hopping asymmetry is introduced between the components. We also obtain a re-entrant feature in the QW as a function of the inter-species interaction. We have employed the TEBD methods to perform CTQW numerically.

In Chapter 5, we introduce the QW of interacting particles in the Harper-Hofstadter ladder. Ladder geometries are essential in condensed matter physics, as it provides a simple extension to the one-dimensional system towards the two-dimensional systems. This chapter discusses the QW of the single and two interacting particles on the two-leg ladder threaded by the magnetic field. In this context, we consider two types of magnetic fields: uniform and staggered magnetic fields. In single-particle QW, we discuss the appearance of chiral motion in the QW depending upon the kind of magnetic field that threads the ladder. In two-particle QW, interaction and magnetic flux significantly affect their spreading dynamics. We discuss the simultaneous effect of interaction and magnetic field on the spreading dynamics, chiral motion, and bound state formation by considering different two-particle initial states. We also discuss the impact of the magnetic field on the formation of repulsively bound pairs when interaction strength is comparable to the hopping strength. We have employed the Exact diagonalization methods to perform CTQW numerically.

Finally, Chapter 6 concludes with a summary of the results and detailed discussions of the main body of the thesis. It also includes the possible extension of the results discussed in the thesis and a list of new problems that can be explored in the future.

## Chapter 2

# Numerical methods

In this chapter, we provide the details of the numerical methods utilised to perform the thesis work. As the problems studied in the thesis involve one-dimensional interacting systems, we utilise the exact diagonalization (ED) method as well as the time-evolving block decimation (TEBD) method. In the following we briefly discuss both the methods.

### 2.1 Exact Diagonalization

Exact Diagonalization is one of the most powerful numerical techniques used to solve the physics of finite-size systems and to extract the exact information about them. It exactly determines the energy eigenstates and energy eigenvalues of a quantum Hamiltonian. In this technique, a quantum Hamiltonian can be written in a matrix form for a discrete and finite system. This method is widely used to study quantum phase transition, computing correlation functions, energy gap, and entanglement entropy in strongly correlated systems such as the Bose-Hubbard model, Heisenberg model,  $t - J$  model, and many more. For a given system with a Hamiltonian  $H$ , this ED method is primarily based on the following steps:

1. Find a complete set of orthonormal basis states  $\{|\phi_i\rangle\}$ .
2. Using the basis states, compute the matrix elements of the Hamiltonian matrix as

$$H_{i,j} = \langle\phi_j|H|\phi_i\rangle. \quad (2.1)$$

3. Diagonalize the Hamiltonian matrix  $\hat{H}$  using some diagonalization subroutine on the computer and get the eigenvalues and eigenvectors.

Now we discuss this method in the context of the Bose-Hubbard (BH) model. As already introduced in Chapter 1, in the second quantized notations, the BH model can be written as,

$$\begin{aligned}\hat{H} &= -J \sum_{\langle i,j \rangle} \hat{a}_i^\dagger \hat{a}_j + h.c + \frac{U}{2} \sum_i \hat{n}_i(\hat{n}_i - 1) \\ &= \hat{h}_J + \hat{h}_U\end{aligned}\quad (2.2)$$

The first term of  $\hat{H}$  corresponds to kinetic energy and is defined as ( $\hat{h}_J$ ), and the second term corresponds to the interaction energy and is defined as ( $\hat{h}_U$ ).

### 2.1.1 Construction of basis

Since our Hamiltonian is in second quantized form, the most natural choice for the basis is the occupation number of Fock space basis. For example, the basis vectors for one-dimensional system of length  $L$  can be written as

$$\{|n_1, n_2, \dots, n_L\rangle\} \equiv |n_1\rangle \otimes |n_2\rangle \otimes \dots \otimes |n_L\rangle, \quad (2.3)$$

where  $n_i$  is the number of particles at  $i^{\text{th}}$  site. If we consider the on-site dimension  $m$ , then the full Hilbert space dimension becomes  $D_f = m^L$ . Since the dimension of the Hilbert space spanned by the basis states grows exponentially with the system size, it is challenging to handle even a small system of typically 10 sites with few particles per site using the standard diagonalization techniques. From table 2.1, one can get an idea about memory requirements. However, by utilizing certain symmetries, it is

On-site dimension (m)	System Size (L)	Number of states	Hamiltonian size in memory
4	4	256	512KB
4	6	4096	128MB
4	10	1048576	8192GB
4	12	2097152	2PB

**Table 2.1:** The table shows the memory requirement in exact diagonalization for a system. We assumed the Hamiltonian is stored as a double-precision floating-point numbers square matrix.

possible to reduce the size of the Hamiltonian matrix for a systems that is accessible with the present computing power. One such symmetry in the case of the BH model is the conservation of the total particle number,  $\hat{N} = \sum_{i=1}^L \hat{n}_i$ . Since  $\hat{N}$  commutes

with  $\hat{H}$  i.e.  $[\hat{H}, \hat{N}] = 0$ , they can have a simultaneous eigen spectrum. With this, the reduced Hilbert space dimension for  $N$  particles in a one-dimensional lattice of length  $L$  is given by

$$D_r = \frac{(N + L - 1)!}{N!(L - 1)!}. \quad (2.4)$$

For example, a one-dimensional system of length  $L = 4$  has  $N = 4$  particles, the full Hilbert space dimension without symmetry is  $4^4 = 256$ . Whereas, on the implication of symmetry of total particle number conservation, the Hilbert space dimension reduces to 35 (by using Eq. 2.4). These basis vectors are shown in table 2.2 in a descending order in which each row represents a basis vector. Therefore, the implementation of the symmetry reduces the Hilbert space dimension substantially, which reduces the effective computational cost and memory needed for the calculations. The basis vectors can be generated using the techniques proposed here [130].

Basis index	$n_1$	$n_2$	$n_3$	$n_4$
1	4	0	0	0
2	3	1	0	0
3	2	1	1	0
4	1	1	1	1
$\vdots$			$\vdots$	
35	0	0	0	4

**Table 2.2:** The table shows the basis vectors for  $N = 4$  and  $L = 4$  with each row representing one basis state of the system. For example,  $|4, 0, 0, 0\rangle$ ,  $|3, 1, 0, 0\rangle$  and  $|0, 0, 0, 4\rangle$  are the basis vectors with basis index 1, 2 and 35, respectively.

### 2.1.2 Construction of Hamiltonian matrix

After constructing all the basis vectors, now we have to find out the matrix elements of the BH Hamiltonian  $\hat{H}$  given in Eq. 2.2 with respect to the generated basis vectors as:

$$H_{ij} = \langle \phi_j | \hat{H} | \phi_i \rangle, \quad (2.5)$$

where  $i$  and  $j$  are the basis indices. To find the elements of the matrix it is easier to treat the total Hamiltonian as a sum of the hopping term  $\hat{h}_J$  and the interaction term  $\hat{h}_U$ . The computation of  $\hat{h}_U$  is trivial as it involves only the diagonal terms. On the other hand,  $\hat{h}_J$  has a contribution to the off-diagonal elements of the Hamiltonian. In the following we discuss the calculation of the matrix elements of  $\hat{h}_J$ .

First, we label each basis vector with an unique id to contract the information

into a single operation such as

$$X_i = \sum_{j=1}^L \sqrt{k_j} n_j, \quad (2.6)$$

where  $k_j$ 's are the prime numbers  $\{2, 3, 5, 7, \dots\}$  and  $n_j$  is the particle number at site  $j$ . For example, if we take the basis  $|2, 1, 1, 0\rangle$ , then the corresponding unique id is

$$\begin{aligned} & 2 \times \sqrt{2} + 1 \times \sqrt{3} + 1 \times \sqrt{5} + 0 \times \sqrt{7} \\ &= 2.82842712475 + 1.73205080757 + 2.2360679775 + 0 \\ &= 6.79654590982. \end{aligned}$$

Now we can re-write the table 2.2 with the unique id which is shown in table 2.3.

Basis index	$n_1$	$n_2$	$n_3$	$n_4$	Unique id
1	4	0	0	0	5.65685424949
2	3	1	0	0	5.97469149469
3	2	1	1	0	6.79654590982
4	1	1	1	1	8.02808365851
$\vdots$		$\vdots$			$\vdots$
35	0	0	0	4	10.5830052442

**Table 2.3:** The table shows the basis vectors and corresponding unique id for  $N = 4$  and  $L = 4$ .

This approach makes the calculation easier as it is not necessary to compare the basis of the bra and the ket states element-wise while calculating the matrix elements. Rather, one requires to compare the unique id labels only. For any specific basis vector  $|v\rangle$  with basis index  $p$ , if we operate the hopping term  $a_i^\dagger a_j$  on it then we get

$$a_i^\dagger a_j |v\rangle = \sqrt{(n_i + 1)n_j} |..n_i + 1, \dots, n_j - 1.. \rangle = \sqrt{(n_i + 1)n_j} |w\rangle.$$

One can then compute the label of the state vector  $|w\rangle$  using Eq. 2.6 and check if it exists in the table of unique ids or not. If it is there then the corresponding basis index (say  $q$ ) can be identified. After this the  $H(p, q)$  element of the Hamiltonian with  $-J\sqrt{(n_i + 1)n_j}$  can be stored. This process continues until the final basis vector is reached. With the help of the above technique one can completely construct the Hamiltonian for the BH model which can be diagonalised to obtain the eigenvalues and eigenvectors using some standard routines. Then for the CTQW

the time evolved state can be computed by

$$\Psi(t) = \hat{\mathcal{U}}(t)\Psi(0) \quad (2.7)$$

with the time evolution operator

$$\hat{\mathcal{U}}(t) = e^{-i\hat{H}t}. \quad (2.8)$$

and the initial state  $|\Psi(0)\rangle$  at time  $t = 0$ .

## 2.2 Time-evolving block-decimation (TEBD)

The time-evolution of the quantum many body state is a very difficult task. In 2004, *G. Vidal* first developed an algorithm to simulate the time evolution of the many-body states [131]. This algorithm is called the time-evolving block decimation (TEBD) since it dynamically adapts the relevant low-dimensional Hilbert subspace of an exponentially larger original Hilbert space for better accuracy. This algorithm is based on the Matrix Product States (MPS) and widely used for simulating the time evolution of the one-dimensional quantum many-body systems governed by a Hamiltonian with at most nearest-neighbour interactions. Before proceeding with the details of the TEBD method we briefly discuss the MPS formalism.

### 2.2.1 Matrix Product State (MPS)

The matrix product state (MPS) is a tensor network representation of the quantum many-body state. It is mainly used in theoretical physics to study strongly correlated systems. Here we discuss the simple implementation of the MPS state from a quantum many-body state. Consider a one-dimensional system consisting of  $L$  sites with open boundary condition and corresponding wavefunction

$$|\Psi\rangle = \sum_{n_1, n_2, \dots, n_L} A_{n_1, n_2, \dots, n_L} |n_1, n_2, \dots, n_L\rangle, \quad (2.9)$$

where  $|n_i\rangle$  is the local state space of the system at site  $i$ . For example, in spin system  $|n_i\rangle = \{\uparrow, \downarrow\}$ , in bosonic systems  $|n_i\rangle = \{0, 1, 2, \dots\}$ .  $A_{n_1, n_2, \dots, n_L}$  is number of coefficients in the system which is equal to the dimension of the Hilbert space of the system. For transformation of this coefficient vector to matrix product form we need to apply the method of Singular Value Decomposition (SVD), which is a well

known method in linear algebra [132]. So the coefficient vector can be written in matrix form as

$$A_{n_1, n_2, \dots, n_L} = A_{n_1, (n_2, \dots, n_L)}. \quad (2.10)$$

Now by performing an SVD on this matrix we get

$$A_{n_1, n_2, \dots, n_L} = A_{n_1, (n_2, \dots, n_L)} = \sum_i U_{n_1, i_1} S_{i_1, i_1} (V^\dagger)_{i_1, (n_2, \dots, n_L)}. \quad (2.11)$$

Here  $U$  and  $V$  are the unitary matrices and  $S$  is a diagonal matrix. Now the index  $i_1$  of  $S_{i_1, i_1}$  and  $(V^\dagger)_{i_1, (n_2, \dots, n_L)}$  can be contracted and transformed into  $A_{i_1, (n_2, \dots, n_L)}$ . Next by renaming  $U_{n_1, i_1}$  as  $A_{i_1}^{n_1}$ , we can rewrite Eq. 2.10 as

$$A_{n_1, (n_2, \dots, n_L)} = \sum_{i_1} A_{i_1}^{n_1} A_{i_1, (n_2, \dots, n_L)}. \quad (2.12)$$

Then transform  $A_{i_1, (n_2, \dots, n_L)}$  to  $A_{(i_1, n_2)(n_3, \dots, n_L)}$  and apply SVD on it. With this

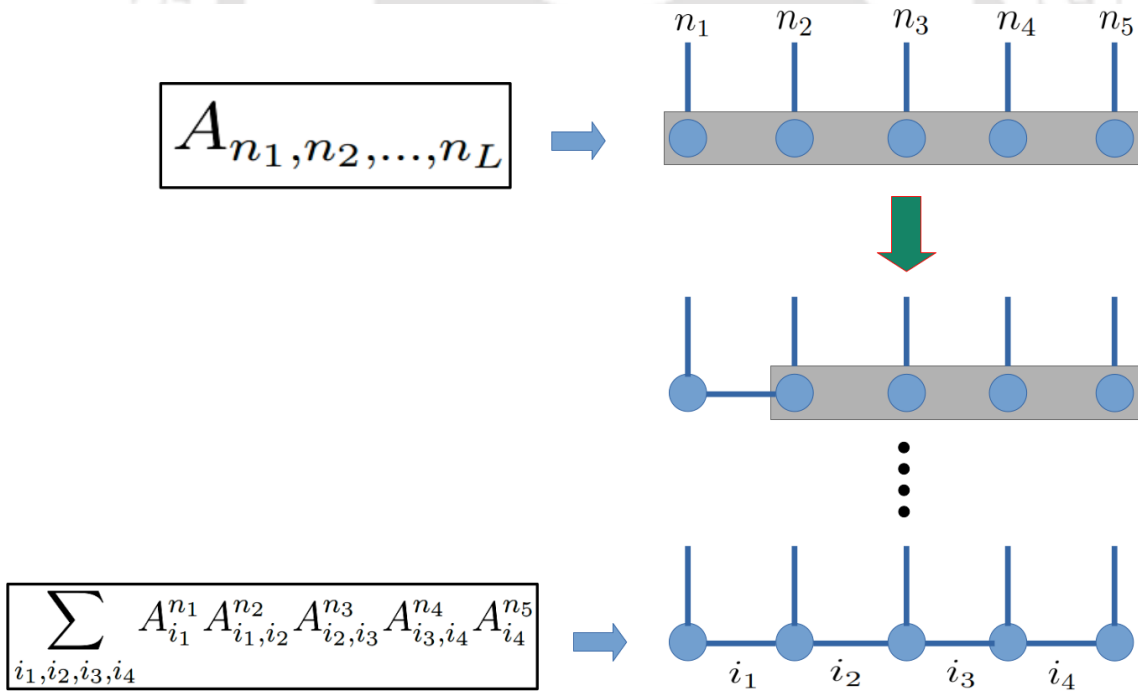


**Figure 2.1:** The graphical representation of the left canonical MPS formation using SVD process for a system of length  $L = 5$ .

Eq. 2.12 becomes

$$A_{n_1, (n_2, \dots, n_L)} = \sum_{i_1} \sum_{i_2} A_{i_1}^{n_1} U_{(i_1, n_2), i_2} S_{i_2, i_2} (V^\dagger)_{i_2, (n_3, \dots, n_L)}. \quad (2.13)$$

Again, by renaming the  $U_{(i_1, n_2), i_2}$  as  $A_{i_1, i_2}^{n_2}$  and contracting the index  $i_2$  of  $S_{i_2, i_2}$  and  $(V^\dagger)_{i_2, (n_3, \dots, n_L)}$ . As a result, the Eq. 2.12 becomes

$$A_{n_1, n_2, \dots, n_L} = \sum_{i_1} \sum_{i_2} A_{i_1}^{n_1} A_{i_1, i_2}^{n_2} A_{i_2, (n_2, \dots, n_L)} \quad (2.14)$$

This process is repeated until we reach the end of the lattice. Finally, the wavefunction transforms into an MPS which is given as

$$|\Psi\rangle = \sum_{i_1, i_2, \dots, i_{L-1}} A_{i_1}^{n_1} A_{i_1, i_2}^{n_2} \dots A_{i_{L-2}, i_{L-1}}^{n_{L-1}} A_{i_{L-1}}^{n_L} |n_1, n_2, \dots, n_L\rangle. \quad (2.15)$$

In the above equation,  $i$ 's are known as the bond indices and  $n_i$  indicates the physical index. In Fig. 2.1, we graphically represent the formation of MPS from a general state. The above formalism is called as Left-canonical MPS. In Fig. 2.2

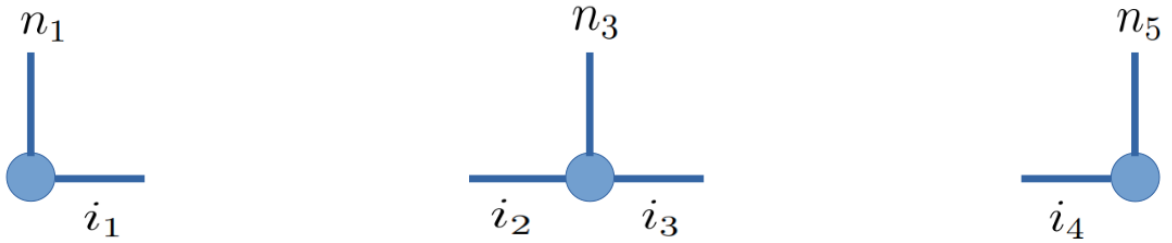


**Figure 2.2:** The figure shows the graphical representation of “A” matrices at the ends and in the bulk of the chain for a system of length  $L = 5$ . The left diagram represents  $A_{i_1}^{n_1}$ , the row vector at the left of the MPS end, the right diagram represents  $A_{i_4}^{n_5}$ , the column vector at the right end of the MPS. The center diagram represents  $A_{i_2, i_3}^{n_3}$ .

we have shown the graphical rules for the “A” matrices where a site is represented by a solid circle, the physical index  $n_i$  by a vertical line and the matrix indices by horizontal lines. The first and the last sites of an MPS are row and column vectors, respectively. Similarly, there are two more ways an MPS can be created. One is the Right-canonical MPS, which is developed by contracting from right to left instead of left to right and  $|\Psi\rangle$  can be written as

$$|\Psi\rangle = \sum_{i_1, i_2, \dots, i_{L-1}} B_{i_1}^{n_1} B_{i_1, i_2}^{n_2} \dots B_{i_{L-2}, i_{L-1}}^{n_{L-1}} B_{i_{L-1}}^{n_L} |n_1, n_2, \dots, n_L\rangle. \quad (2.16)$$

The last one is the mixed-canonical MPS, in which  $|\Psi\rangle$  looks like

$$|\Psi\rangle = \sum_{i_1, i_2, \dots, i_{L-1}} A_{i_1}^{n_1} \dots A_{i_{l-1}, i_l}^{n_l} S_{i_l, i_l} B_{i_l, i_{l+1}}^{n_{l+1}} \dots B_{i_{L-1}}^{n_L} |n_1, n_2, \dots, n_L\rangle. \quad (2.17)$$

## 2.2.2 Implementation of the TEBD method

The essential technique of TEBD is to write the time-evolution operator  $\hat{U}(\delta t) = e^{-i\hat{H}\delta t}$  (consider  $\hbar = 1$ ), introduced in Eq. 2.8, for a small time  $\delta t$  using the *Suzuki-Trotter* decomposition [133, 134]. If the Hamiltonian of interest contains only the nearest-neighbour interactions, then the Hamiltonian can be written in terms of local two site terms as;

$$\hat{H} = \sum_i \hat{h}_{i,i+1}. \quad (2.18)$$

The exact time evolution is given by

$$\hat{U}_{exact}(\delta t) = e^{-i\hat{H}\delta t}. \quad (2.19)$$

Now  $\hat{H}$  can be rewritten as;

$$\begin{aligned} \hat{H} &= \hat{H}_{even} + \hat{H}_{odd} \\ &= \sum_{i \in even} \hat{h}_{i,i+1} + \sum_{i \in odd} \hat{h}_{i,i+1}. \end{aligned} \quad (2.20)$$

In this scenario, all  $\hat{h}_{i,i+1}$  terms commute among themselves but,  $\hat{H}_{even}$  and  $\hat{H}_{odd}$  do not commute. Using the Baker-Campbell-Hausdorff formula  $\hat{U}_{exact}(\delta t)$  can be approximated as

$$\begin{aligned} \hat{U}_{exact}(\delta t) &= e^{-i\hat{H}\delta t} \\ &= e^{-i\hat{H}_{even}\delta t} e^{-i\hat{H}_{odd}\delta t} e^{-i[\hat{H}_{even}, \hat{H}_{odd}]\delta t^2} \\ &\approx e^{-i\hat{H}_{even}\delta t} e^{-i\hat{H}_{odd}\delta t} + \mathcal{O}(\delta t^2) \\ &= \hat{U}_{TEBD} + \mathcal{O}(\delta t^2). \end{aligned} \quad (2.21)$$

The non-commutative nature of  $\hat{H}_{even}$  and  $\hat{H}_{odd}$  gives rise to a second order error of order  $\mathcal{O}(\delta t^2)$  in each step of the time evolution due to the approximation

$$e^{-i[\hat{H}_{even}, \hat{H}_{odd}]\delta t^2} \approx \hat{1} - i\delta t^2[\hat{H}_{even}, \hat{H}_{odd}]. \quad (2.22)$$

If we consider a longer time of evolution  $T$ , then it can be divided into  $\frac{T}{\delta t}$  intervals. So, in time  $T$  the error is  $\frac{T}{\delta t} \times \mathcal{O}(\delta t^2) = \mathcal{O}(\delta t)$ , which is the first order in  $\delta t$ . With this the time evolved wavefunction becomes

$$|\psi(t + \delta t)\rangle = e^{-i\hat{H}_{even}\delta t} e^{-i\hat{H}_{odd}\delta t} |\psi(t)\rangle \quad (2.23)$$

Now the two-site time-evolution operator is applied on the MPS description of the wavefunction as shown in the graphical representation in Fig. 2.3. After operating a two-site operator, the local dimension increases by  $n^2$  in each time step and the MPS description vanishes on those two-sites. As a result, at every time step, the dimension increases exponentially. However, by applying the SVD technique, one can reduce the dimension by truncating the singular value spectrum and restore the MPS description after each time step as shown in Fig. 2.4. Now the above

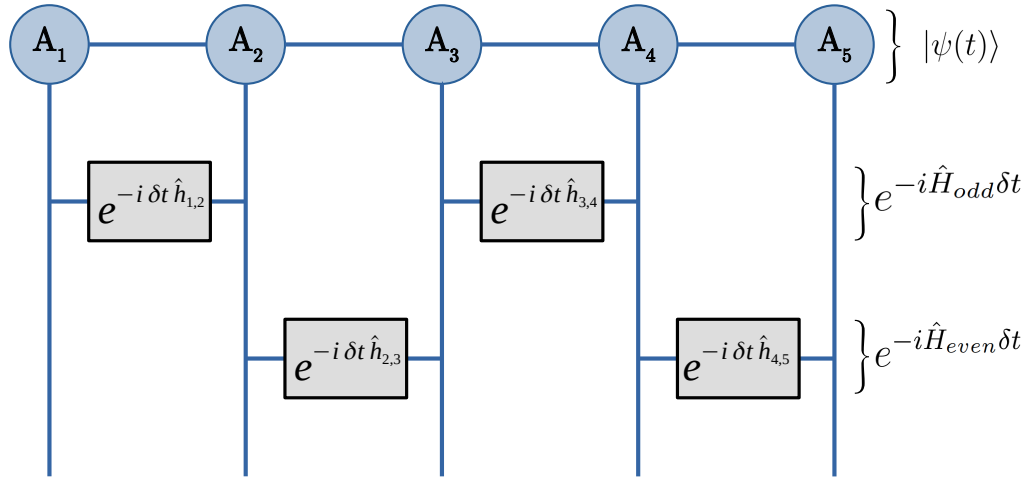


**Figure 2.3:** The graphical representation of the TEBD1 (first order) algorithm for a quantum lattice system of 5 sites with nearest neighbour interactions for a small time ( $\delta t$ ). The corresponding Hamiltonian  $\hat{H}$  can be written as,  $\hat{H} = \hat{H}_{even} + \hat{H}_{odd}$  where  $\hat{H}_{even} = \hat{h}_{2,3} + \hat{h}_{4,5}$  and  $\hat{H}_{odd} = \hat{h}_{1,2} + \hat{h}_{3,4}$ . The even and odd numbered two-site local time evolution operators are alternatively applied to the wave function represented by a matrix product state (MPS).

operation shown in Eq. 2.23 is repeated on the initial state  $|\psi(t)\rangle$  until we reach a final state at different time. This *Suzuki-Trotter* decomposition method works if the Hamiltonian contains only the nearest-neighbour terms. If the Hamiltonian contains the next nearest-neighbour terms, then the *Suzuki-Trotter* decomposition of the time evolution operator is done with the three-site local operators instead of two. Note that during the time evolution, in each step the entanglement builds up in the system. The error also builds up in the wave-function in the process of truncation in SVD. However, for dynamical evolution, the entanglement increases

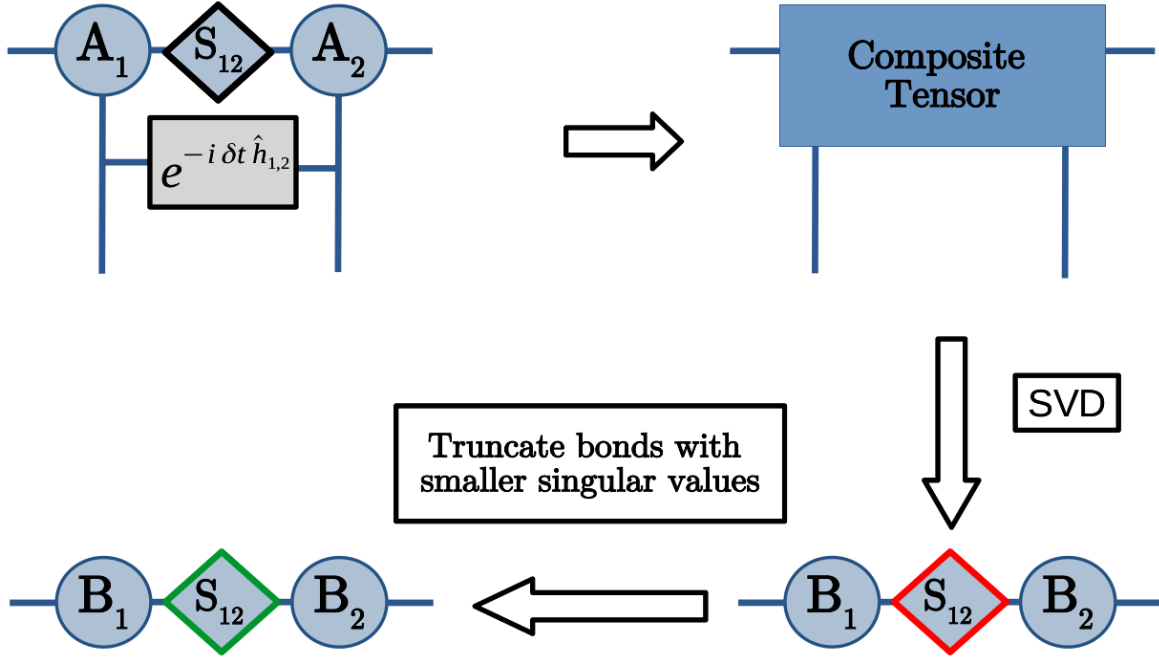


**Figure 2.4:** The figure shows a key step in TEBD1 is the contraction of a two site time-evolution operator into a pair of MPS tensors and splitting back into a new pair of MPS tensors with smaller singular values.

linearly in the system with time [135], which may not be a problem for most of the systems. Apart from this, errors also arise from the *Suzuki-Trotter* decomposition, which is of the order of  $\mathcal{O}(\delta t)$ . This error can be reduced by considering a very short time step  $\delta t$ . The error in the *Suzuki-Trotter* decomposition can be further reduced by considering higher-order decomposition (TEBDn). For example,  $\hat{U}_{exact}(\delta t)$  can be symmetrically decomposed as

$$\begin{aligned} \hat{U}_{exact}(\delta t) &= e^{-i\hat{H}\delta t} \\ &\approx e^{-i\hat{H}_{even}\frac{\delta t}{2}} e^{-i\hat{H}_{odd}\delta t} e^{-i\hat{H}_{even}\frac{\delta t}{2}} + \mathcal{O}(\delta t^3) \\ &= \hat{U}_{TEBD2} + \mathcal{O}(\delta t^3). \end{aligned} \quad (2.24)$$

In this case, error associated in each step is the of order of  $\mathcal{O}(\delta t^3)$  and error in time  $T$  is  $\frac{T}{\delta t} \times \mathcal{O}(\delta t^3) = \mathcal{O}(\delta t^2)$ , hence the error is of the second order.

In this thesis, we have employed the exact method for time-evolution of an initial state under the influence of a time independent Hamiltonian in Chapter 3 and Chapter 5. In Chapter 4, the TEBD simulations are carried out using the open source MPS (OSMPS) library [136, 137]. Where we have employed the TEBD method for time evolution with 4<sup>th</sup> order Trotterized two site gates and used the time step of  $0.01(J^{-1})$ .

## Chapter 3

# Two-component quantum walk in one-dimensional lattice with hopping imbalance

As discussed in Chapter 1, the QW of the two-component system may exhibit novel scenarios due to various competing interactions. Exploiting the experimental advances in creating and manipulating two-component quantum gases in optical lattices, we study the physics characterizing the QW of a two-component system in a one-dimensional lattice. To this end, we consider a system of two interacting particles of different hopping strength or mass. We show that the combined effect of hopping imbalance and interaction exhibits interesting physics in the two particles QW. Moreover, we show that the choice of initial states also plays an important role in the QW in such hopping imbalanced systems. Before going to the details of our studies, we briefly highlight the important findings which emerge from our analysis. We show that when the two particles start the QW from the same site, a repulsively bound pair [2] is formed as a function of inter-particle interaction - a phenomenon similar to the case of two identical particles [3, 96]. However, when the two particles start from two nearest neighbor sites, then the wavefunction of the fast component transmits through the slow component in the absence of interaction. With the increase in interaction, the fast component completely gets reflected from the slower one before forming a weak doublon in the limit of weak interaction. However, when the walkers are a few sites apart, the behaviour is similar to the previous case, except that the doublon formation is not so prominent. Interestingly, when the two particles are initially located far from each other, then both the particles feel the effect of the interaction and reflect from each other.

### 3.1 Model and approach

The Hamiltonian for the model which describes the system under consideration is given by;

$$H = - \sum_{\langle i,j \rangle, \sigma} J_{\sigma} (a_{i,\sigma}^{\dagger} a_{j,\sigma} + H.c.) + U \sum_i n_{i,\downarrow} n_{i,\uparrow} \quad (3.1)$$

where  $a_{i,\sigma}^{\dagger}$  ( $a_{i,\sigma}$ ) is the creation (annihilation) operator of the two components denoted as  $\sigma = \downarrow, \uparrow$ .  $U$  is the inter-component interaction strength and  $n_{i,\sigma} = a_{i,\sigma}^{\dagger} a_{i,\sigma}$  is the number operator at  $i$ 'th site corresponding to each component  $\sigma$ . Here,  $J_{\sigma}$  represents the nearest neighbor hopping matrix element for the component  $\sigma$ . The two components are distinguished from each other by introducing the hopping imbalance in the system. For convenience we define  $\delta = J_{\downarrow}/J_{\uparrow}$  and the hopping imbalance in the system is incorporated by setting  $\delta \neq 1$ . In our calculations, we consider  $J_{\uparrow} > J_{\downarrow}$  and set  $J_{\uparrow} = 1$  as the energy scale which makes all the physical quantities dimensionless. Due to the presence of one particle from each component, the quantum statistics of individual components can be neglected.

Our studies are based on the continuous-time quantum walk (CTQW) approach [22, 138, 139] which is based on the dynamical evolution of an initial state under the influence of a time independent Hamiltonian as shown in Eq.3.1 as

$$|\Psi(t)\rangle = e^{-iHt/\hbar} |\Psi_0\rangle \quad (3.2)$$

where,  $|\Psi_0\rangle$  is the initial state. For our studies we consider different initial states depending upon the initial positions of the particles. Hereafter, we refer to the CTQW as only QW for convenience.

In order to understand the physics of the system, we primarily compute two important physical quantities such as the expectation value of the on-site number operator as

$$\langle n_i(t) \rangle = \langle \Psi(t) | \sum_{\sigma} a_{i,\sigma}^{\dagger} a_{i,\sigma} | \Psi(t) \rangle \quad (3.3)$$

and the two-particle correlation function

$$\Gamma_{ij} = \langle a_{i,\uparrow}^{\dagger} a_{j,\downarrow}^{\dagger} a_{j,\downarrow} a_{i,\uparrow} \rangle \quad (3.4)$$

with the time evolved state  $|\Psi(t)\rangle$ . Note that  $\Gamma_{ij}$  is defined here as the correlation function between the two components and is different from the two-particle correla-

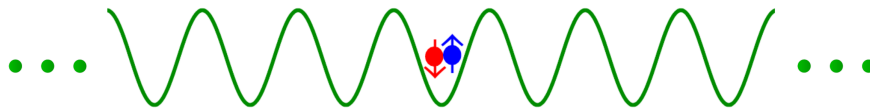


**Figure 3.1:** The schematic description of the initial state given in Eq. 3.5.

tion function defined in Refs. [3, 94, 96] for identical particles. For our analysis, we compute  $\Gamma_{ij}$  after an evolution time,  $t$ . Apart from these two important observables, we also analyze other quantities of interest, such as the half-length occupation, point of contact, and transmission coefficients which we describe in the following section. In our numerical simulations, the exact method for the dynamical evolution of the initial state has been employed where the lattice of length  $L = 41$  with open boundary conditions such that we have 20 sites on the left and right of the central sites with index “0”. We study the QWs by varying  $U$  from zero to a large repulsive limit in all the cases. Note that similar physics is expected for attractive interactions as well. By considering different values of  $\delta$  for different initial states, we study the QWs as discussed in detail in the following section.

## 3.2 Results

### 3.2.1 Two particles at the same site

In this section, we start with the QW of  $\uparrow$  and  $\downarrow$  particles which are initially located at the central site of the lattice as shown in Fig. 3.1. The initial state corresponding to this situation is given as

$$|\Psi(0)\rangle = a_{0,\uparrow}^\dagger a_{0,\downarrow}^\dagger |vac\rangle, \quad (3.5)$$

where  $|vac\rangle$  represents the empty state. Note that in the absence of any hopping imbalance i.e.  $\delta = 1$ , the system is similar to that of two indistinguishable interacting particles whose QW has already been studied in detail [3, 96]. It has been shown in both theoretical and experimental analysis that when  $\delta = 1$ , the two particles exhibit bosonic bunching as a function of interaction.

However, in the present case, the introduction of hopping imbalance, i.e.,  $\delta \neq 1$ , makes the particles distinguishable, which may exhibit different features in the QW. In this context, we first consider  $\delta = 0.2$  and vary the interaction strength  $U$  and analyze the spreading of the on-site particle density, which is depicted in Fig.3.2(a).

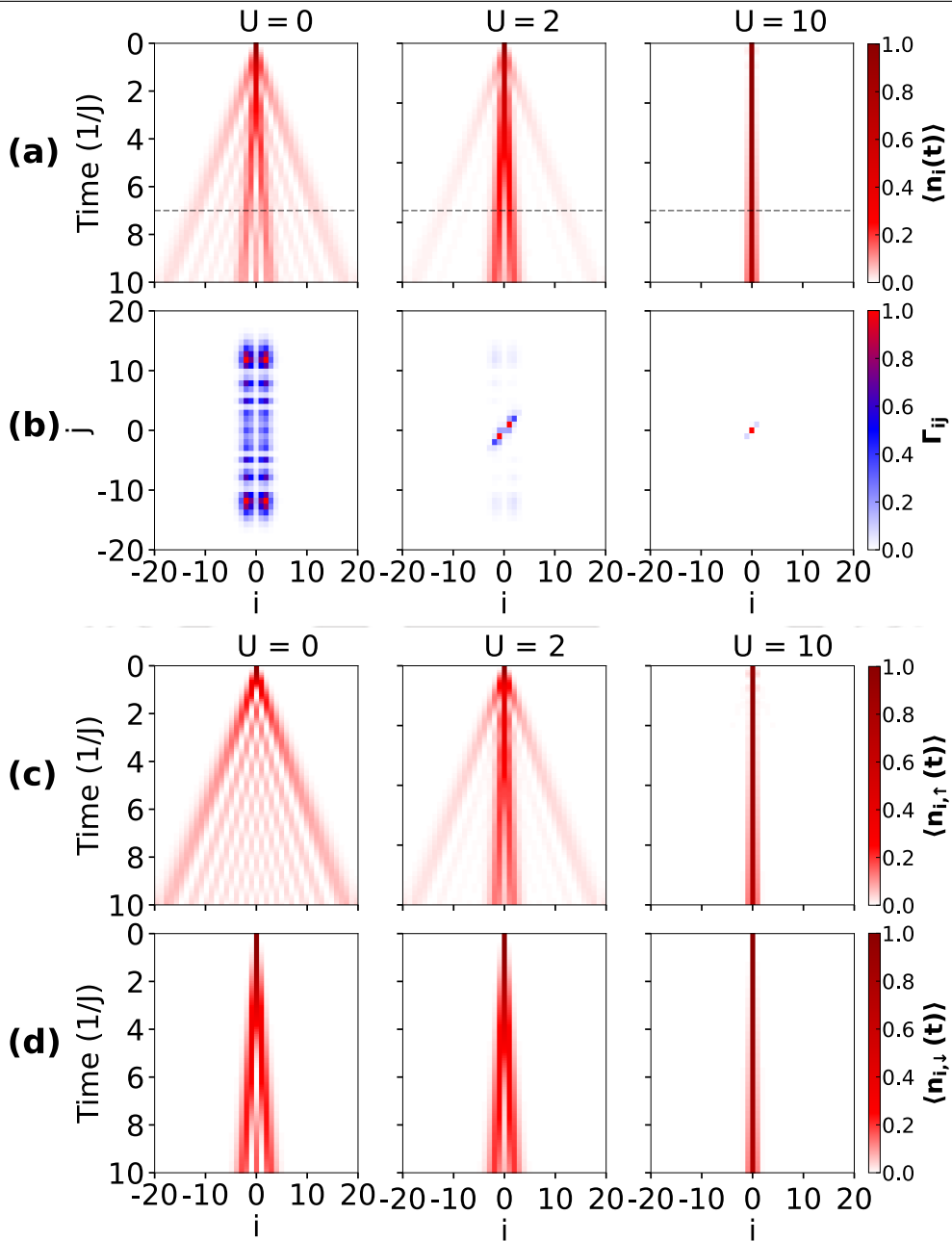


**Figure 3.2:** The figure shows the QW of two particles with the initial state given in Eq. 3.5 and  $\delta = 0.2$ . (a) Shows the time evolution of the normalized on-site density for different values of  $U$ . (b) Shows the normalized correlation functions  $\Gamma_{ij}$  at time  $t = 7J^{-1}$ , which correspond to the dashed lines in (a). (c) and (d) shows the on-site density evolution of  $\uparrow$  particle and  $\downarrow$  particle respectively corresponding to the QW shown in (a).

It can be seen that for vanishingly small interactions, the two particles exhibit independent particle QW. Due to the difference in hopping strength between the particles, the density profile of the  $\downarrow$  particle spreads at a slower rate compared

to the  $\uparrow$  particle, as expected. However, as the strength of interaction increases ( $U = 2$ ), the density profile exhibits simultaneous features of single and composite particle QW, a result similar to the ones discussed in Ref. [3, 27]. Further increase in interaction to a large value results in only a single profile corresponding to a slow density spreading, indicating that the two particles perform QW as a composite object. This feature in the QW can be attributed to the formation of doublon ( $\uparrow\downarrow$ ) due to the large onsite interaction [2] (see Fig. 3.9(a)). Hence, for stronger interaction, the QW of an effective doublon appears, which can be seen as a very slow evolution of the density profile in Fig. 3.2(a) for  $U = 10$ .

This feature of doublon formation can be clearly seen by separately looking at the evolution of individual particle's on-site densities  $\langle n_\sigma \rangle$  over the lattice. Clearly, with increasing  $U$ , the spreading of both the  $\uparrow$  and  $\downarrow$  particles become slower and identical to each other for large values of  $U$  as depicted in Fig. 3.2(c) and Fig. 3.2(d) respectively. An accurate insight about this doublon formation can be understood by analyzing the two-particle correlation matrix  $\Gamma_{ij}$  defined in Eq. 4.2. We calculate  $\Gamma_{ij}$  after evolving the initial state to  $t = 7J^{-1}$  (indicated by the dashed line in Fig. 3.2(a)) and plot it in Fig. 3.2(b) for different  $U$  considered in Fig. 3.2(a). At  $U = 0$ , the two-particle correlation matrix shows four peaks at four different locations. This feature is different from the  $\delta = 1$  case where the four peaks appear at four symmetric positions [96] as the wave functions of each non-interacting particle spread the same distance from the center on either side. However, due to the hopping imbalance, the spreading of the wave functions is not identical for the two particles, and this results in an asymmetry in the position of the peaks in the two-particle correlation matrix. By increasing  $U$ , the diagonal part of the matrix start to dominate, and eventually, for large  $U$ , only the dominating diagonal part survives, which indicates the formation of doublon (see Fig. 3.2(b)). To further

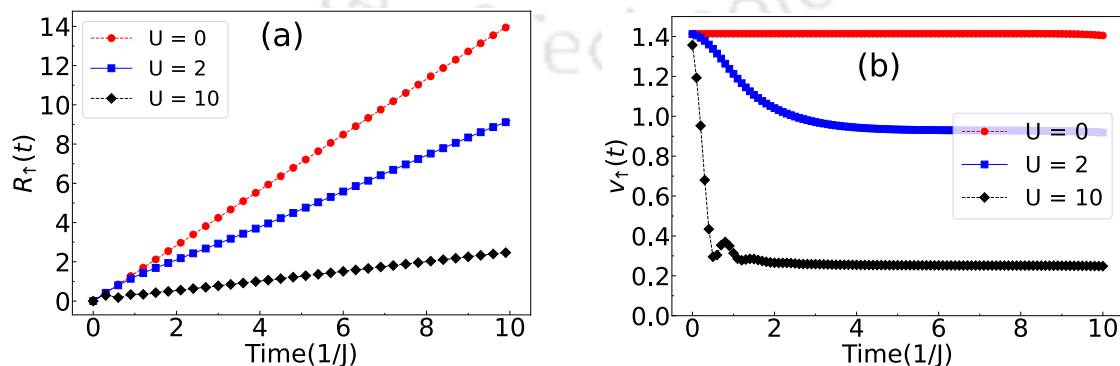


**Figure 3.3:** (a)  $R(t)$  and (b)  $v(t)$  are plotted for  $U = 0, 2$  and  $10$  corresponding to the expansion of the wave function of  $\uparrow$  particle when  $\delta = 0.2$ .

### Chapter 3. Two-component quantum walk in one-dimensional lattice with hopping imbalance

complement the doublon formation we track the wave function expansion velocity as

$$v_\sigma(t) = R_\sigma(t)/t, \quad \text{where } R_\sigma(t) = \left[ \sum_i (i - i_0)^2 \langle n_{i,\sigma}(t) \rangle \right]^{1/2}, \quad (3.6)$$

is the root mean-square displacement of the wave function and  $i_0$  is the central site. In the limit of strong imbalance, the expansion of  $\downarrow$  particle slow. Hence, to check the slowing down of the composite system we plot  $R_\uparrow(t)$  and  $v_\uparrow(t)$  respectively of the  $\uparrow$  particle wave function for different values of  $U = 0, 2, 10$  in Fig. 3.3(a) and Fig. 3.3(b) respectively. It can be seen for  $U = 0$ , the expansion is fast which gradually slows down as  $U$  increases. For  $U = 10$ , the time evolution of  $v_\uparrow(t)$  is extremely slow indicating the QW of bound pair with reduced effective hopping proportional to  $(J_\uparrow J_\downarrow)/U$ . Although the slow spreading of the wavefunction indicates

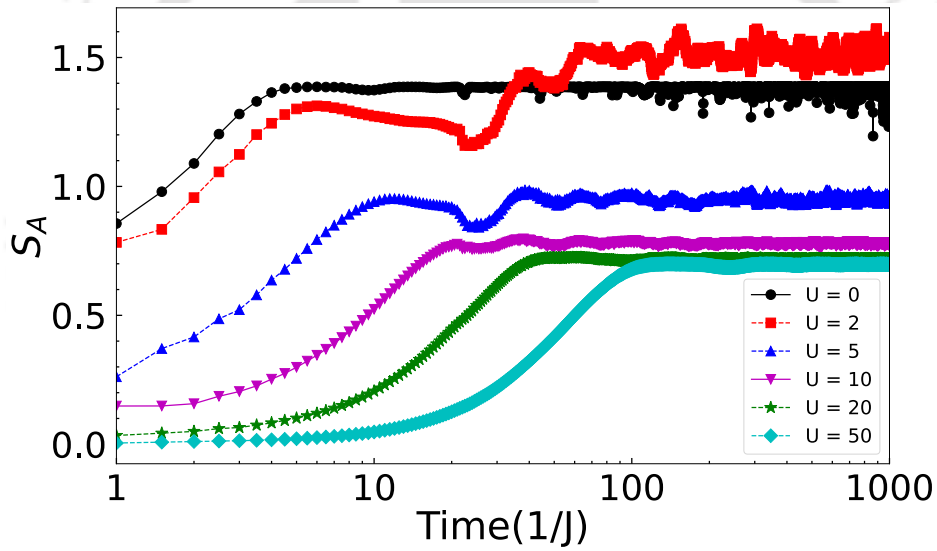


**Figure 3.4:** The figure shows the time evolution of  $S_A(t)$  for  $U = 0, 2, 5, 10, 20, 50$ .

a possible localization transition [27, 140], we rule out this possibility by computing the entanglement entropy defined as

$$S_A(t) = -\text{Tr}[\rho_A(t) \ln \rho_A(t)] \quad (3.7)$$

by dividing the system into two equal subsystems  $A$  and  $B$  and computing the reduced density matrix  $\rho_A(t)$  as

$$\rho_A(t) = \text{Tr}_B(|\psi(t)\rangle\langle\psi(t)|). \quad (3.8)$$

We plot the time evolution of  $S_A(t)$  for different values of  $U = 0, 2, 5, 10, 20, 50$  in Fig. 3.4 for  $\delta = 0.2$ . The entanglement entropy grows initially for all values of  $U$  but eventually saturates in the long time evolution indicating no localization [27].

Note that the feature of doublon formation is not due to the hopping imbalance, rather it is solely due to the inter-component interaction. However, the condition  $\delta \neq 1$  can influence the doublon formation due to the difference in kinetic energies between the particles. To further understand the effect of hopping imbalance, we check the QW for other values of  $\delta$  such as  $\delta = 0.4, 0.6$  and  $0.8$ . For all the cases, the features in the QW remain qualitatively similar (not shown) but the signatures of doublon formation appear at stronger interaction strengths for larger values of  $\delta$ . To quantify the doublon formation, we compute the quantity defined as

$$P = \sum_i \Gamma_{ii} = \sum_i n_{i,\downarrow} n_{i,\uparrow} \quad (3.9)$$

from the diagonal part of the two-particle correlation matrix  $\Gamma_{ij}$  during the time evolution. In our case, we compute  $P$  at time  $t = 7J^{-1}$  for each values of  $\delta$  and plot them as a function of  $U$  in Fig. 3.5(a). The formation of doublons can be inferred from the behavior of  $P$ , which asymptotically approaches unity with an increase in interaction strength. For comparison, we show  $P$  for the two limiting cases, i.e.,  $\delta = 0$  and  $1$ , which correspond to fully imbalanced and balanced cases. From the figure, it can be easily seen that although the effect of  $\delta$  on the pair formation is not so significant, for strong imbalance (small  $\delta$ ) the doublon formation happens at a smaller  $U$  due to small effective hopping. To further complement the dependence

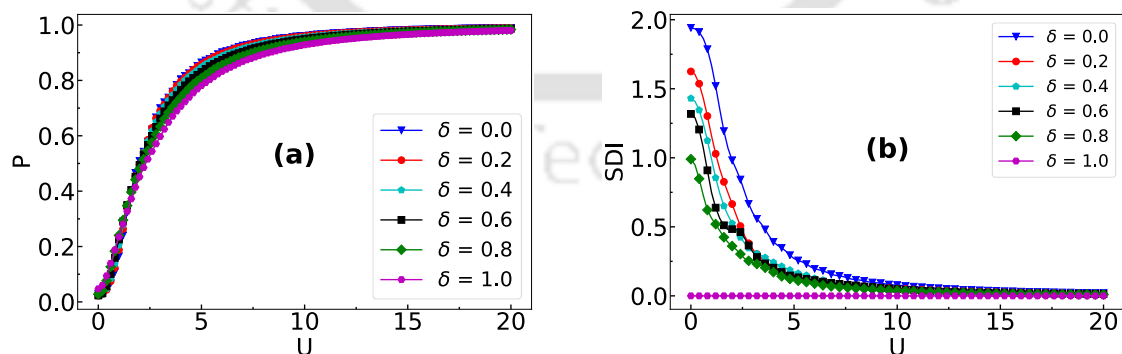


**Figure 3.5:** Figure shows the behaviour of (a)  $P$  and (b)  $SDI$  as a function of  $U$  for different  $\delta$  after a time evolution of the initial state given in Eq. 3.5 up to  $t = 7J^{-1}$ .

of doublon formation on  $\delta$  and  $U$  we calculate the spatial density imbalance (SDI)

between the two components which we define as

$$SDI = \sum_i |n_{i,\uparrow} - n_{i,\downarrow}|. \quad (3.10)$$

We plot the values of  $SDI$  as a function of  $U$  for different  $\delta$  in Fig. 3.5(b), calculated at time  $t = 7J^{-1}$  for the initial state given in Eq. 3.5. It can be seen that for all the cases of hopping imbalance, the values of  $SDI$  are finite for smaller  $U$  and eventually vanish in the regime of large  $U$ . While the vanishing of the  $SDI$  for large  $U$  is due to the doublon formation - a process similar to the balanced case ( $\delta = 1$ ), the finite values of  $SDI$  for smaller values of  $U$  can be attributed to the hopping imbalance.

### 3.2.2 Two particles at two different sites

This section studies the effect of hopping imbalance and interaction on the QW of two particles initially located at two different sites. We show that this situation reveals interesting physics compared to the one discussed in the previous section, where the effect of interaction was noticed in the form of doublon formation. To this end, we consider different initial states which can describe various aspects of the QW at different parameter regimes. In particular we consider three initial states which are given by

$$|\Psi(0)\rangle = a_{0,\uparrow}^\dagger a_{1,\downarrow}^\dagger |vac\rangle \quad (3.11)$$

where the particles are at the nearest neighbor (Fig. 3.6(a)),

$$|\Psi(0)\rangle = a_{-2,\uparrow}^\dagger a_{2,\downarrow}^\dagger |vac\rangle \quad (3.12)$$

where there are three empty sites between the particles (Fig. 3.6(b)) and

$$|\Psi(0)\rangle = a_{20,\uparrow}^\dagger a_{20,\downarrow}^\dagger |vac\rangle \quad (3.13)$$

where the particles are initially located at two edges of the lattice (Fig. 3.6(c)). Although we have considered other initial states by varying the distance between the particles in our analysis, the above three states can reveal all the relevant physics. In the following we will mainly focus on the QW for all the three different cases mentioned above by analyzing various relevant physical quantities such as the evolution of density, correlation matrix and transmission coefficients. The results arising due to the other initial states will be highlighted when necessary.

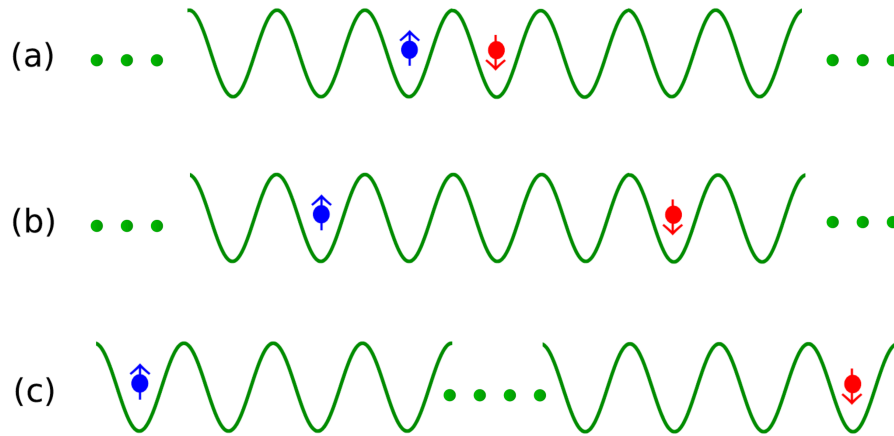


**Figure 3.6:** (a), (b) and (c) depict the schematic description of the initial states given in Eq. 3.11, Eq. 3.12 and Eq. 3.13 respectively.

### 3.2.2.1 Density evolution

First, we study the behaviour of the on-site densities in the two particles QW by considering different values of  $\delta$  and by varying  $U$ . The time evolution of  $\langle n_i \rangle$  with the initial states given in Eq. (3.11 - 3.13) are depicted in Fig. 3.7(a-c), respectively. From the figure, one can see a marked difference compared to the situation where the two particles are initially located at the same site (see Fig. 3.2(a)). It can be noticed that there also exist some similarities between the two scenarios at vanishingly small interaction when both the components perform independent particle QWs and the  $\uparrow$  particle (left) spreads faster compared to the  $\downarrow$  particle (right). For finite  $U$ , both the particles start to interact with each other after a certain time and position, leading to interesting features in the QW.

When the two particles are initially located at the adjacent sites (Eq. 3.11 and Fig. 3.6(a)), for  $U = 0$  the  $\uparrow$  and  $\downarrow$  particles spread independently of each other as can be seen from Fig. 3.7(a). For finite but weak  $U = 2$ , two different profiles corresponding to slow and fast spreading appear in the QW. This situation indicates the contribution from both single and doublon density evolution [3, 27]. With further increase in the  $U$ , the two particles reflect from each other and the situation is similar to the anti bunching of identical bosons [3, 96]. To clearly understand this behaviour we plot the time evolution of  $P$  defined in Eq. 3.9 for different values of  $U = 0, 2, 10$  in Fig. 3.8(a-c), respectively. Clearly, the probability of pair formation for  $U = 0$  and  $U = 10$  vanishes with time which remains finite for  $U = 2$ . The initial growth of  $P$  in each case is due to the finite overlap of the two wave functions.

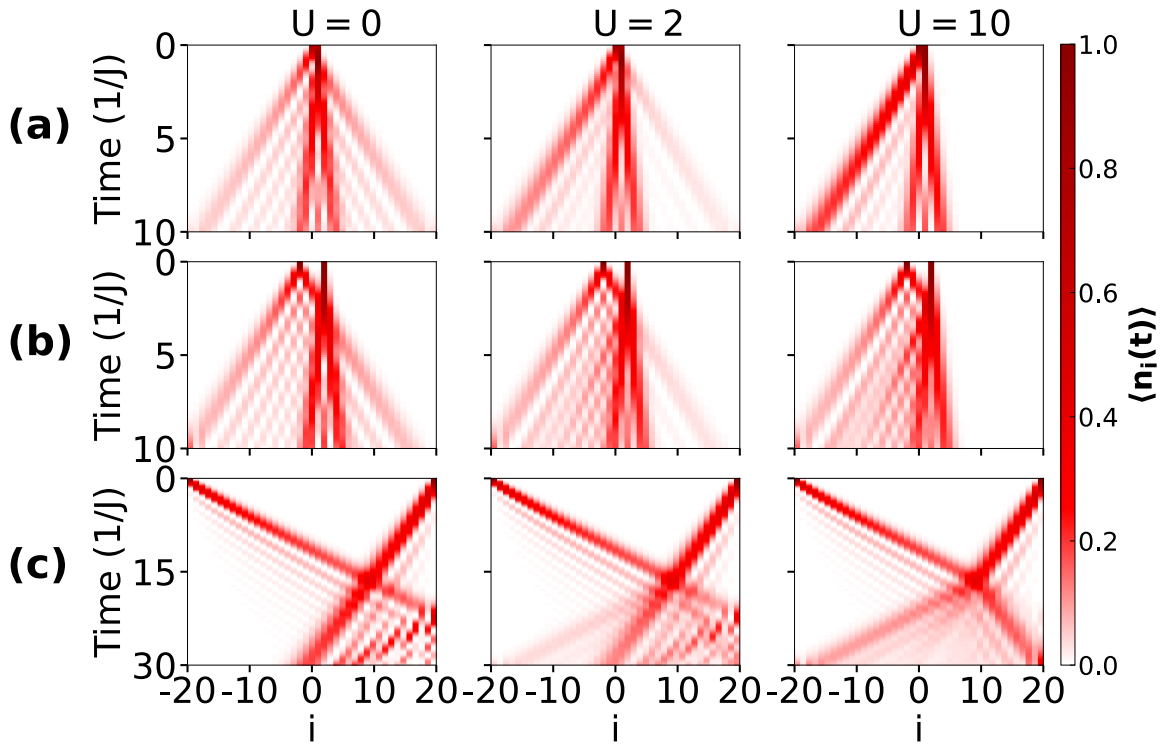


**Figure 3.7:** Figure shows the QWs for different initial states and different values of  $U$ . Here (a), (b) and (c) depict the total density (normalized) evolution for the three initial states Eq. 3.11, Eq. 3.12 and Eq. 3.13 respectively. For results depicted in (a) and (b)  $\delta = 0.2$  and for (c)  $\delta = 0.4$  has been considered.

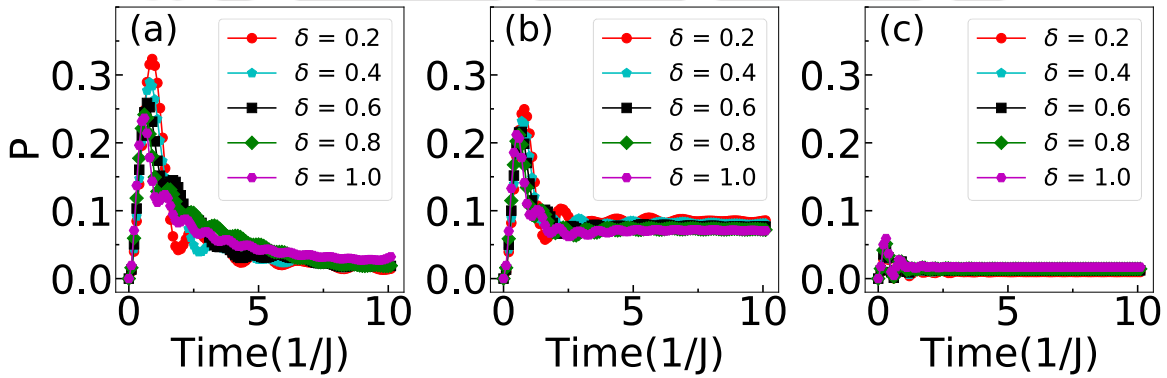


**Figure 3.8:** The figure shows the time evolution of  $P$  for different values of  $\delta$  and (a) for  $U = 0$ , (b) for  $U = 2$  and (c) for  $U = 10$ .

On the other hand, when the two particles are few sites apart ((Eq. 3.12 and Fig. 3.6(b)) and the interaction is finite but weak, the  $\downarrow$  particle acts like a barrier and as a result, the density spreading of the  $\uparrow$  particle shows reflected as well as transmitted components in the propagation as shown in Fig. 3.7(b). As the inter-

action becomes stronger and stronger, the transmission ceases to occur, and the  $\uparrow$  particle wave function gets completely reflected for large enough  $U$ . Unlike the previous case, the pair formation is not stable during the time evolution (not shown).

The QW for the initial state (Eq. 3.13 and Fig. 3.6(c)), however, gives a very different outcome as can be seen from Fig. 3.7(c). Since the particles are initiated at the edges, we get a unidirectional spread of each particle's wave function. Due to the hopping imbalance, the density profiles of two particles meet at a point away from the center toward the slow moving particle ( $\downarrow$ ). When  $U = 0$ , the two particles move independently, and their wave functions transmit through each other without influencing the QWs of the individual particles. On the other hand, the onset of interaction  $U$  leads to the reflection of both the components from each other by reducing the transmission. It can be easily seen that the effect of interaction on the  $\downarrow$  particle is drastic for this case compared to the other two cases. For clarity we also show the on-site density distribution over the entire lattice at a particular instant during the time evolution in Fig. 3.9(b-d) for the initial states shown in Eq. (3.11 - 3.13). The effect of interaction can be clearly seen as we move from weak to strong interaction regime (I to III) in Fig. 3.9. For comparison, we also show the situation when the two particles start from the central site in Fig. 3.9(a).

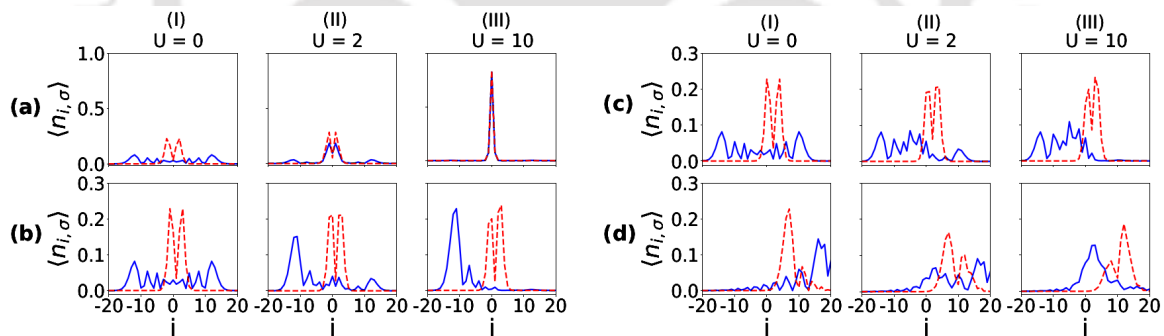


**Figure 3.9:** Figure shows the onsite densities of  $\downarrow$  (dashed curves) and  $\uparrow$  particle (solid curves) in the lattice for different regimes of interaction such as small (I), intermediate (II) and large (III) after evolving the initial state up to a certain time ( $t$ ). (a-d) correspond to the initial states given in Eq. 3.5, Eq. 3.11, Eq. 3.12 and Eq. 3.13 respectively. For (a-c)  $t = 7J^{-1}$ ,  $\delta = 0.2$  and for (d)  $t = 20J^{-1}$ ,  $\delta = 0.4$  are considered.

The effect of interaction on the QW can be further understood by analyzing the evolution of the half-length occupation of the individual components which are defined as

$$N_{\frac{L}{2},\uparrow} = \sum_{i \leq \frac{L}{2}} n_{i,\uparrow} \quad \text{and} \quad N_{\frac{L}{2},\downarrow} = \sum_{i \leq \frac{L}{2}} n_{i,\downarrow} \quad (3.14)$$

### Chapter 3. Two-component quantum walk in one-dimensional lattice with hopping imbalance

for  $\uparrow$  and  $\downarrow$  component respectively. The time evolution of  $N_{\frac{L}{2},\uparrow}$  (red dashed curves) and  $N_{\frac{L}{2},\downarrow}$  (blue solid curve) for different values of interactions such as  $U = 0$  (circles),  $U = 2$  (up triangles) and  $U = 10$  (squares) are plotted in Fig. 3.10(a-c) for the initial states and hopping imbalance considered in Fig. 3.7(a-c) respectively. From the figures it can be seen that initially  $N_{\frac{L}{2},\uparrow} = 1$  and  $N_{\frac{L}{2},\downarrow} = 0$  as the  $\uparrow$  and the  $\downarrow$  particles reside in the left and the right halves of the system respectively. As the time progresses, different features are visible in the time evolution of  $N_{\frac{L}{2},\uparrow}$  and  $N_{\frac{L}{2},\downarrow}$  for different initial states and interactions due to hopping imbalance. In Fig. 3.10(a), for

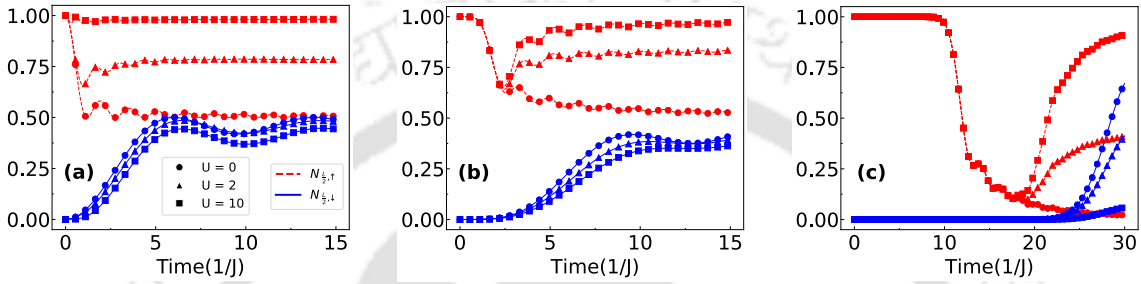


**Figure 3.10:** Evolution of half-length occupation  $N_{\frac{L}{2},\uparrow}$  (dashed curves) and  $N_{\frac{L}{2},\downarrow}$  (solid curves) are shown for different interaction strengths such as  $U = 0$  (circles),  $U = 2$  (triangles) and  $U = 10$  (squares). (a), (b) and (c) correspond to the initial states given in Eq. 3.11, 3.12 and 3.13 respectively. For (a-b)  $\delta = 0.2$  and for (c)  $\delta = 0.4$  is considered.

$U = 0$  the value of  $N_{\frac{L}{2},\uparrow}$  ( $N_{\frac{L}{2},\downarrow}$ ) initially starts to decrease (increase) as both the wave functions transmit through each other. Eventually both the quantities saturate to a value close to 0.5 due to no reflection from each other. Finite interactions however, lead to reflection of wave functions and hence  $N_{\frac{L}{2},\uparrow}$  saturates to different values larger than 0.5. For sufficiently strong  $U$ ,  $N_{\frac{L}{2},\uparrow}$  saturates to unity due to complete reflection from the  $\downarrow$  particle. These features can be seen from the curves corresponding to  $U = 2$  and 10 in Fig. 3.10(a). Note that the effect on the  $\downarrow$  particle in this process is negligible. For the second case (Fig. 3.10(b)), while the long time evolution of  $N_{\frac{L}{2},\uparrow}$  and  $N_{\frac{L}{2},\downarrow}$  exhibit features similar to the case shown in Fig. 3.10(a), the short time evolution behave differently. Up to  $t \sim 1J^{-1}$ , the values of  $N_{\frac{L}{2},\uparrow}$  ( $N_{\frac{L}{2},\downarrow}$ ) remain equal to 1(0). This is because of the presence of empty sites between the particles at  $t = 0$  for which the  $\uparrow$  particle wave function remains entirely on the left half of the lattice before spreading into the right half after  $t = 1J^{-1}$ . During this time, the occupation by the  $\downarrow$  particle on the left half of the lattice remains zero. After  $t = 1J^{-1}$ , however, the values of  $N_{\frac{L}{2},\uparrow}$  suddenly decrease up to  $t \sim 2J^{-1}$  and then start to increase for values of  $U \neq 0$ . The decrease in the values of  $N_{\frac{L}{2},\uparrow}$  is due to the hopping imbalance for which the  $\uparrow$  and  $\downarrow$  particle wave function interact at a point right from the center of the lattice. Hence, there is a finite propagation of the  $\uparrow$  particle wave function

towards the right half of the lattice leading to the decrease in  $N_{\frac{L}{2},\uparrow}$ . After  $t = 2J^{-1}$ , the values of  $N_{\frac{L}{2},\uparrow}$  saturate at higher values as already discussed. On the other hand the values of  $N_{\frac{L}{2},\downarrow}$  increase and saturate after  $t = 1J^{-1}$ . For the case shown in Fig. 3.10(c), the features are similar to the one shown in Fig. 3.10(b) except that the saturation occurs at a later time due to the largest distance between the particles at the initial position. Note that in our analysis we don't analyze the physics for a very long time evolution. Hence, the contributions arising from reflections from the boundaries are ignored in all the cases except the last case where the quantum walkers are initially located at the edges.

### 3.2.2.2 Correlation function

The two-particle correlation function also shows interesting behavior due to the hopping imbalance and interaction. The  $\Gamma_{ij}$  are computed for different values of  $U$  considered in Fig. 3.7 and plotted in Fig. 3.11(a-c) for the initial states given in Eq. (3.11 - 3.13) respectively. In Fig. 3.11(a-b), for  $U = 0$ ,  $\Gamma_{ij}$  (calculated at time  $t = 7J^{-1}$ ) shows four peaks due to the fact that the particle wave functions spread equal distance in both directions from the initial position. With the increase in  $U$ , the elements in the upper triangle along with the diagonal elements of the  $\Gamma_{ij}$  matrix start to decrease and eventually vanish for large enough  $U$ . This is because the two particles avoid each other due to strong repulsion. When the two particles start from the edges Eq. 3.13, the correlation matrix  $\Gamma_{ij}$  behaves differently compared to the other two cases. In Fig. 3.11(c), we plot  $\Gamma_{ij}$  at time  $t = 20J^{-1}$ , for which the corresponding local densities of the individual components  $\langle n_\sigma \rangle$  are shown in Fig. 3.9(d). Since for vanishing  $U$  the wave functions transmit through each other and travel to the opposite directions, we see only one peak in the correlation matrix. However, for strong enough interaction ( $U > 10$ ), the peak in the correlation matrix flips to a different position because of strong repulsion between the particles which is also visible from Fig. 3.7(c). Note that there is no doublon formation in these cases.

### 3.2.2.3 Effect of distance

From the above discussion, it is understood that the features in the time evolution of densities in the presence of hopping imbalance and interaction have a strong dependence on the initial states. The point of contact of the two particle wave function strongly depends on the distance between the particles. In order to examine

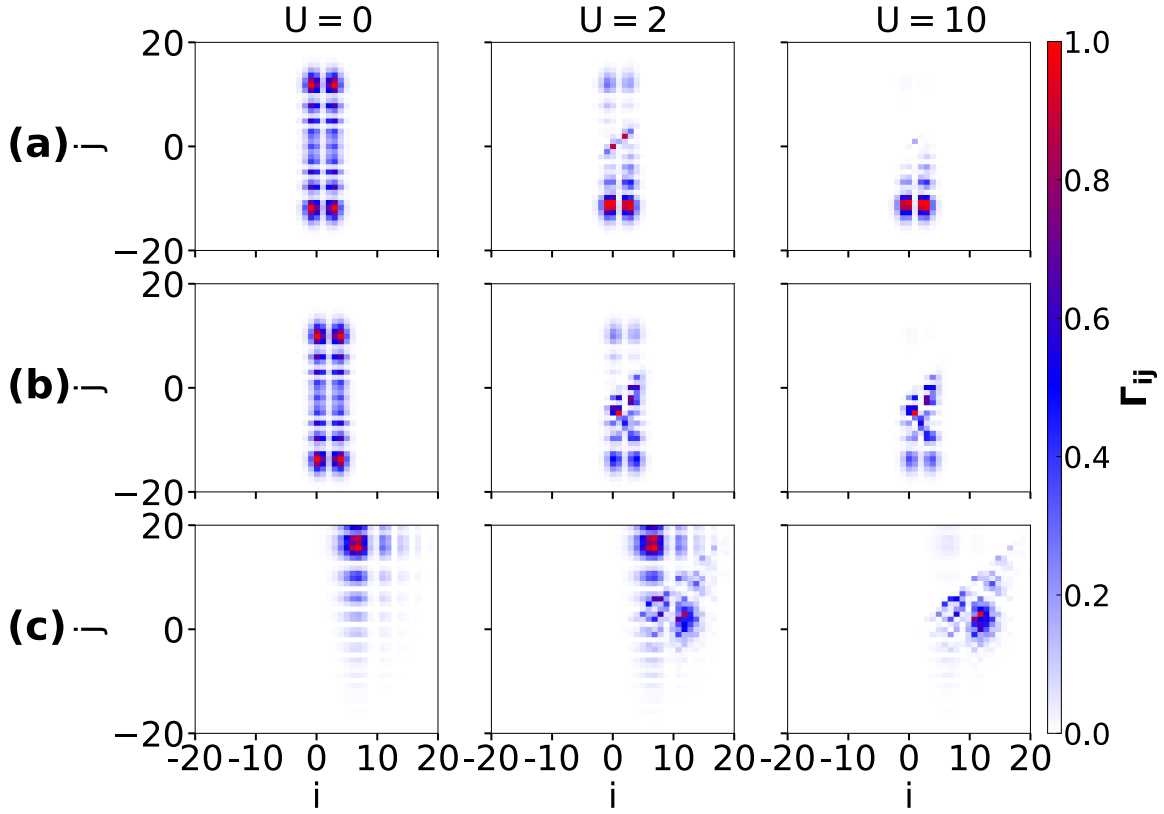


**Figure 3.11:** Normalized correlation functions  $\Gamma_{ij}$  are plotted corresponding to the parameters considered in Fig. 3.7 at a particular instant during the time evolution.  $\Gamma_{ij}$  in (a), (b) and (c) correspond to the initial states of Eq. 3.11, Eq. 3.12 and Eq. 3.13 respectively. While  $\Gamma_{ij}$  is computed at  $t = 7J^{-1}$  for (a) and (b), for (c) it is computed at  $t = 20J^{-1}$ .

this we study the effect of distance between the two particles at the initial position on the QW by defining a general initial state

$$|\Psi(0)\rangle = a_{-d,\uparrow}^\dagger a_{d,\downarrow}^\dagger |vac\rangle, \quad (3.15)$$

where  $d$  is the distance of the occupied sites from the central one. The point at which the two particles first meet can be computed by tracking the position where the occupancy of both the  $\uparrow$  and  $\downarrow$  particles becomes finite in the entire lattice for the first time during the time evolution. For this purpose we define a quantity

$$I_P = \sum_i \langle n_{i,\uparrow} n_{i,\downarrow} \rangle, \quad (3.16)$$

which becomes finite only when any site will have finite densities of both the components during the time evolution. The time evolution of  $I_P$  (red squares) for an exemplary initial state  $|\Psi_0\rangle = a_{-14,\uparrow}^\dagger a_{14,\downarrow}^\dagger |vac\rangle$  of non interacting particles ( $U = 0$ )

and  $\delta = 0.2$  is shown in Fig. 3.12(a). This clearly shows that  $I_P$  becomes finite

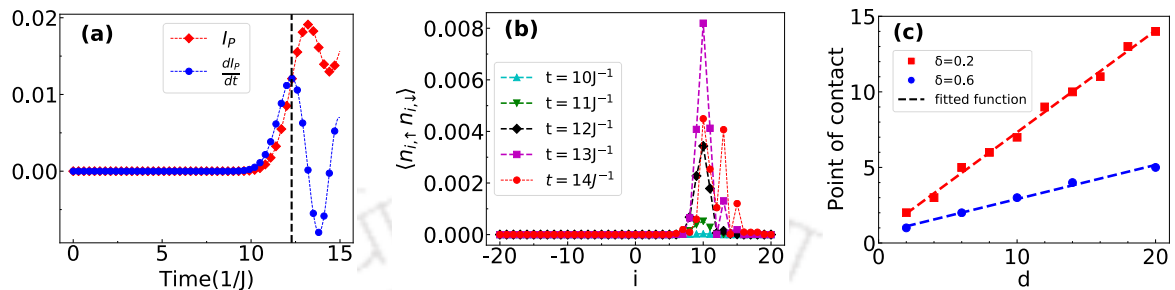


**Figure 3.12:** (a)  $I_P$  and  $\frac{dI_P}{dt}$  are plotted with respect to time. Black dashed line represents the time at which  $\frac{dI_P}{dt}$  is maximum. Here we consider the initial state  $|\Psi_0\rangle = a_{-14,\uparrow}^\dagger a_{14,\downarrow}^\dagger |vac\rangle$  and  $\delta = 0.2$ . (b) The point of contact is shown by plotting  $\langle n_{i,\uparrow}n_{i,\downarrow} \rangle$  with respect to the site at different times. The time  $t = 12.28J^{-1}$  corresponds to the black dashed line of (a). (c) Point of contact of the two-particle wave functions are plotted with different  $d$  of the initial state  $|\Psi_0\rangle = a_{-d,\uparrow}^\dagger a_{d,\downarrow}^\dagger |vac\rangle$ . The red squares and blue circles are the data for  $\delta = 0.2$  and  $0.6$ , respectively. The dashed lines are the fitted functions.

after a certain time of evolution indicating the point of contact between the two wave functions. The actual point of contact is not easy to estimate from the figure due to the smooth variation of  $I_P$  with time. To estimate the point of contact, we first plot  $dI_P/dt$  (blue circles) as a function of time and obtain the time of contact as the first peak in  $dI_P/dt$  which appears at  $t = 12.28J^{-1}$ . Then we plot  $\langle n_{i,\uparrow}n_{i,\downarrow} \rangle$  as a function of site index  $i$  for different  $t$  around  $t = 12.28J^{-1}$  such as  $t = 10J^{-1}$ ,  $11J^{-1}$ ,  $12J^{-1}$ ,  $13J^{-1}$  and  $14J^{-1}$  in Fig. 3.12(b). The appearance of large peaks at  $i = 10$  for  $t \geq 12$  is a clear indication of the point of contact. We repeat this procedure for different values of  $d$  and plot the point of contact as a function of  $d$  in Fig. 3.12(c) for two different values of  $\delta$ . These curves exhibit linear behaviour which can be attributed to the ballistic nature of the QW. Moreover, we find that the slopes of the fitted functions decrease with an increase in  $\delta$ . It is to be noted that the point of contact for all  $d$  and  $\delta$  is independent of  $U$  as expected. However, the dependence of  $U$  on  $d$  can only be realized after the point of contact which will be discussed in the following subsection.

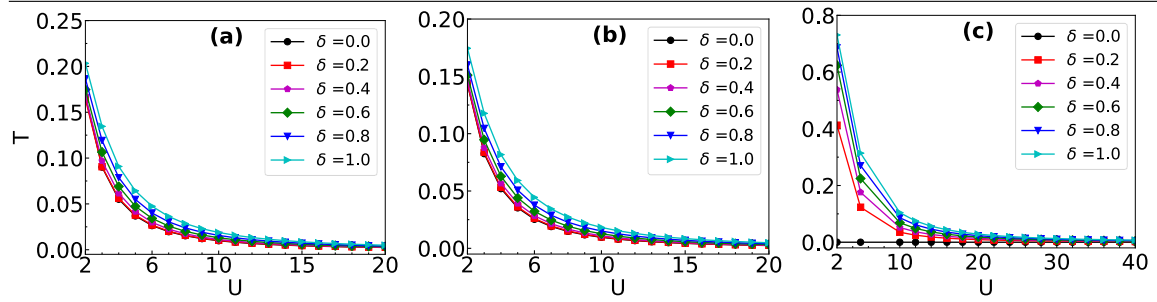


**Figure 3.13:** The transmission coefficient  $T$  is plotted with respect to  $U$  for different values of  $\delta$  by evolving the initial state  $|\Psi(0)\rangle$  to (a)  $t = 7J^{-1}$ , (b)  $t = 7J^{-1}$  and (c)  $t = 23J^{-1}$ . (a), (b) and (c) correspond to the results obtained using the initial states given in Eq. 3.11, Eq. 3.12 and Eq. 3.13 respectively.

### 3.2.2.4 Transmission coefficient

The effect of hopping imbalance on the QW is further studied by calculating the transmission coefficient defined as

$$T = \sum_{\substack{i,j \\ j>i}} \langle n_{i,\uparrow} n_{j,\downarrow} \rangle. \quad (3.17)$$

which is nothing but the sum over all the upper triangular elements of the correlation matrix. This provides an estimate of the probability of the existence of the  $\uparrow$  particle on the right side region of the  $\downarrow$  particle profile at a particular instant during the QW. In order to understand the behaviour of  $T$  of interacting particles with hopping imbalance, we plot  $T$  with respect to  $U$  for different values of  $\delta$  in Fig. 3.13 (a), (b) and (c) for three initial states given in Eq. 3.11, Eq. 3.12 and Eq. 3.13 respectively. In all these cases we observe that the values of  $T$  decrease with increase in  $U$  and gradually vanish in the limit of strong interactions. Moreover, a larger hopping imbalance (i.e. smaller  $\delta$ ) leads to a faster decay of  $T$ . This indicates that for a large (small) imbalance, the transmission ceases for a weak (strong) interaction  $U$ . This is because for small  $\delta$  the on-site density of the  $\downarrow$  particle at the point of contact during the QW is larger compared to the case of larger  $\delta$ . Hence, at the point of contact the effective interaction experienced by the  $\uparrow$  particle is stronger for smaller  $\delta$ . Note that in Fig. 3.13(c) for  $\delta = 0$ , the  $T$  is always zero because the  $\downarrow$  particle is localized at the edge (as  $J_{\downarrow} = 0$ ), and the  $\uparrow$  particle can never go past the edge due to the open boundary condition. It can be seen from Fig. 3.13 that the vanishing up of  $T$  is very slow as a function of  $U$  for all the cases considered. In order to obtain the value of critical interaction strength ( $U_c$ ) for no transmission or complete

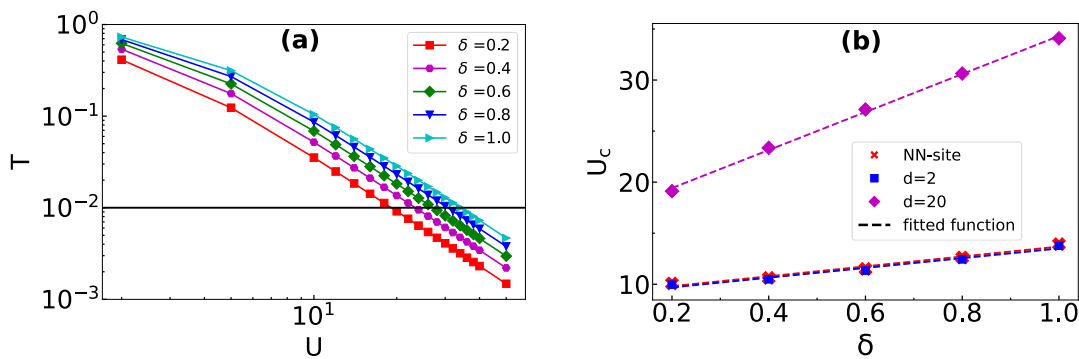


**Figure 3.14:** (a) The transmission coefficient  $T$  is plotted as a function of  $U$  for different values of  $\delta$  in the log-log scale for the initial state given in Eq. 3.13 at  $t = 23J^{-1}$ . The dashed line marks  $T = 10^{-2}$  which is considered as the critical  $T$  for zero transmission and its point of intersection with different curves are the corresponding  $U_c$ . (b) The plot between  $U_c$  and  $\delta$  is obtained by evolving the initial states given in Eq. 3.11 to  $t = 7J^{-1}$  (red stars), Eq. 3.12 to  $t = 7J^{-1}$  (blue squares) and Eq. 3.13 to  $t = 23J^{-1}$  (magenta diamonds).

reflection, we have re-plotted the  $T - U$  plot in the log-log scale (see Fig. 3.14(a)) and estimated  $U_c$  by assuming  $T = 10^{-2}$  as the condition for no transmission. Using the above method, we have calculated the values of  $U_c$  for different initial states and plotted them in the  $U_c - \delta$  plane in Fig. 3.14(b). The curves for different initial states exhibit the linear dependence of  $U_c$  with respect to  $\delta$ . Moreover, we observe that the critical strength and slope of the curves increase with increasing  $d$ . Note that in our analysis, we consider  $U > \max(J_{\uparrow}, J_{\downarrow})$  to see the effect of  $U$  on  $T$ .

### 3.3 Conclusions

We have studied the QW of a two-component system in the presence of interaction and hopping imbalance in a one-dimensional lattice. By considering different initial states depending on the positions of the particles ( $\uparrow$  and  $\downarrow$  where the  $\uparrow$  particle has higher hopping strength), we have analyzed the combined effect of hopping imbalance and inter-component interaction on the two-particle QW. We have found that when the two particles initially start from the central site of the lattice, the QW exhibits independent particle QWs to a QW of composite particles or doublon as a function of repulsive interactions. However, for the initial state with two particles at two different sites (a few sites apart), the  $\uparrow$  particle wave function gets reflected from the  $\downarrow$  particle's wave function for large enough interactions, and no doublon is formed. On the other hand, when the two particles start from the opposite ends of the lattice, the situation is completely different for strong interactions. In this

### Chapter 3. Two-component quantum walk in one-dimensional lattice with hopping imbalance

---

case, both the  $\uparrow$  and  $\downarrow$  particle wave functions significantly reflect from each other at a point close to the initial position of the  $\downarrow$  particle. While we obtain different behavior compared to the many-body limit depending upon the parameters of the model Hamiltonian, the phenomenon of zero transmission in the limit of large inter-component interaction resembles the phase separation which has been predicted in systems of binary atomic mixtures in optical lattices [115, 141, 142]. Moreover, we have obtained that the change in the initial position of the particles leads to a qualitative change in the results. These findings provide insights into the dynamical behavior of a mixture of two-component systems in periodic potential at the few particle levels. Due to the recent experimental progress in the controlled creation and manipulation of multi-component atomic mixtures in an optical lattice and the single-site addressing techniques, our prediction can, in principle, be simulated in quantum gas experiments. While the hopping imbalance can be indirectly obtained by considering a two-component atomic mixture of different masses such as  $^{87}\text{Rb}$  and  $^{41}\text{K}$  atoms [107], it will be impossible to tune the hopping imbalance to explore the physics in broader parameter space. Therefore, an appropriate platform can be the mixture of two hyperfine states of a particular atomic species in a state-dependent optical lattice where the hopping strengths of each internal state can be independently tuned [109, 121–123, 143].

## Chapter 4

# Signatures of non-trivial pairing in the quantum walk of two-component bosons

### 4.1 Introduction

Recent studies on periodic lattices show that the QWs of more than one indistinguishable particle exhibit non-trivial correlations due to Hanbury Brown-Twiss (HBT) interference [3, 96]. From theoretical and experimental studies, it is well established that when the walkers start from the same site, the individual particle wavepackets spread ballistically and symmetrically from their initial positions. However, when the walkers are at the two nearest neighbour (NN) sites, they propagate together, exhibiting the phenomenon of bosonic bunching. Further developments in studying the QWs of interacting particles have enabled us to gain insights into the combined effects of interactions, particle statistics, and strong correlations [94, 101, 126, 144, 145]. Interestingly, interactions between the particles lead to a completely different scenario in the QW, which has recently been studied in the context of the Bose-Hubbard models in one-dimension. [27, 96]. It has been shown that two strongly interacting bosons on a single site exhibit QW of bound bosonic pairs, whereas two NN bosons show a transition from bosonic to fermionic like spatial correlations and anti-bunching with an increase in onsite interaction [3, 146]. On the other hand, the QWs of two interacting distinguishable particles have also been explored in one-dimension [129, 147–149], exhibiting features qualitatively similar to the QW of indistinguishable particles.

An important inference that can be drawn from the existing findings is that

strongly interacting NN bosons don't form local pairs in their QW. However, in this chapter, we show that in the case of the QW of two-component bosons in one-dimension, non-trivial local bound pairs can be formed due to the interplay of inter- and intra-component interactions. By considering different initial states of more than two particles, we show that the quantum correlation along with competing interactions favors the formation of onsite inter-component bound pairs even if the two components start their QW from the NN sites. Depending on the initial conditions, the formation of bound pairs is more robust when suitable hopping asymmetry is introduced. Moreover, we obtain a re-entrant feature in the QW as a function of the inter-species interaction.

## 4.2 Model

Our analysis is based on the two-component Bose-Hubbard model which is given as

$$\begin{aligned}
 H = & - \sum_{\langle i,j \rangle, \sigma} J_{\sigma} (a_{i,\sigma}^{\dagger} a_{j,\sigma} + H.c.) + U_{\uparrow\downarrow} \sum_i n_{i,\uparrow} n_{i,\downarrow} \\
 & + \sum_{i,\sigma} \frac{U_{\sigma}}{2} n_{i,\sigma} (n_{i,\sigma} - 1)
 \end{aligned} \tag{4.1}$$

where  $a_{i,\sigma}^{\dagger}$  ( $a_{i,\sigma}$ ) are the creation (annihilation) operators of two different components  $\sigma \in (\uparrow, \downarrow)$  which can correspond to two different atoms or two hyperfine states of a single atom.  $n_{i,\sigma} = a_{i,\sigma}^{\dagger} a_{i,\sigma}$  is the number operator at the  $i^{\text{th}}$  site corresponding to individual component  $\sigma$ . Here,  $J_{\sigma}$  and  $U_{\sigma}$  are the NN hopping matrix elements and onsite intra-component interaction energies of the individual components  $\sigma$ , respectively. The inter-component interaction is denoted by  $U_{\uparrow\downarrow}$ . In our studies, we assume the two components as the two hyperfine states of a single atom in a state-dependent optical lattice [109]. This assumption leads to the condition  $U_{\uparrow} = U_{\downarrow} = U$  and we define  $\delta = J_{\downarrow}/J_{\uparrow}$  to introduce the hopping asymmetry between the states/components. Hopping asymmetry is ensured by setting  $J_{\uparrow} > J_{\downarrow}$  i.e.  $\delta < 1$  and we take  $J_{\uparrow} = 1$  as the energy scale.

We study the CTQW (hereafter referred as QW) by computing experimentally relevant quantities such as the onsite densities and the two-site correlation functions. The total onsite density is defined as  $n_i(t) = \langle \sum_{\sigma} a_{i,\sigma}^{\dagger} a_{i,\sigma} \rangle$ . Unlike the single-particle case [3, 94, 96], for the two-component system we compute both inter-species density-

density and intra-species two-particle correlation function defined as

$$\Gamma_{ij}^{\downarrow\uparrow}(t) = \langle n_{i,\downarrow} n_{j,\uparrow} \rangle \quad \text{and} \quad \Gamma_{ij}^{\sigma}(t) = \langle a_{i,\sigma}^{\dagger} a_{j,\sigma}^{\dagger} a_{j,\sigma} a_{i,\sigma} \rangle \quad (4.2)$$

respectively. These quantities are calculated with a time evolved state  $|\Psi(t)\rangle = e^{-iHt/\hbar}|\Psi(0)\rangle$ , where  $|\Psi(0)\rangle$  is some initial state. The time evolution is obtained by utilizing the Time Evolving Block Decimation (TEBD) method using the Matrix Product States (MPS) [150, 151] with appropriate approximations. In our analysis, we consider a system size of  $L = 41$  except for the case of long time evolution where we take  $L = 82$ .

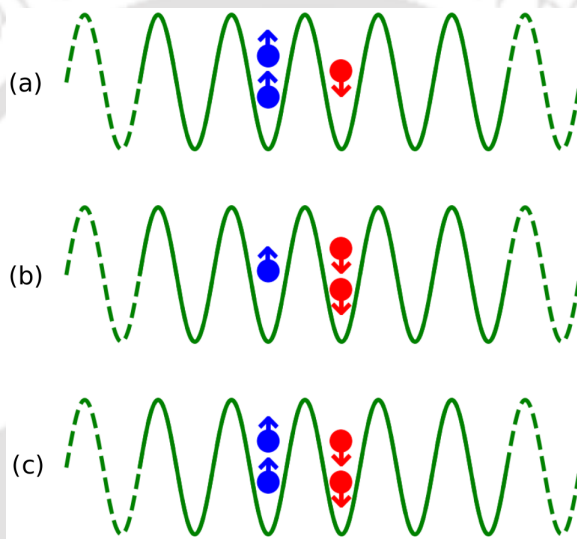


**Figure 4.1:** The lattice diagrams (a), (b) and (c) represent the initial state  $|\Psi(0)\rangle_{\text{I}} = a_{0,\uparrow}^{\dagger 2} a_{1,\downarrow}^{\dagger} |vac\rangle$ ,  $|\Psi(0)\rangle_{\text{II}} = a_{0,\uparrow}^{\dagger} a_{1,\downarrow}^{\dagger 2} |vac\rangle$  and  $|\Psi(0)\rangle_{\text{III}} = a_{0,\uparrow}^{\dagger 2} a_{1,\downarrow}^{\dagger 2} |vac\rangle$ , respectively.

For our studies we consider three different initial states where one or two particles from different components are located at the two NN sites at the center of the lattice. The states are -

1. two  $\uparrow$  particles and one  $\downarrow$  particle i.e.  $|\Psi(0)\rangle_{\text{I}} = a_{0,\uparrow}^{\dagger 2} a_{1,\downarrow}^{\dagger} |vac\rangle$ ,
2. one  $\uparrow$  particles and two  $\downarrow$  particles i.e.  $|\Psi(0)\rangle_{\text{II}} = a_{0,\uparrow}^{\dagger} a_{1,\downarrow}^{\dagger 2} |vac\rangle$  and
3. two  $\uparrow$  and two  $\downarrow$  particles i.e.  $|\Psi(0)\rangle_{\text{III}} = a_{0,\uparrow}^{\dagger 2} a_{1,\downarrow}^{\dagger 2} |vac\rangle$

as depicted in Fig. 4.1(a), (b) and (c) respectively. In the following we discuss the QWs for all the cases in details.

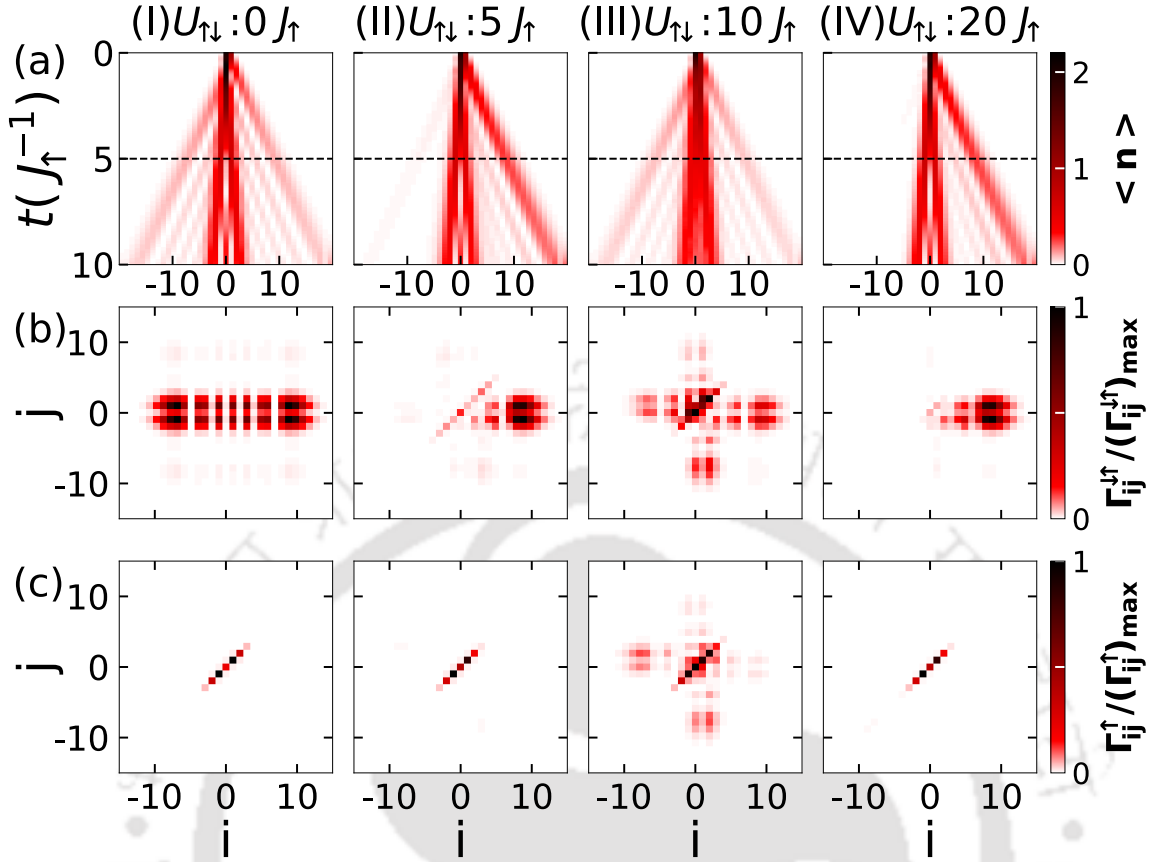


**Figure 4.2:** Panel (a) shows the onsite density evolution with the initial state  $|\Psi(0)\rangle_{\text{I}}$  for (I)  $U_{\uparrow\downarrow} = 0J_{\uparrow}$ , (II)  $U_{\uparrow\downarrow} = 5J_{\uparrow}$ , (III)  $U_{\uparrow\downarrow} = 10J_{\uparrow}$  and (IV)  $U_{\uparrow\downarrow} = 20J_{\uparrow}$ . Panel (b) and (c) show the correlation functions  $\Gamma_{ij}^{\downarrow\uparrow}$  and  $\Gamma_{ij}^{\uparrow\downarrow}$ , respectively. Here  $U = 10J_{\uparrow}$  and  $\delta = 1$  are considered and the correlation functions are plotted at  $t = 5J_{\uparrow}^{-1}$ .

### 4.3 Two $\uparrow$ and one $\downarrow$ particles

In this section, we consider two  $\uparrow$  particles located at the central site (i.e.  $i = 0$ ) of the lattice and a  $\downarrow$  particle at the NN site on the right (i.e.  $i = 1$ ) as shown in Fig. 4.1(a). The initial state corresponding to this situation is  $|\Psi(0)\rangle_{\text{I}}$  which is defined earlier. This choice of the initial state ensures that  $U_{\downarrow}$  is irrelevant in the Hamiltonian of Eq. 4.1. In such a scenario, the competing interactions are  $U_{\uparrow} = U$  and  $U_{\uparrow\downarrow}$ . We first discuss the symmetric hopping case i.e.  $\delta = 1$ . In the absence of  $U_{\uparrow\downarrow}$ , the two components behave independently in their QWs. For large  $U$ , the two  $\uparrow$  particles form a repulsively bound pair [2] and exhibit the QW of a composite particle with reduced hopping strength [3, 27, 96]. This situation is similar to the case of the QWs of two particles with asymmetric hopping as discussed in Ref. [148]. It is expected that with the onset of  $U_{\uparrow\downarrow}$ , the individual wavepackets will start reflecting

from each other leading to complete reflection in the limit of large  $U_{\uparrow\downarrow}$ . In contrast, we show that for a moderate value of  $U = 10J_{\uparrow}$ , which is sufficient to form a bound state of  $\uparrow$  particles, the QW exhibits a re-entrant transition as a function of  $U_{\uparrow\downarrow}$  as can be seen from Fig. 4.2(a)(I-IV). When  $U_{\uparrow\downarrow} = 0J_{\uparrow}$ , the QW shows a slow and fast spreading of densities indicative of that of  $\uparrow\uparrow$  pair and  $\downarrow$  particle, respectively, which can be seen from the finite diagonal elements of the correlation matrix  $\Gamma_{ij}^{\uparrow}$  as shown in Fig. 4.2(c-I). An increase in  $U_{\uparrow\downarrow}$  leads to an onset of a fast spreading wavepacket reflected from the slower one (Fig. 4.2(a-II) for  $U_{\uparrow\downarrow} = 5J_{\uparrow}$ ) a feature which reappears when  $U_{\uparrow\downarrow} > U$  (Fig. 4.2(a-IV) for  $U_{\uparrow\downarrow} = 20J_{\uparrow}$ ). This reflection of wavepacket is due to the inter-particle repulsion and can be understood from the vanishing of the upper triangular matrix elements of  $\Gamma_{ij}^{\downarrow\uparrow}$  as shown in Fig. 4.2(b-II) and Fig. 4.2(b-IV) plotted for  $U_{\uparrow\downarrow} = 5J_{\uparrow}$  and  $20J_{\uparrow}$  respectively. Careful analysis of the correlation function, however, reveals that while in the limit  $U_{\uparrow\downarrow} < U$  and  $U_{\uparrow\downarrow} > U$ , the  $\uparrow\uparrow$  pair survives (see Fig. 4.2(c-II)) and Fig. 4.2(c-IV), at  $U_{\uparrow\downarrow} \sim U$  it tends to break and a two-component pair (which we call a doublon i.e.  $\uparrow\downarrow$ ) tends to form - a scenario completely different from  $U_{\uparrow\downarrow} = 0J_{\uparrow}$  limit (see Fig. 4.2). This feature can be clearly seen from the gradual fading away of the diagonal elements of the intra-component correlation matrix  $\Gamma_{ij}^{\uparrow}$  (Fig. 4.2(c-III)) and appearance of finite diagonal elements of inter-component density correlation matrix  $\Gamma_{ij}^{\downarrow\uparrow}$  (Fig. 4.2(b-III)).

Now we reduce the hopping strength and plot the evolution of the onsite density ( $\langle n_i(t) \rangle$ ), the density-density correlation ( $\Gamma_{ij}^{\downarrow\uparrow}$ ) and the two-particle correlation ( $\Gamma_{ij}^{\uparrow}$ ) in Fig. 4.3 for  $\delta = 0.2$ . When  $U_{\uparrow\downarrow} = 0J_{\uparrow}$ , the QW shows a slow and fast spreading of densities (Fig. 4.3(a-I)) corresponding to the  $\uparrow\uparrow$  pair and  $\downarrow$  particle respectively which can be seen from the finite diagonal elements of the correlation matrix  $\Gamma_{ij}^{\uparrow}$  as shown in Fig. 4.3(c-I). Increasing the value of  $U_{\uparrow\downarrow}$ , the fast spreading wavepacket gets reflected from the slower one (Fig. 4.3(a-II) for  $U_{\uparrow\downarrow} = 5J_{\uparrow}$ ), a feature which reappears when  $U_{\uparrow\downarrow} > U$  (Fig. 4.3(a-IV) for  $U_{\uparrow\downarrow} = 20J_{\uparrow}$ ) indicating the re-entrant feature in the QW. The reflection of wavepacket in this case is due to the inter-particle repulsion and can be understood from vanishing of the upper triangular matrix elements of  $\Gamma_{ij}^{\downarrow\uparrow}$  as depicted in Fig. 4.3(b-II) and Fig. 4.3(b-IV) for  $U_{\uparrow\downarrow} = 5J_{\uparrow}$  and  $20J_{\uparrow}$  respectively. In the limit  $U_{\uparrow\downarrow} < U$  and  $U_{\uparrow\downarrow} > U$ , the  $\uparrow\uparrow$  pair survives (Fig. 4.3(c-I), (c-II) and (c-IV)). Interestingly, when  $U_{\uparrow\downarrow} = U = 10J_{\uparrow}$ ,  $\uparrow\uparrow$  pair breaks completely and a stable two-component pair ( $\uparrow\downarrow$ ) (doublon) is formed after a short time evolutions (Fig. 4.3(III)). This feature can be clearly seen from the vanishing diagonal elements of the intra-component correlation matrix  $\Gamma_{ij}^{\uparrow}$  (Fig. 4.3(c-III)) and appearance of finite diagonal elements of inter-component density correlation

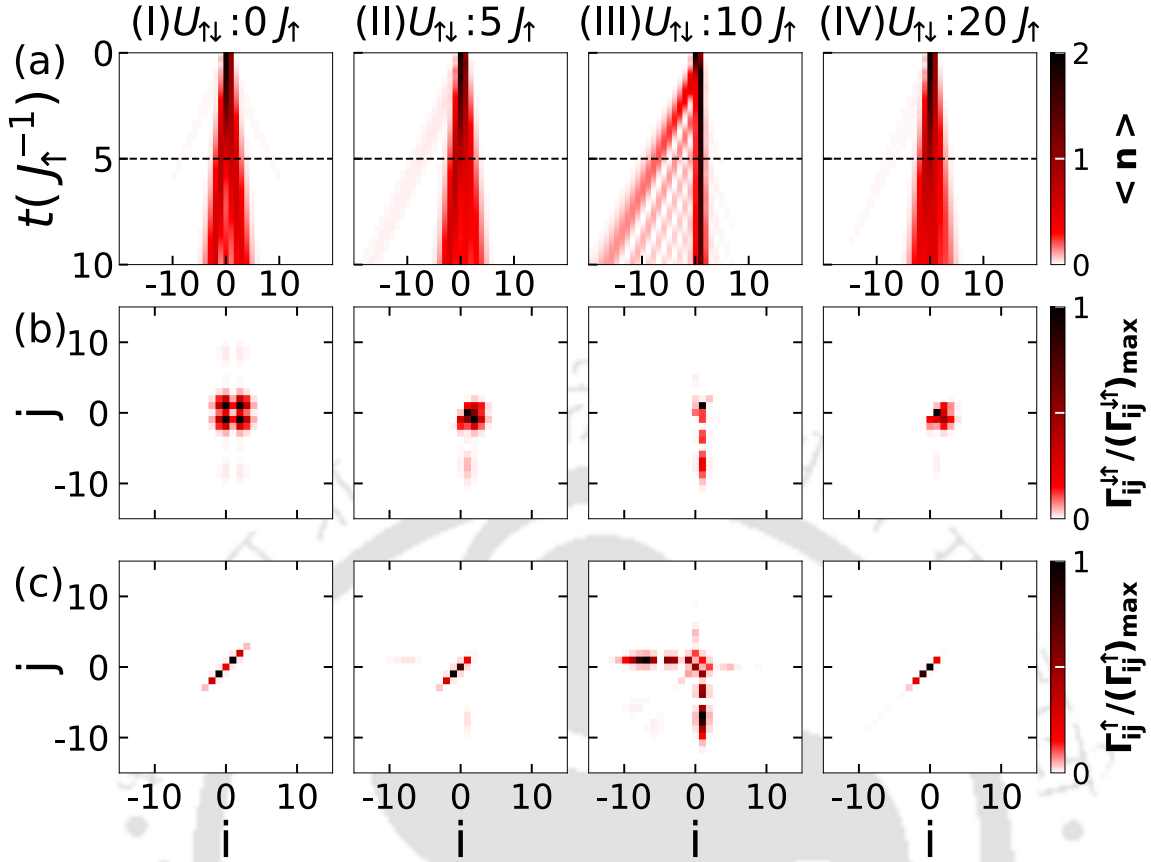


**Figure 4.3:** Panel (a) shows the normalised density evolution of the initial state  $|\Psi_0\rangle = a_{0,\uparrow}^{\dagger 2} a_{1,\downarrow}^{\dagger} |vac\rangle$  for  $U_{\uparrow\downarrow} = 0J_{\uparrow}, 5J_{\uparrow}, 10J_{\uparrow}$  and  $20J_{\uparrow}$ . Here  $U = 10J_{\uparrow}$  and  $\delta = 0.2$ . Panel (b) and (c) show the correlation functions  $\Gamma_{ij}^{\downarrow\uparrow}$  and  $\Gamma_{ij}^{\uparrow\uparrow}$ , respectively at time,  $t = 5J_{\uparrow}^{-1}$ .

matrix  $\Gamma_{ij}^{\downarrow\uparrow}$  (Fig. 4.3(b-III)). For clarity we also show the density evolutions of  $\uparrow$  and  $\downarrow$  components in Fig. 4.4 for  $\delta = 0.2$ . It can be seen that for  $U_{\uparrow\downarrow} = 10J_{\uparrow}$ , the  $\uparrow\uparrow$  pair break into two different profiles. One of them remain close to the center which forms a doublon with the  $\downarrow$  component and at site "1" and the other moves independently to the left since this doublon acts as a potential barrier that reflects the wavepacket of the isolated  $\uparrow$  component (Fig. 4.4(a(III))).

In order to quantify the doublon formation and the dissociation of  $\uparrow\uparrow$  pair, we compute the quantities defined as

$$P_{\uparrow\downarrow} = \sum_i n_{i,\uparrow} n_{i,\downarrow}; \quad P_{\uparrow\uparrow} = 1/2 \sum_i (n_{i,\uparrow}^2 - n_{i,\uparrow}), \quad (4.3)$$

which count the number of  $\uparrow\downarrow$  and  $\uparrow\uparrow$  pairs in the system and can be computed from the correlation matrix. In Fig. 4.5(a), we plot both  $P_{\uparrow\downarrow}$  (circles) and  $P_{\uparrow\uparrow}$

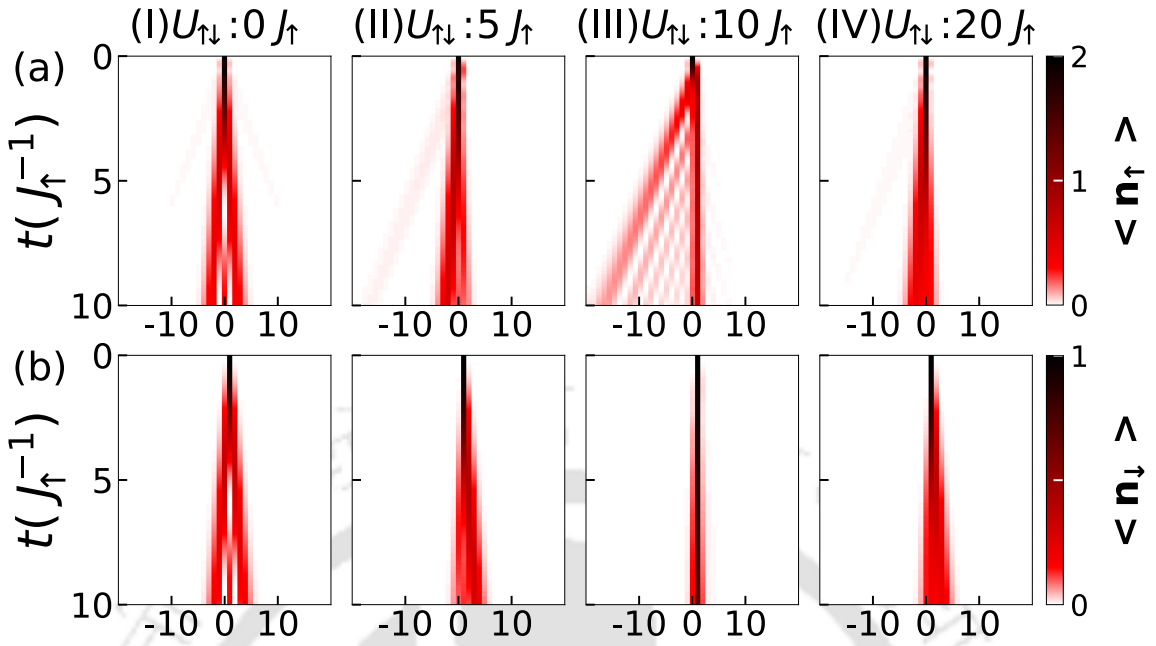


**Figure 4.4:** Panel (a) and (b) show the normalised density evolution of  $n_{\uparrow}$  and  $n_{\downarrow}$ , respectively for  $U_{\uparrow\downarrow} = 0J_{\uparrow}, 5J_{\uparrow}, 10J_{\uparrow}$  and  $20J_{\uparrow}$ . Here  $U = 10J_{\uparrow}$  and  $\delta = 0.2$ .

(squares) as a function of  $U_{\uparrow\downarrow}$  for both  $\delta = 1$  (dashed curve) and  $\delta = 0.2$  (solid curve) while keeping  $U = 10J_{\uparrow}$ , after a time evolution to  $t = 10J_{\uparrow}^{-1}$ . Clearly, the doublon formation is indicated by a dominant value of  $P_{\uparrow\downarrow}$  at  $U_{\uparrow\downarrow} = U = 10J_{\uparrow}$  for  $\delta = 0.2$ . Note that for  $\delta = 1$ , both  $P_{\uparrow\downarrow}$  and  $P_{\uparrow\uparrow}$  are of the same order due to the equal probabilities of formation of both the types of bound pairs. We also plot the time evolution of  $P_{\uparrow\downarrow}$  and  $P_{\uparrow\uparrow}$  at the critical value  $U_{\uparrow\downarrow} = U = 10J_{\uparrow}$  in Fig. 4.5(b). The finite (zero) value of  $P_{\uparrow\downarrow}$  ( $P_{\uparrow\uparrow}$ ) after  $t > 1J_{\uparrow}^{-1}$  indicates the formation (dissociation) of  $\uparrow\downarrow$  ( $\uparrow\uparrow$ ) pair. In the inset of Fig. 4.5(b), the variation of  $P_{\uparrow\downarrow}$  for different values of  $\delta$  confirms that the doublon formation is robust for smaller  $\delta$ . So up to this point, we have obtained that when  $U_{\uparrow\downarrow}$  is of the order of  $U$ , the  $\uparrow\uparrow$  pair tends to break, and a  $\uparrow\downarrow$  pair tends to form. A hopping imbalance introduces a complete dissociation of a  $\uparrow\uparrow$  pair, and a doublon is formed.

The reason behind this can be explained as follows. In the limit of equal inter and intra-species interaction and equal hopping strengths of both the components, the binding energy of  $\uparrow\uparrow$  pair and  $\uparrow\downarrow$  pair are equal. Hence the states  $|(\uparrow\uparrow)_0\rangle, |(\downarrow)_1\rangle$  and  $|(\uparrow)_0\rangle, |(\uparrow\downarrow)_1\rangle$  are degenerate. Therefore, during the QWs, when the wavepacket of the  $\uparrow\uparrow$  pair overlaps with that of the  $\downarrow$  component there is equal probability of forming either of the bound states. Hence, we see the signature of both  $\uparrow\uparrow$  pair and  $\uparrow\downarrow$  pair in the QWs. However, by making the  $J_{\downarrow}$  smaller and comparable to the effective hopping

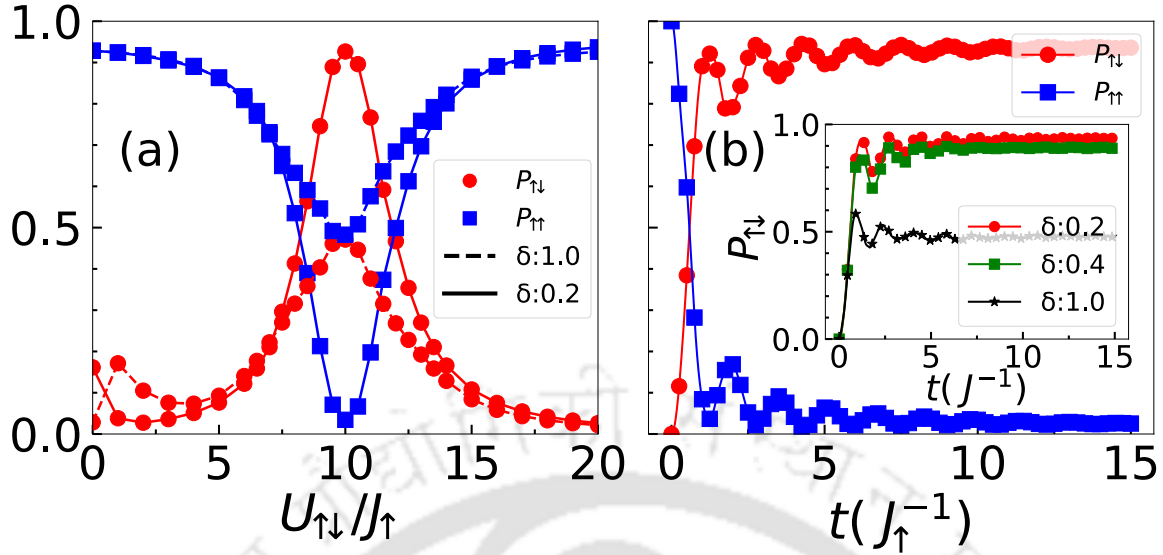


**Figure 4.5:** (a)  $P_{\uparrow\downarrow}$  (red circles) and  $P_{\uparrow\uparrow}$  (blue squares) are plotted against  $U_{\uparrow\downarrow}/J_{\uparrow}$  for  $\delta = 1$  (dashed curve) and  $\delta = 0.2$  (solid curve) at  $t = 10J_{\uparrow}^{-1}$ . (b) Shows the time evolution of  $P_{\uparrow\downarrow}$  (red circles) and  $P_{\uparrow\uparrow}$  (blue squares) for  $\delta = 0.2$  and  $U_{\uparrow\downarrow} = 10J_{\uparrow}$  indicating complete inter-component pair formation and breaking up of  $\uparrow\uparrow$  pair. (Inset) The time evolution of  $P_{\uparrow\downarrow}$  for different  $\delta$  such as  $\delta = 0.2$  (red circles),  $\delta = 0.4$  (green squares) and  $\delta = 1$  (black stars).

strength of  $\uparrow\uparrow$  pair, the doublon formation becomes energetically more favorable. This is because the doublon formation increases the system's overall energy, and the particles avoid each other due to repulsion. Note that this phenomenon is due to the interplay of both intra- and inter-species interactions and hence forbidden in the case of indistinguishable bosons [27] and two-component mixture with one particle from each species as considered in Ref. [148].

#### 4.4 One $\uparrow$ and two $\downarrow$ particles

In this section we study the QW with a different initial state

$$|\Psi(0)\rangle_{\text{II}} = a_{0,\uparrow}^\dagger a_{1,\downarrow}^{\dagger 2} |vac\rangle \quad (4.4)$$

where we consider two  $\downarrow$  particle and one  $\uparrow$  particle as shown in Fig. 4.1(b). Although we have in total three-particles in the system, the situation is completely different from the QW with the initial state  $|\Psi(0)\rangle_{\text{I}}$  when  $\delta \neq 1$ . In Fig. 4.6, we plot the onsite density, the inter- and intra-component correlation function for  $U_{\downarrow} = U = 10J_{\uparrow}$  and  $\delta = 0.2$  for different values of  $U_{\uparrow\downarrow}$ . It can be seen from Fig. 4.6(a) that when  $U_{\uparrow\downarrow} = 0J_{\uparrow}$ , the two  $\downarrow$  particles exhibit slow spreading of densities corresponding

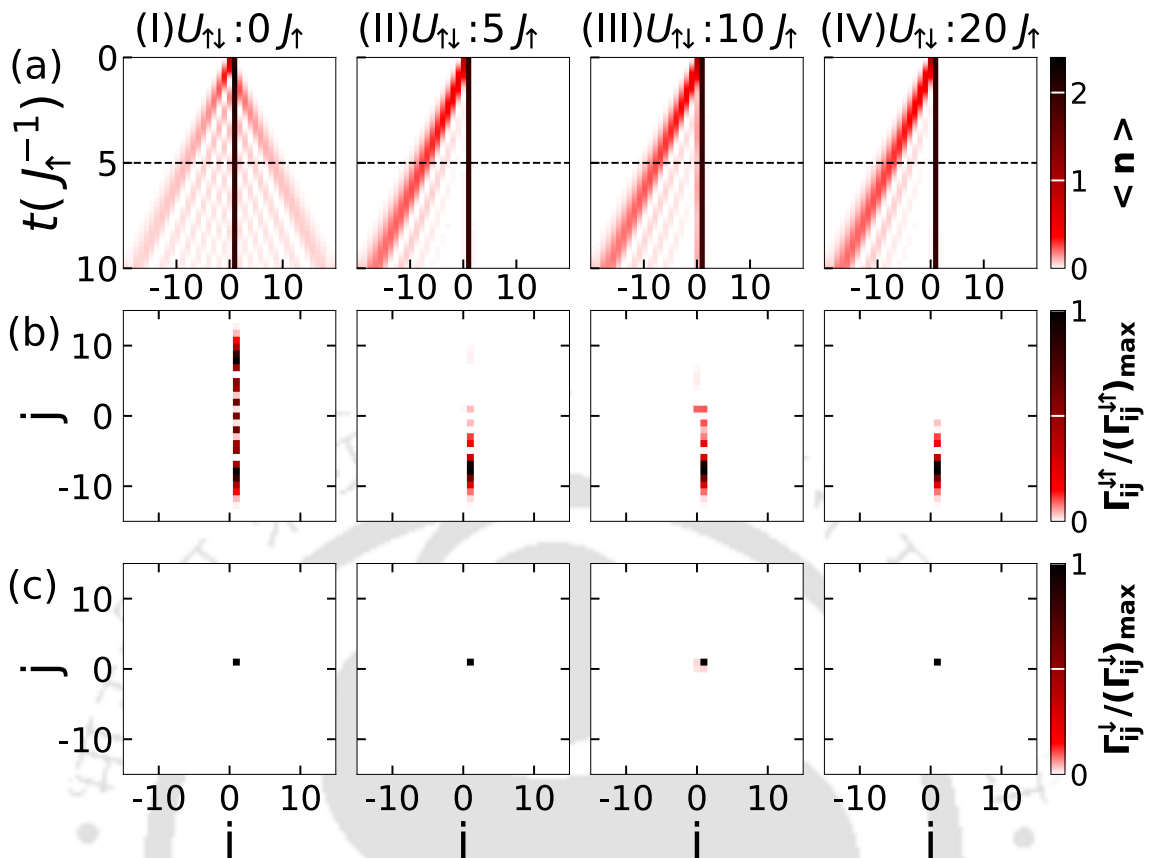


**Figure 4.6:** Panel (a) shows the normalised density evolution of the initial state  $|\Psi_0\rangle_{\text{II}} = a_{0,\uparrow}^\dagger a_{1,\downarrow}^\dagger |vac\rangle$  for  $U_{\uparrow\downarrow} = 0J_{\uparrow}$ ,  $5J_{\uparrow}$ ,  $10J_{\uparrow}$  and  $20J_{\uparrow}$ . Here  $U = 10J_{\uparrow}$  and  $\delta = 0.2$ . In Panel (b) and (c) are shown the correlation functions  $\Gamma_{ij}^{\uparrow\uparrow}$  and  $\Gamma_{ij}^{\downarrow\downarrow}$  respectively at time,  $t = 5J_{\uparrow}^{-1}$ .

to  $\downarrow\downarrow$  pair localized around the 1<sup>st</sup> site and the single  $\uparrow$  particle exhibits a fast propagation. Finite  $U_{\uparrow\downarrow}$  leads to the reflection of the  $\uparrow$  component from the potential barrier created by the  $\downarrow\downarrow$  pair. The signatures of the reflection of wavepacket and the  $\downarrow\downarrow$  pair can be seen from the correlation matrix  $\Gamma_{ij}^{\uparrow\uparrow}$  and  $\Gamma_{ij}^{\downarrow\downarrow}$  plotted in Fig. 4.6(b) and (c) respectively. This phenomenon can also be seen by individually plotting the density evolution of the  $\uparrow$  and  $\downarrow$  components as shown in Fig. 4.7. Note that the formation of a doublon ( $\uparrow\downarrow$  pair) in this case is forbidden due to the strong  $\downarrow\downarrow$  pair.

We also confirm the absence of doublon formation in the limit  $\delta \neq 1$  by comparing the  $P$  values defined in the main text. In Fig. 4.8(a) we plot  $P_{\uparrow\downarrow}$  and  $P_{\downarrow\downarrow}$  for different values of  $U_{\uparrow\downarrow}$  and  $\delta = 0.2$  after a time evolution to  $t = 10J_{\uparrow}^{-1}$ . The values of  $P_{\downarrow\downarrow} \sim 0$  and  $P_{\uparrow\downarrow} \sim 1$  as a function of  $U_{\uparrow\downarrow}$  indicate no doublon formation. This behaviour can be complemented by the time evolution of  $P_{\downarrow\downarrow}$  and  $P_{\uparrow\downarrow}$  which saturate to 1 and 0 respectively (Fig. 4.8(b)). In the inset of Fig. 4.8(b) we show the time evolution

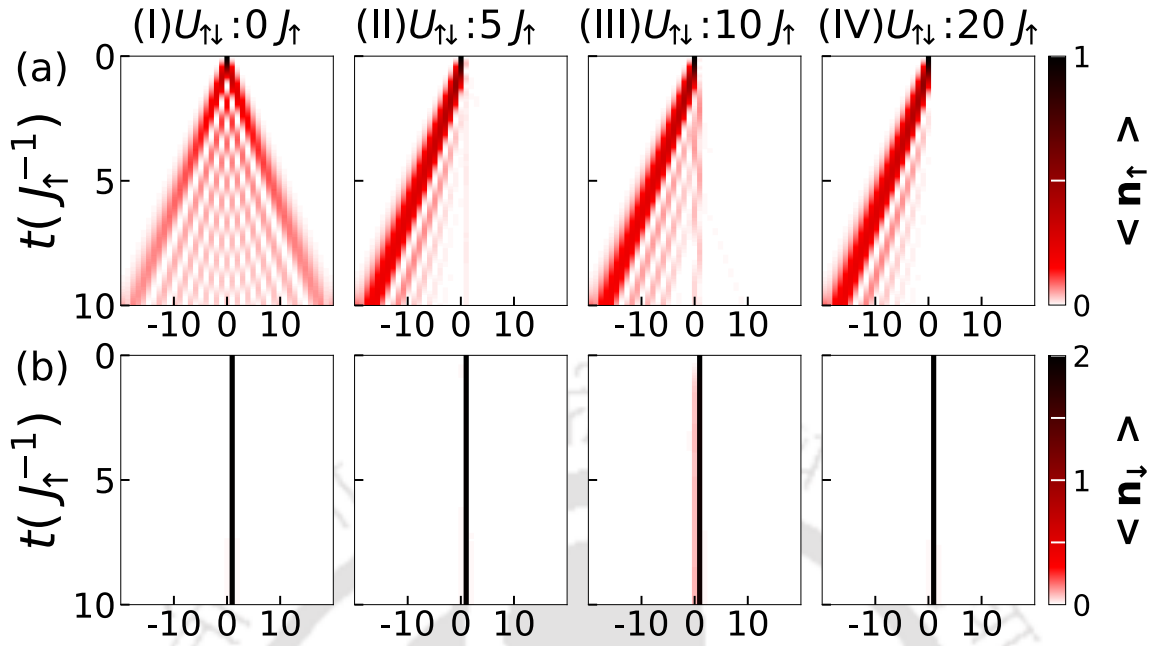


**Figure 4.7:** Panel (a) and (b) show the normalised density evolution of  $n_{\uparrow}$  and  $n_{\downarrow}$ , respectively for  $U_{\uparrow\downarrow} = 0, 5, 10$  and  $20$ . Here  $U = 10$  and  $\delta = 0.2$ .

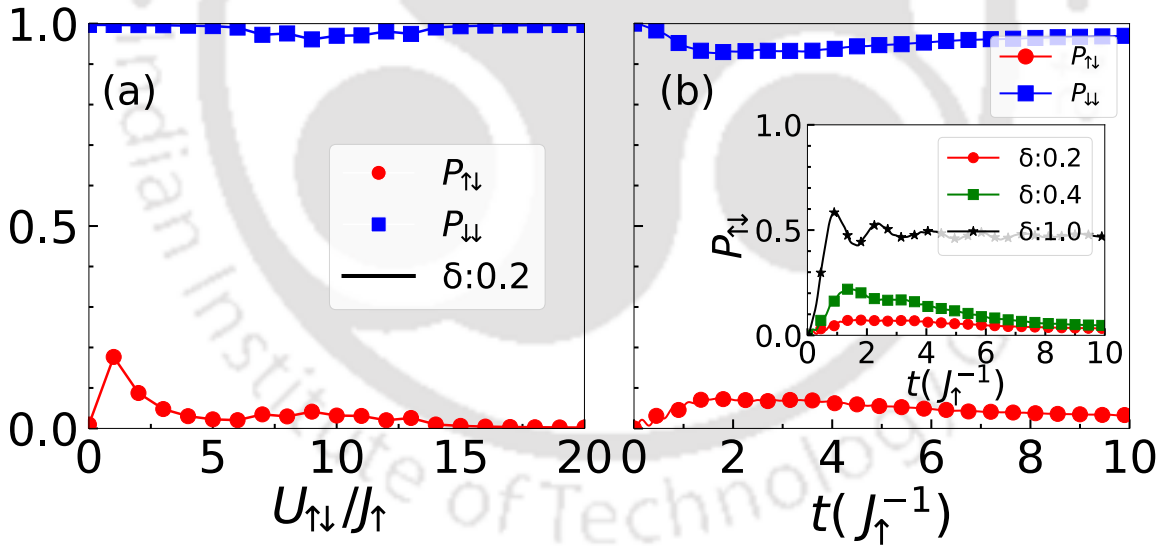


**Figure 4.8:** (a)  $P_{\uparrow\downarrow}$  (circles) and  $P_{\downarrow\downarrow}$  (squares) against  $U_{\uparrow\downarrow}/J_{\uparrow}$  for  $\delta = 1$  (dashed curve) and  $\delta = 0.2$  (solid curve) at  $t = 10J_{\uparrow}^{-1}$ . (b) Shows the time evolution of  $P_{\uparrow\downarrow}$  (circles) and  $P_{\downarrow\downarrow}$  (squares) for different  $\delta = 0.2$  and  $U_{\uparrow\downarrow} = 10J_{\uparrow}$  indicating that there are no inter-component pair formation and dissociation of  $\downarrow\downarrow$  pair. (Inset) The time evolution of  $P_{\uparrow\downarrow}$  for different  $\delta$  such as  $\delta = 0.2$  (circle),  $\delta = 0.4$  (square) and  $\delta = 1$  (star).

of  $P_{\uparrow\downarrow}$  which saturates to a finite value for  $\delta = 1$  and vanishes as  $\delta$  decreases. This indicates a behaviour opposite to that with the initial state  $|\Psi(0)\rangle_t$  discussed in

Sec. 4.4.

## 4.5 Two $\uparrow$ and two $\downarrow$ particles

In this section we consider two particles from each component as shown in Fig. 4.1(c) and study their QWs. The initial state considered for this case is given by

$$|\Psi_0\rangle_{\text{III}} \equiv a_{0,\uparrow}^{\dagger 2} a_{1,\downarrow}^{\dagger 2} |vac\rangle \quad (4.5)$$

Note that for this initial state the  $U_{\downarrow}$  term in the Hamiltonian of Eq. 4.1 is relevant which was ignored previously. Now, the physics of the system will be governed by all the three interactions, namely  $U_{\uparrow}$ ,  $U_{\downarrow}$  and  $U_{\uparrow\downarrow}$ . Similar to the previous cases, here we assume  $U_{\uparrow} = U_{\downarrow} = U = 10J_{\uparrow}$  and vary  $U_{\uparrow\downarrow}$  for our investigation. We begin the discussion with asymmetric hopping and come back to the symmetric case later. In the limit of  $U = 10J_{\uparrow}$ , both  $\uparrow$  and  $\downarrow$  particles form repulsively bound pairs at the beginning when  $U_{\uparrow\downarrow} = 0J_{\uparrow}$  [2, 3, 27, 94, 96].

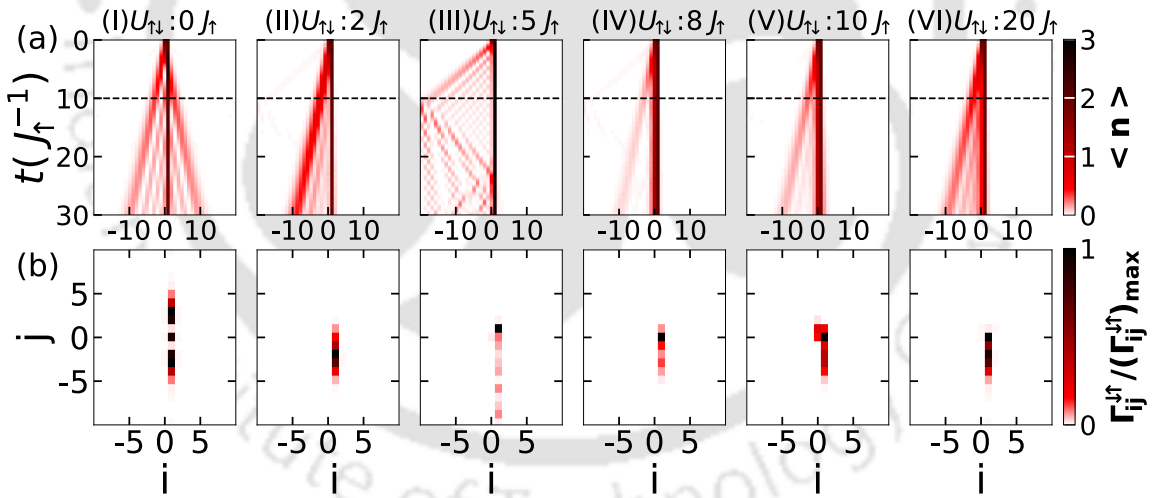


**Figure 4.9:** Panel (a) shows the density evolution of the initial state  $|\Psi_0\rangle = a_{0,\uparrow}^{\dagger 2} a_{1,\downarrow}^{\dagger 2} |vac\rangle$  for  $U_{\uparrow\downarrow} = 0J_{\uparrow}, 2J_{\uparrow}, 5J_{\uparrow}, 8J_{\uparrow}, 10J_{\uparrow}$  and  $20J_{\uparrow}$ . Here  $U = 10J_{\uparrow}$  and  $\delta = 0.2$ . Panel (b) shows the correlation functions  $\Gamma_{ij}^{\downarrow\uparrow}$  at time,  $t = 10J_{\uparrow}^{-1}$ .

We plot the density evolution ( $\langle n_i(t) \rangle$ ), the density-density correlation function ( $\Gamma_{ij}^{\downarrow\uparrow}$ ) for  $U = 10J_{\uparrow}$  and  $U_{\uparrow\downarrow} = 0J_{\uparrow}, 2J_{\uparrow}, 5J_{\uparrow}, 8J_{\uparrow}, 10J_{\uparrow}, 20J_{\uparrow}$  in Fig. 4.9 and Fig. 4.11 for  $\delta = 0.2$  and  $\delta = 1.0$  respectively. For  $U_{\uparrow\downarrow} = 0J_{\uparrow}$  and  $\delta = 0.2$ , the two  $\uparrow\uparrow$  and  $\downarrow\downarrow$  pairs perform QWs independently with fast and slow spreading respectively because of the difference in their effective tunneling rates. As  $U_{\uparrow\downarrow}$  increases, the

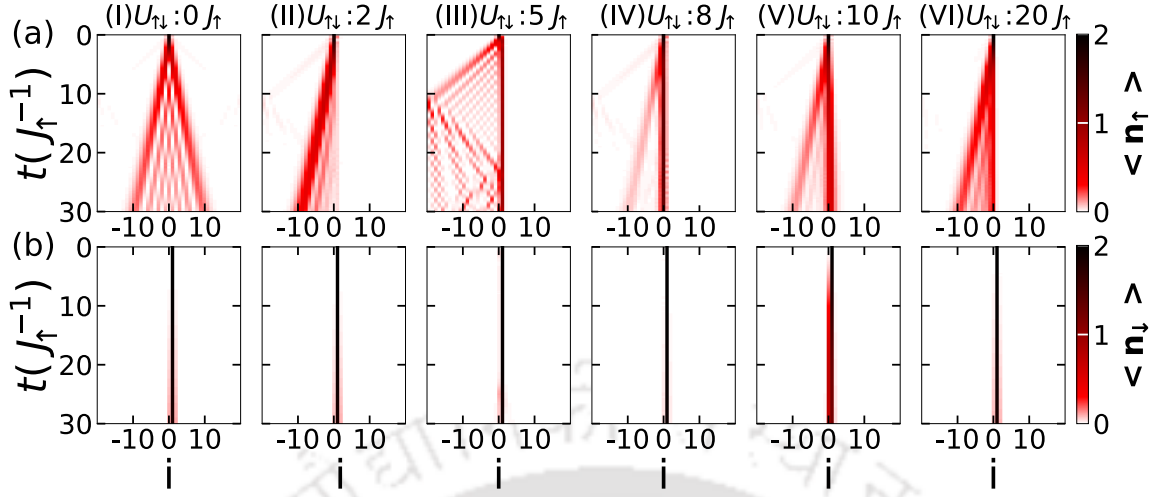


**Figure 4.10:** Panel (a) and (b) show the density evolution of  $n_{\uparrow}$  and  $n_{\downarrow}$ , respectively for  $U_{\uparrow\downarrow} = 0J_{\uparrow}, 2J_{\uparrow}, 5J_{\uparrow}, 8J_{\uparrow}, 10J_{\uparrow}$  and  $20J_{\uparrow}$ . Here  $U = 10J_{\uparrow}$  and  $\delta = 0.2$ .

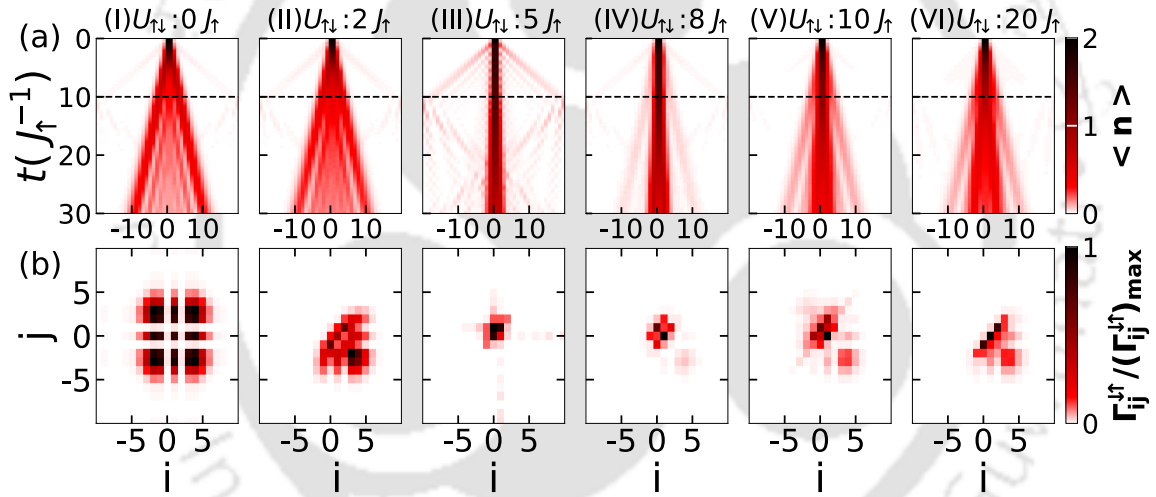


**Figure 4.11:** Panel (a) shows the density evolution of the initial state  $|\Psi_0\rangle = a_{0,\uparrow}^{\dagger 2} a_{1,\downarrow}^{\dagger 2} |vac\rangle$  for  $U_{\uparrow\downarrow} = 0J_{\uparrow}, 2J_{\uparrow}, 5J_{\uparrow}, 8J_{\uparrow}, 10J_{\uparrow}$  and  $20J_{\uparrow}$ . Here  $U = 10J_{\uparrow}$  and  $\delta = 1.0$ . Panel (b) shows the correlation functions  $\Gamma_{ij}^{\uparrow\downarrow}$  at time,  $t = 10J_{\uparrow}^{-1}$ .

fast moving wavepacket starts to get reflected from the slower one (Fig. 4.9(a-II) for  $U_{\uparrow\downarrow} = 2J_{\uparrow}$ ) which reappears in the limit when  $U_{\uparrow\downarrow} > U$  (Fig. 4.9(a-VI) for  $U_{\uparrow\downarrow} = 20J_{\uparrow}$ ). This reflection of wavepacket can be easily understood from the vanishing of the upper triangular matrix elements of  $\Gamma_{ij}^{\uparrow\downarrow}$  as shown in Fig. 4.9(b-II) and Fig. 4.9(b-VI). We also plot individual density evolution  $n_{\uparrow}$  and  $n_{\downarrow}$  in Fig. 4.10 to observe the features i.e., reflection of the  $\uparrow$  particle wavepacket, breaking of the  $\uparrow\uparrow$  pair at 0 site and formation of pair at 1<sup>st</sup> site. Similar features are also visible in the symmetric hopping case i.e.  $\delta = 1.0$  (see Fig. 4.11 (b-II) and (b-VI)). This

indicates that the re-entrant feature in the QW of  $\uparrow\uparrow$  and  $\downarrow\downarrow$  pair appears in the limit of  $U_{\downarrow} < 5J_{\uparrow}$  and  $U_{\downarrow} > 10J_{\uparrow}$ . In Fig. 4.9, when  $U_{\downarrow} = 5J_{\uparrow}$ , we see simultaneous

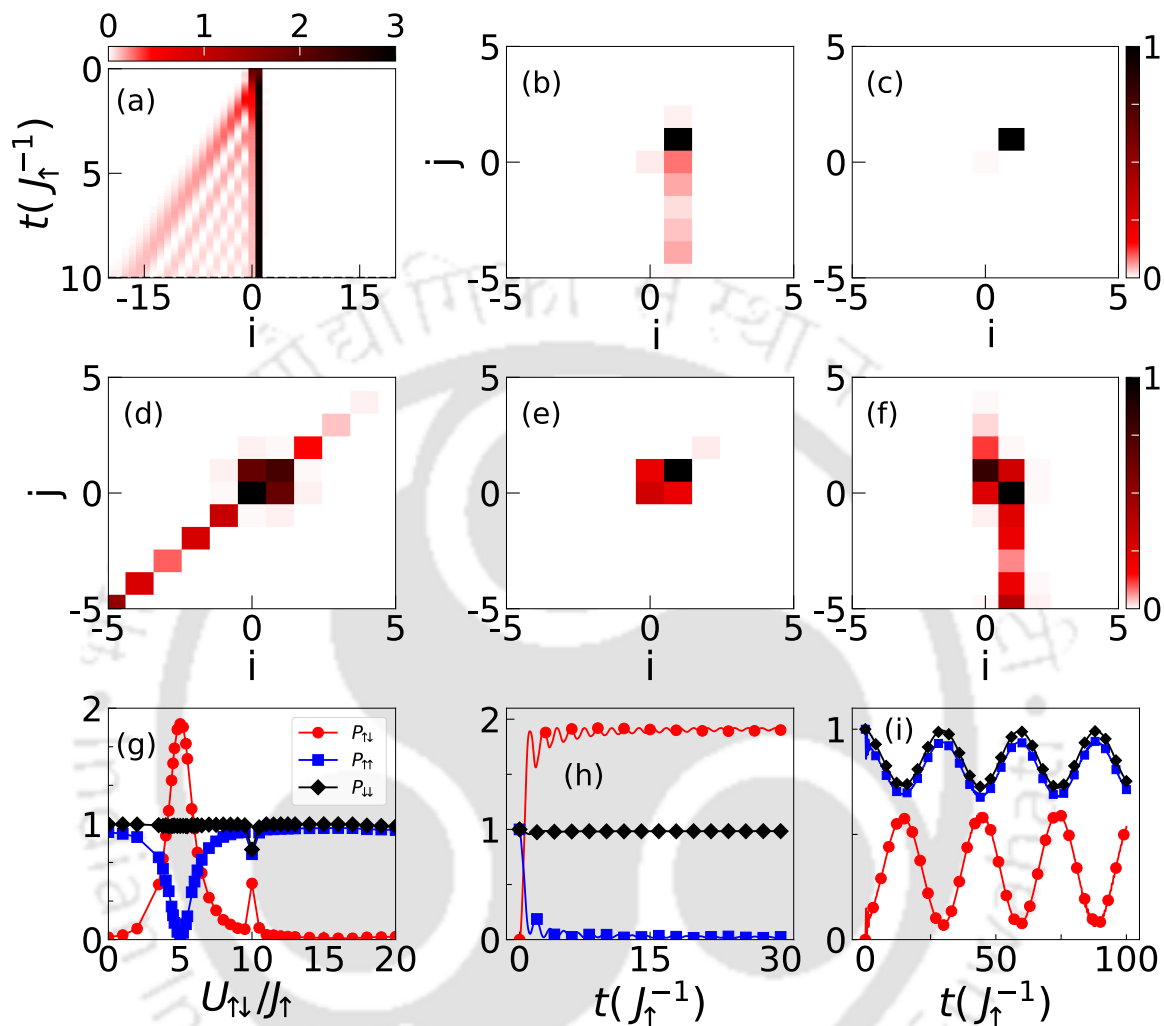


**Figure 4.12:** Figure shows (a)  $\langle n_i \rangle$ , (b)  $\Gamma_{ij}^{\downarrow\uparrow}$  and (c)  $\Gamma_{ij}^{\downarrow}$  for the QWs with the initial state  $|\Psi(0)\rangle_{\text{II}}$  for  $U_{\downarrow} = 5J_{\uparrow}$ ,  $U = 10J_{\uparrow}$  and  $\delta = 0.2$  at  $t = 10J_{\uparrow}^{-1}$ . (d-f) Show the values of  $\Gamma_{ij}^{\uparrow}$ ,  $\Gamma_{ij}^{\downarrow}$  and  $\Gamma_{ij}^{\uparrow\downarrow}$ , respectively for  $U_{\downarrow} = 10J_{\uparrow}$  at  $t = 17J_{\uparrow}^{-1}$ . (g) Shows the behavior of  $P_{\uparrow\downarrow}$  (red circles),  $P_{\uparrow\uparrow}$  (blue squares) and  $P_{\downarrow\downarrow}$  (black diamond) as a function of  $U_{\downarrow}$  at  $t = 10J_{\uparrow}^{-1}$ . The time evolution of  $P$ 's are plotted in (h) and (i) for  $U_{\downarrow} = 5J_{\uparrow}$  and  $10J_{\uparrow}$ , respectively with  $L = 82$  sites.

signatures of a three-particle and a single-particle QW in the density evolution and take a closer view of this density evolution and plot it in Fig. 4.12(a). The figure indicates that a  $\uparrow$  particle forms pair with an already formed  $\downarrow\downarrow$  pair leaving behind an isolated  $\uparrow$  particle indicated by the central bright patch. These features can be seen in the correlation data shown in Fig. 4.12 (b) and (c) where  $\Gamma_{ij}^{\downarrow\uparrow}$  and  $\Gamma_{ij}^{\downarrow}$  are plotted respectively. The bright spots at (1,1) position in Fig. 4.12 (b) and (c)

indicate the three-particle bound state. To further quantify this we compare the behaviour of  $P_{\downarrow\downarrow} = 1/2 \sum_i (n_{i,\downarrow}^2 - n_{i,\downarrow})$  along with  $P_{\uparrow\uparrow}$  and  $P_{\uparrow\downarrow}$  as a function of  $U_{\uparrow\downarrow}$  in Fig. 4.12(g). The values of  $P_{\uparrow\uparrow} \sim 0$  (blue square),  $P_{\downarrow\downarrow} \sim 1$  (black diamond) and  $P_{\uparrow\downarrow} \sim 2$  (red circle) for  $U_{\uparrow\downarrow} = 5J_{\uparrow}$  after the time evolution to  $t = 10J_{\uparrow}^{-1}$  confirm the formation of  $\uparrow\downarrow\downarrow$  bound state, which we call a triplon. The triplon formation can also be confirmed from the time evolved values of  $P$ 's which saturate to  $P_{\uparrow\downarrow} \sim 2$ ,  $P_{\downarrow\downarrow} \sim 1$  and  $P_{\uparrow\uparrow} \sim 0$  as shown in Fig. 4.12(h). On the other hand the isolated  $\uparrow$  particle can not penetrate the potential barrier created by the triplon and performs a unidirectional QW on the left part of the lattice as can be seen from Fig. 4.12(a). The triplon formation at  $U_{\uparrow\downarrow} = U/2 = 5J_{\uparrow}$  can also be attributed to the condition of minimum effective interaction which can be understood as follows. In the atomic limit, the states  $|(\uparrow\uparrow)_0 (\downarrow\downarrow)_1\rangle$ ,  $|(\uparrow)_0 (\uparrow\downarrow\downarrow)_1\rangle$  and  $|(\uparrow\uparrow\downarrow)_0 (\downarrow)_1\rangle$  are degenerate. With  $\delta = 0.2$ , the  $\uparrow\uparrow$  pair is weakly bound compared to the  $\downarrow\downarrow$  pair because  $U/J_{\uparrow} < U/J_{\downarrow}$ . This ensures faster spreading of the former compared to the latter. Hence, during the time evolution, when the wavepacket of the  $\uparrow\uparrow$  pair overlaps with that of the  $\downarrow\downarrow$  pair and due to degeneracy, a stable triplon is formed. To find the difference between

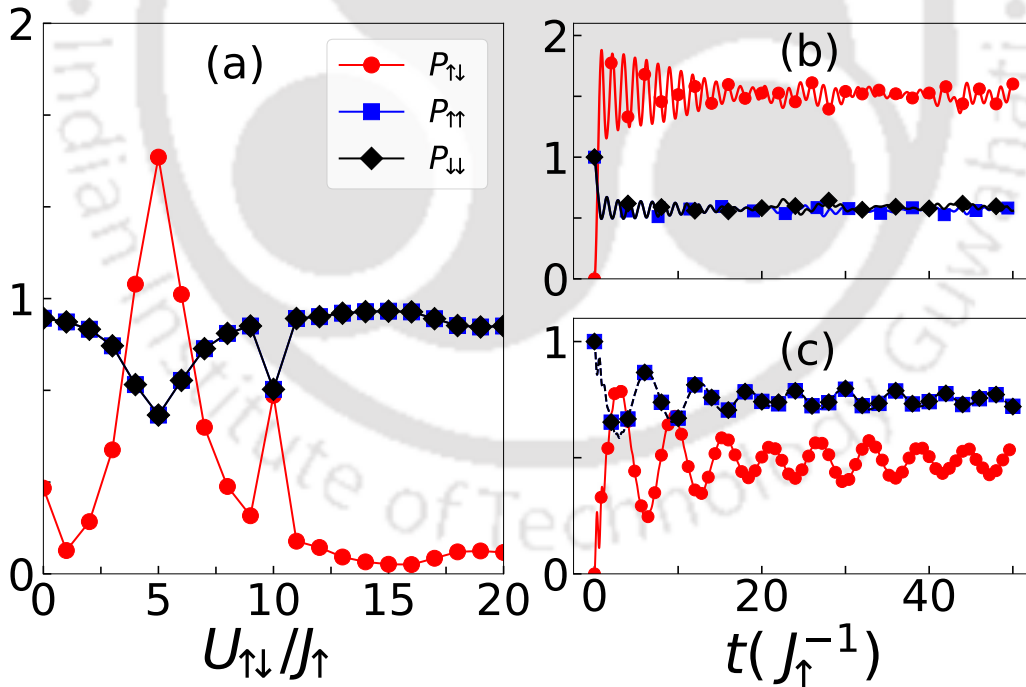


**Figure 4.13:** (a)  $P_{\uparrow\downarrow}$  (red circles),  $P_{\uparrow\uparrow}$  (blue squares) and  $P_{\downarrow\downarrow}$  (black diamonds) against  $U_{\uparrow\downarrow}$  for  $\delta = 1$  at  $t = 10J_{\uparrow}^{-1}$ . (b) Shows the time evolution of  $P_{\uparrow\downarrow}$  (red circles),  $P_{\uparrow\uparrow}$  (blue squares) and  $P_{\downarrow\downarrow}$  (black diamonds) for  $U_{\uparrow\downarrow} = 5J_{\uparrow}$  indicating the formation of inter-component pair and dissociation of  $\downarrow\downarrow$  pair. (c) The time evolution of  $P_{\uparrow\downarrow}$  (red circles),  $P_{\uparrow\uparrow}$  (blue squares) and  $P_{\downarrow\downarrow}$  (black diamonds) for  $U_{\uparrow\downarrow} = 10J_{\uparrow}$ .

symmetric and asymmetric hopping cases, we also plot the  $P$ 's at time  $t = 10J_{\uparrow}^{-1}$  in Fig. 4.13(a) for the  $\delta = 1$ . This indicates a similar behaviour compared to  $\delta = 0.2$  except at  $U_{\uparrow\downarrow} \sim 5J_{\uparrow}$ . At  $U_{\uparrow\downarrow} = 5J_{\uparrow}$ , the values of  $P_{\uparrow\downarrow} < 2$  and  $P_{\uparrow} = P_{\downarrow} < 1$  indicate the partial formation (dissociation) of the triplon (pairs). Moreover, we plot the variation of  $P$ 's with time  $t(J_{\uparrow}^{-1})$  in Fig. 4.13(b) which confirms the formation (dissociation) of triplon (pairs) with time. Further increase in  $U_{\uparrow\downarrow}$  tends to favour the

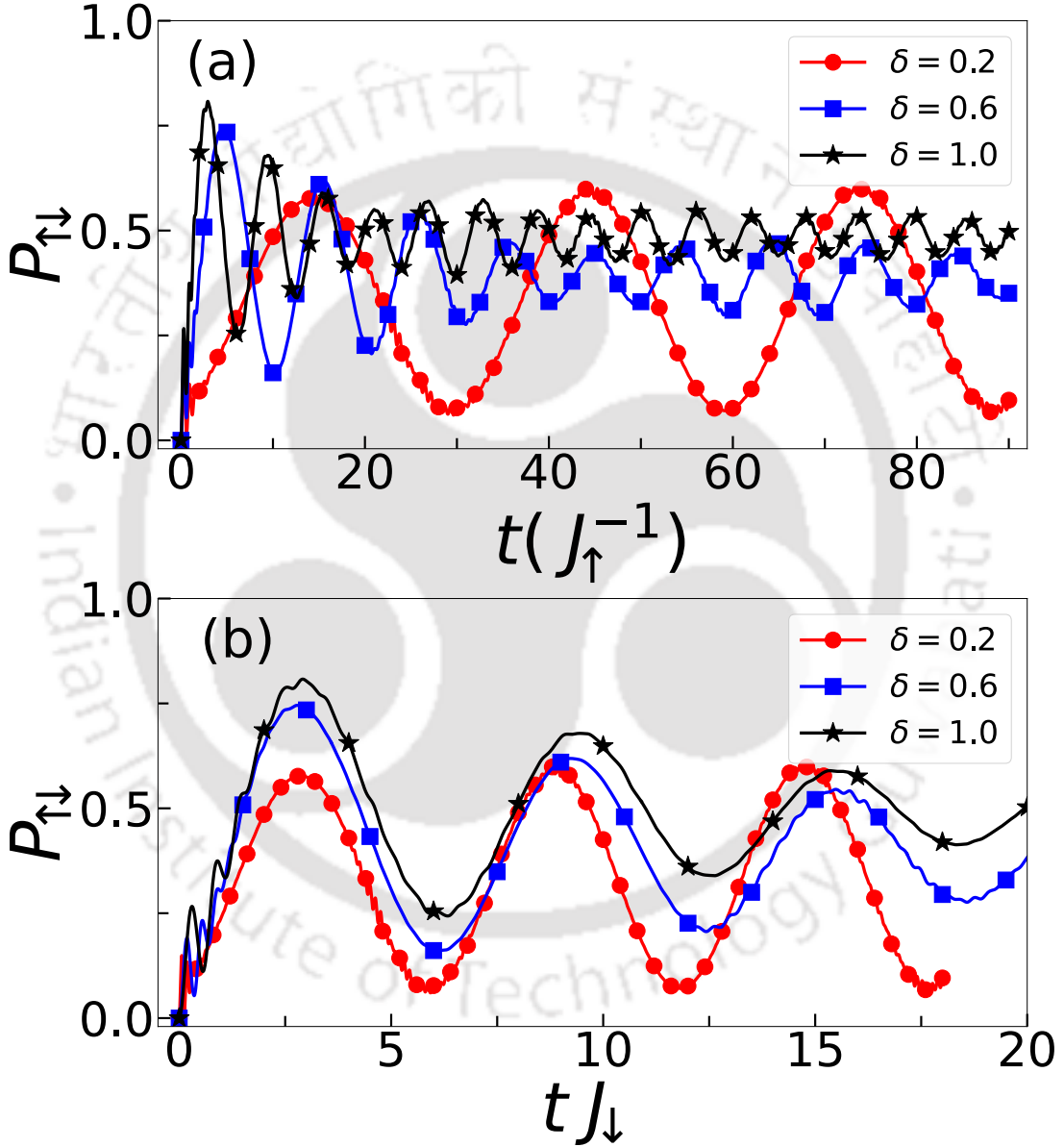


**Figure 4.14:** Figure shows  $P_{\uparrow\downarrow}$  as a function of  $t(J_{\uparrow}^{-1})$  (a), and  $tJ_{\downarrow}$  (b) for different  $\delta$  with  $U_{\uparrow\downarrow} = U_{\uparrow} = U_{\downarrow} = 10J_{\uparrow}$ .

formation of all possible pairs such as the doublon ( $\uparrow\downarrow$ ) and two intra-component pairs ( $\uparrow\uparrow$  and  $\downarrow\downarrow$ ) at  $U_{\uparrow\downarrow} = U = 10J_{\uparrow}$ . The signatures of which can be seen as

the finite diagonal elements of the correlation matrices (Fig. 4.12 (d-f)) and the behaviour of the values of  $P$ 's (Fig. 4.12 (g and i)) for  $\delta = 0.2$ , are also same for  $\delta = 1.0$  as shown in Fig. 4.13 (a and c). It is to be noted that the  $P$ 's exhibit finite oscillation in their time evolution for different values of  $\delta$ . In Fig. 4.14(a) we show the variation of  $P_{\uparrow\downarrow}$  with time for  $\delta = 0.2, 0.6$  and  $1$ . It can be seen that the period of oscillation increases with decreasing  $\delta$ . This phenomenon can be explained in the following way. When the two components form doublons, they move with an effective second-order hopping  $\propto J_{\uparrow}J_{\downarrow}/U_{\uparrow\downarrow}$  as suggested by the perturbation theory [152, 153]. This leads to the different time scales for different  $\delta$ , which is  $\propto 1/J_{\downarrow}$  (as other parameters are the same for different  $\delta$  cases) in the QW. As a result, we see different periods of oscillation in  $P$ 's with respect to time, as shown in Fig. 4.14(a). To confirm this we plot  $P_{\uparrow\downarrow}$  with  $tJ_{\downarrow}$  in Fig. 4.14(b), which shows almost equal period of oscillation for different values of  $\delta$ . The slight deviation in the long time evolution for different  $\delta$  can be attributed to the approximation in the perturbation theory. Interestingly, we also see the signature of a nearest-neighbour

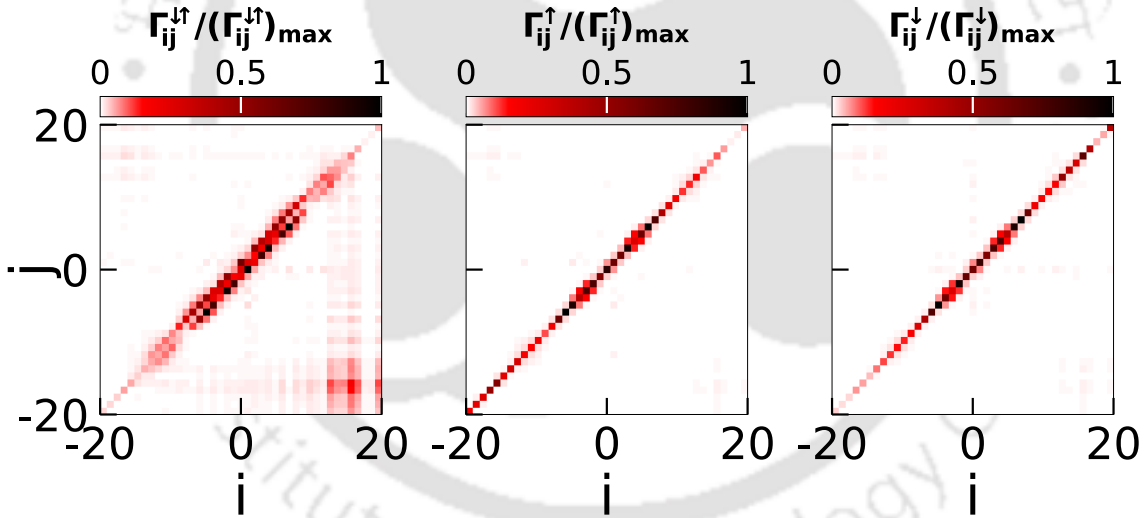


**Figure 4.15:**  $\Gamma_{ij}^{\downarrow\uparrow}$ ,  $\Gamma_{ij}^{\uparrow\uparrow}$  and  $\Gamma_{ij}^{\downarrow\downarrow}$  are plotted at time  $t = 70J_{\uparrow}^{-1}$  for  $U_{\uparrow\downarrow} = U = 10J_{\uparrow}$  and  $\delta = 1$ .

$\uparrow\downarrow$  pair in the density-density correlation matrix in Fig. 4.12(f) for  $\delta = 0.2$ . This unusual pairing is inevitable due to the simultaneous formation of onsite pairs and doublons. To confirm this we plot  $\Gamma_{ij}^{\downarrow\uparrow}$  at time  $t = 70J_{\uparrow}^{-1}$  in Fig. 4.15 for  $\delta = 1$ . The finite upper and lower diagonal elements indicate the nearest-neighbor bound pair whereas the diagonal elements in  $\Gamma_{ij}^{\uparrow\uparrow}$  and  $\Gamma_{ij}^{\downarrow\downarrow}$  ensure the formation of the  $\uparrow\uparrow$  and  $\downarrow\downarrow$  pairs. So, the system exhibits another condition of degenerate states for  $U_{\uparrow\downarrow} = U = 10J_{\uparrow}$ , where the particles prefer to be in states such as  $|(\uparrow\downarrow)_0\rangle$   $(\uparrow\downarrow)_1\rangle$ ,

$|(\uparrow\uparrow)_0 (\downarrow\downarrow)_1\rangle$ .

So, in the regime when  $U_{\uparrow\downarrow} < U = 5J_{\uparrow}$ ,  $5J_{\uparrow} < U_{\uparrow\downarrow} < 10J_{\uparrow}$  and  $U_{\uparrow\downarrow} > 10J_{\uparrow}$  the bosons favors to stay in the original configuration of  $|(\uparrow\uparrow)_0 (\downarrow\downarrow)_1\rangle$  without forming an inter-component bound state. This is because in the limit  $U_{\uparrow\downarrow} \geq U$  the breaking of the intra-component pair is energetically not favorable.

## 4.6 Repulsive U and attractive $U_{\uparrow\downarrow}$

The physics of bound state formation of non-local bosons discussed in the Sec. 4.3 and Sec. 4.5 are extremely sensitive to the nature of the interactions. The essential condition that energetically favours these features in the dynamics demands all the associated interactions ( $U_{\uparrow}$ ,  $U_{\downarrow}$  and  $U_{\uparrow\downarrow}$ ) are either repulsive or attractive. If different signs are considered then the inter-component bound states do not form in the dynamics. As an example we consider repulsive intra component interactions ( $U_{\uparrow}$  and  $U_{\downarrow}$ ) and attractive  $U_{\uparrow\downarrow}$  and study the QW using the initial states  $|\Psi(0)\rangle_I = a_{0,\uparrow}^{\dagger 2} a_{1,\downarrow}^{\dagger} |vac\rangle$  and  $|\Psi(0)\rangle_{II} = a_{0,\uparrow}^{\dagger 2} a_{1,\downarrow}^{\dagger 2} |vac\rangle$  in the following.

### 4.6.1 Two $\uparrow$ and one $\downarrow$ particles

The initial state we have considered here is  $|\Psi(0)\rangle_I = a_{0,\uparrow}^{\dagger 2} a_{1,\downarrow}^{\dagger} |vac\rangle$  and we plot the on-site density evolution ( $\langle n_i \rangle$ ), the density-density correlation ( $\Gamma_{ij}^{\uparrow\downarrow}$ ) and the two-particle correlation ( $\Gamma_{ij}^{\uparrow}$ ) in Fig. 4.16 (a), (b) and (c) respectively for  $\delta = 0.2$ . Here we consider  $U_{\uparrow} = U_{\downarrow} = U = 10J_{\uparrow}$  and  $U_{\uparrow\downarrow} = 0J_{\uparrow}$ ,  $-5J_{\uparrow}$ ,  $-10J_{\uparrow}$ ,  $-20J_{\uparrow}$ . From Fig. 4.16, we can conclude that, unlike the repulsive  $U_{\uparrow\downarrow}$  case, breaking of  $\uparrow\uparrow$  pair and formation of  $\uparrow\downarrow$  pair is forbidden. The finite diagonal elements in the plot showing the two-particle correlation matrices ( $\Gamma_{ij}^{\uparrow}$ ) in Fig. 4.16(c) confirms the formation of only  $\uparrow\uparrow$  pair for all values of  $U_{\uparrow\downarrow} \leq 0J_{\uparrow}$ .

### 4.6.2 Two $\uparrow$ and two $\downarrow$ particles

Now we consider the state  $|\Psi(0)\rangle_{II} = a_{0,\uparrow}^{\dagger 2} a_{1,\downarrow}^{\dagger 2} |vac\rangle$  as the initial state. We plot the on-site density evolution ( $\langle n_i \rangle$ ) and the density-density correlation ( $\Gamma_{ij}^{\uparrow\downarrow}$ ) in Fig. 4.17 (a) and (b) respectively for  $\delta = 0.2$ ,  $U_{\uparrow} = U_{\downarrow} = U = 10J_{\uparrow}$  and  $U_{\uparrow\downarrow} = 0J_{\uparrow}$ ,  $-2J_{\uparrow}$ ,  $-5J_{\uparrow}$ ,  $-8J_{\uparrow}$ ,  $-10J_{\uparrow}$ ,  $-20J_{\uparrow}$ . It can be clearly seen from Fig. 4.17(a) that the wavepacket of the  $\uparrow\uparrow$  pair gets reflected from that of the strongly bound  $\downarrow\downarrow$  pair for all finite values of  $U_{\uparrow\downarrow}$ . Note that the slow spreading of the  $\downarrow\downarrow$  is due to weak hopping strength. The reflection in this case can also be observed from the

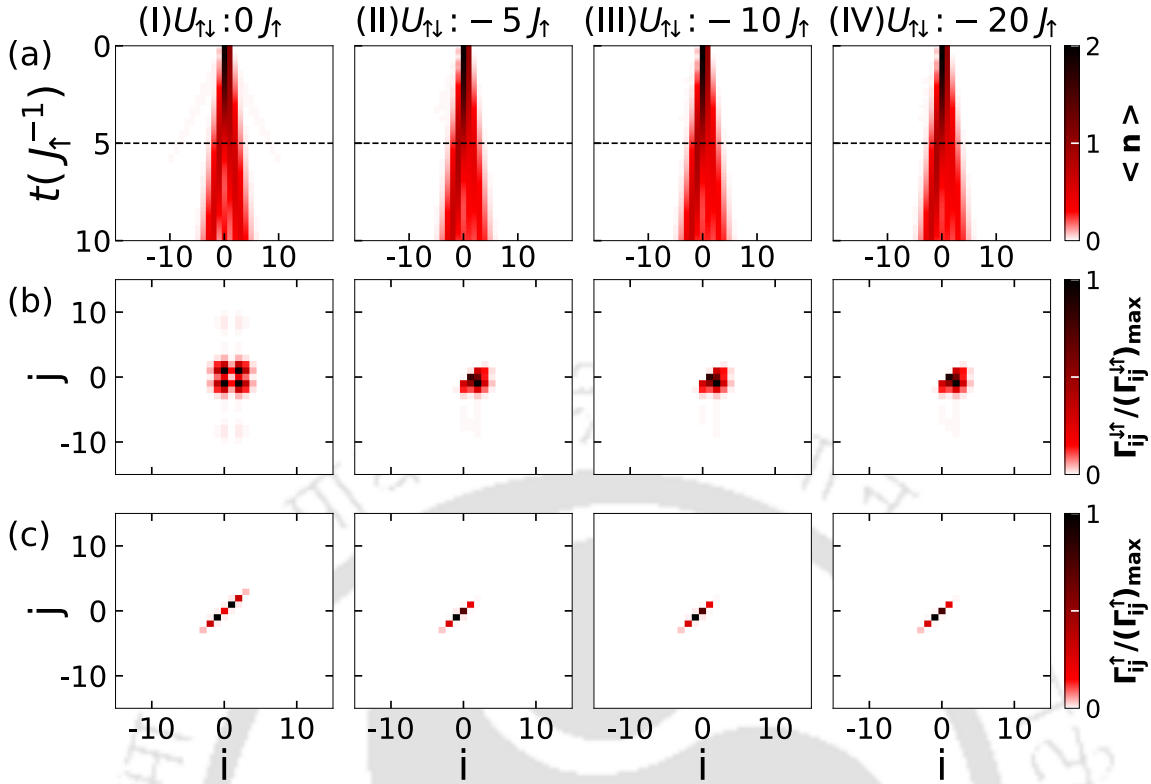


**Figure 4.16:** Panel (a) shows the density evolution of the initial state  $|\Psi_0\rangle = a_{0,\uparrow}^{\dagger 2} a_{1,\downarrow}^{\dagger} |vac\rangle$  for  $U_{\uparrow\downarrow} = 0J_{\uparrow}$ ,  $-5J_{\uparrow}$ ,  $-10J_{\uparrow}$  and  $-20J_{\uparrow}$ . Here  $U = 10J_{\uparrow}$  and  $\delta = 0.2$ . In Panel (b) and (c) are shown the correlation functions  $\Gamma_{ij}^{\downarrow\uparrow}$  and  $\Gamma_{ij}^{\uparrow\downarrow}$  respectively at time,  $t = 5J_{\uparrow}^{-1}$ .

vanishing of the upper triangular matrix elements of  $\Gamma_{ij}^{\uparrow\downarrow}$  as depicted in Fig. 4.17(b). In this case we do not see any triplon or nearest neighbour pairing.

## 4.7 Conclusions

We obtained local bound states in the QWs of initially non-local bosons with only local interactions in the two-component Bose-Hubbard model. We have shown that the non-trivial inter-component bound states can be formed at specific critical ratios of inter and intra-component interaction strengths. An inter-component bound pair is formed by considering three particles in total when both intra- and inter-component interactions are of equal strength. However, when two particles from each component are considered, a stable triplon is formed when the inter-species interaction is half of the intra-species ones. Moreover, we have obtained that a finite hopping asymmetry between the components plays an essential role in favouring a more stable inter-component bound pair. We have also shown that the QWs exhibit

a re-entrant phenomenon as a function of the inter-component interaction.

The many-body physics of two different types of particles or two-component systems has been a topic of great interest in its own right [154] in condensed matter physics. Compared to the system with identical particles, the two-component systems are a much richer platform enabling access to a larger parameter space due to the presence of both intra- and inter-component interactions. The present analysis opens up possibilities for further exploration in the context of the quantum walk of two-component bosons, such as the effects of NN interactions and disorder. Due to the rapid progress in the manipulation of ultracold binary atomic mixture in optical lattices [102–108], many physical phenomena involving two-component bosons, fermions and Bose-Fermi mixtures have been predicted [109–116, 118–120, 155] and observed [33, 117, 156] in the framework of the Hubbard and the two-component Bose-Hubbard models. Therefore, our findings can in principle, be simulated in a system of two-component Bose mixture in optical lattices by controlling the inter- and intra-component interactions by the Feshbach resonance and the individual hopping strengths by the state-dependent optical lattice [109, 121–123, 143].

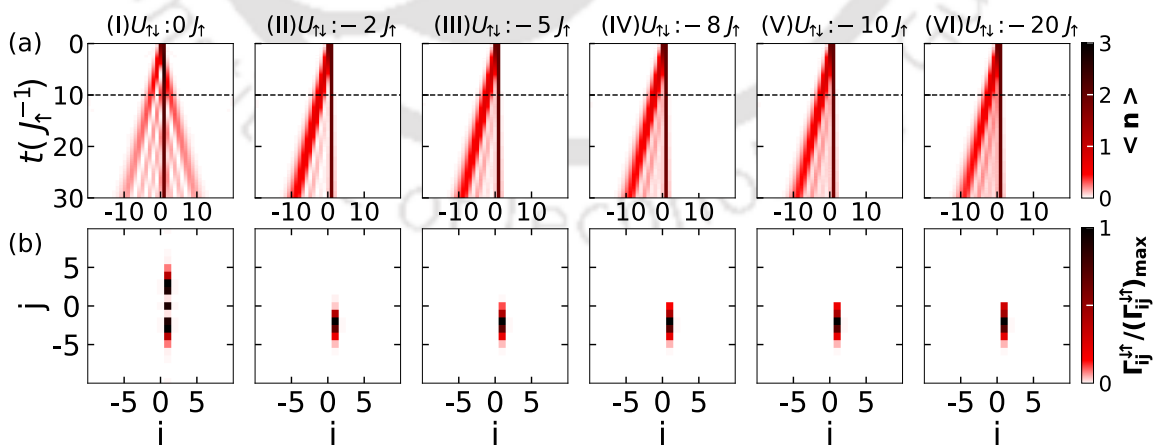


**Figure 4.17:** Panel (a) shows the density evolution of the initial state  $|\Psi_0\rangle = a_{0,\uparrow}^\dagger a_{1,\downarrow}^\dagger |vac\rangle$  for  $U_{\uparrow\downarrow} = 0J_{\uparrow}, -2J_{\uparrow}, -5J_{\uparrow}, -8J_{\uparrow}, -10J_{\uparrow}$  and  $-20J_{\uparrow}$ . Here  $U = 10J_{\uparrow}$  and  $\delta = 0.2$ . Panel (b) shows the correlation functions  $\Gamma_{ij}^{\uparrow\downarrow}$  at time,  $t = 10J_{\uparrow}^{-1}$ .



## Chapter 5

# Quantum walk of interacting bosons in Harper-Hofstadter ladder

### 5.1 Introduction

In the last two chapters, we have discussed the QW of two-component systems in one dimension. Interestingly, the model describing the two-component bosons in a one-dimensional lattice (Eq. 4.1) resembles to a two-leg Bose-Hubbard ladder as shown in Fig. 5.1. Here the particles residing in the individual legs can be regarded as the two different components. The onsite interactions (hoppings) in individual legs correspond to the intra-component onsite interaction (hoppings) and the interaction along the rung of the ladder is equivalent to the inter-component interactions in Eq. 4.1. Apart from this the inter-leg hopping on a Bose-Hubbard ladder is equivalent to the inter-particle exchange. Ladder geometries are extremely important systems in condensed matter physics as they carry the structure of several interesting compounds which have been studied in great detail. Moreover, the physics of the ladder system provides a simple extension to the one-dimensional lattice toward the two-dimensional system. Due to the recent progress in the field of cold atoms in optical lattices, it has been made possible to create ladder lattices and study quantum phase transitions [157–160]. Several theoretical studies have been performed to predict novel physical properties in such quasi-one-dimensional systems [161–165]. On the other hand, the interplay between quantum mechanical particles and artificial gauge fields in continuum [166, 167] and periodic systems [168–170] have allowed to the study of quantum phase transitions and topological phases [128, 159, 169, 171]. Apart from the two-dimensional system, numerous efforts have been made in recent years to understand the physics of two-leg ladder systems in the presence of mag-

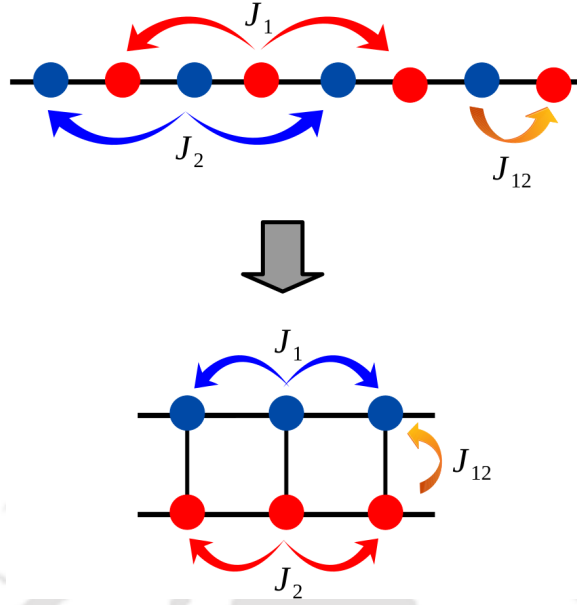


**Figure 5.1:** The figure describes the two component bosons in one dimensional lattice resembling to a two-leg Bose-Hubbard ladder.

netic fields [172–175] which are the smallest possible structure to host such effects. The bosonic version of such a system in the context of optical ladders was also analysed, resulting in various exciting phenomena related to the chiral nature of the particles and the subsequent experimental observations [159, 176–178]. While the non-interacting systems exhibit the chiral physics arising due to the presence of the magnetic field, the presence of interaction introduces novel phenomena which have been widely discussed in recent years [179–192].

Although the experimental demonstration of such interacting complex systems is difficult, the chiral motion has been observed recently in the quantum walk of two interacting particles on a ladder optical lattice [144]. By allowing uniform flux threading across the plaquettes of the ladder, the chiral motion has been probed in the presence of interaction by using quantum gas microscopy. However, a detailed understanding of the CTQW with varying interaction and changing flux strength and pattern is yet to be studied.

Motivated by these developments, we study the CTQW of two interacting bosonic particles on a two-leg ladder subjected to both uniform and staggered magnetic fields as depicted in Fig. 5.2(a) and (b), respectively. We show that interaction and flux have significant effects on the quantum walk. By considering different two particles initial states we study the effect of the magnetic field on the spreading of the wavefunction, chiral motion and bound state formation.

When the two particles are located at the two sites of the rung in the initial

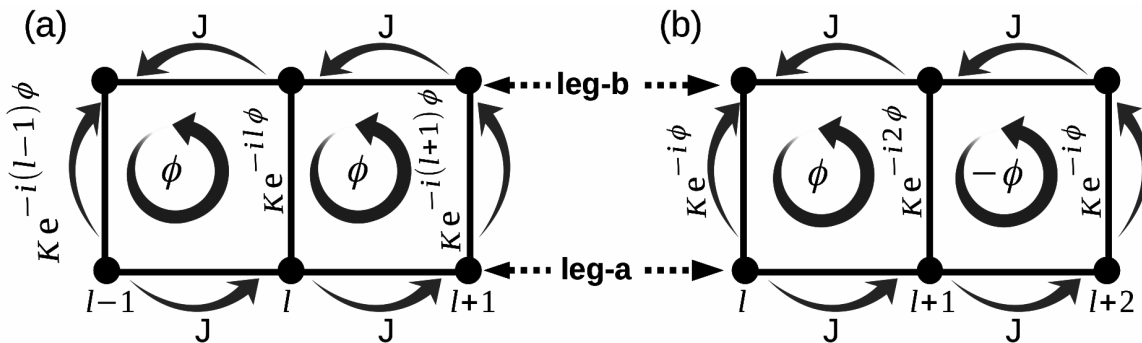


**Figure 5.2:** Schematic diagram depicting two-leg Bose-Hubbard ladder in the presence of (a) uniform flux and (b) staggered flux.

state, we find that increasing flux strength slows down the overall spreading of the particle wavefunction. However, the slowing down is found to be more substantial in the presence of the staggered flux than the uniform flux. Interestingly, the chiral motion of the particles that occurs in the presence of uniform flux ceases to occur in staggered flux. On the other hand, when the two particles are located at the same site, we get signatures of repulsively bound pair (RBP) formation [2, 94, 116, 193]. When the onsite interaction is comparable to the hopping strength, the formation of bound pair is forbidden. Interestingly, we find that the presence of flux favours the formation of RBP. In the following, we discuss these phenomena in detail.

## 5.2 Model

The Hamiltonian describing the system of bosons in a two-leg ladder with a uniform flux (Fig. 5.2(a)) is given by the interacting Harper-Hofstadter (HH) Hamiltonian;

$$\begin{aligned}
 H_u = & \frac{U}{2} \sum_{l,p \in a,b} \hat{n}_{l,p}(\hat{n}_{l,p} - 1) - J \sum_l (\hat{a}_l^\dagger \hat{a}_{l+1} + \hat{b}_l^\dagger \hat{b}_{l+1}) \\
 & - K \sum_l e^{-il\phi} (\hat{a}_l^\dagger \hat{b}_l + h.c.),
 \end{aligned} \tag{5.1}$$

where the operator  $p_l$  ( $p_l^\dagger$ ) annihilates (creates) a bosonic particle at site  $l$  of leg  $p$  ( $= a, b$ ) and  $n_{l,p}$  is the on-site number operator at site  $l$  of leg  $p$  ( $= a, b$ ).  $J$  and  $K$  denote the amplitude of the intra-leg and inter-leg hopping respectively. The inter-leg hopping term is complex in nature and introduces an artificial gauge field  $B$  of flux  $\phi = \frac{e}{\hbar} \int_{r_i}^{r_f} d\tilde{\mathbf{r}} \cdot \mathbf{A}(\tilde{\mathbf{r}})$ , where  $\mathbf{A}(\tilde{\mathbf{r}})$  is the magnetic vector potential. We perform our calculations in the Landau gauge  $\mathbf{A}(\tilde{\mathbf{r}}) = Bx\hat{y}$  with the phase  $\phi = \pi\Phi/\Phi_0$ , where  $\Phi$  is the magnetic flux through each plaquette and  $\Phi_0 = h/e$  is the magnetic flux

quantum.

For the case of a staggered flux threading through the ladder, where the flux in adjacent plaquettes are aligned in the opposite direction (see Fig. 5.2(b)), the Hamiltonian is given by

$$\begin{aligned}
 H_s = & \frac{U}{2} \sum_{l,p \in a,b} \hat{n}_{l,p}(\hat{n}_{l,p} - 1) - J \sum_l (\hat{a}_l^\dagger \hat{a}_{l+1} + \hat{b}_l^\dagger \hat{b}_{l+1}) \\
 & - K \sum_{l \in \text{odd}} (\hat{a}_l^\dagger \hat{b}_l e^{-i\phi} + h.c.) - K \sum_{l \in \text{even}} (\hat{a}_l^\dagger \hat{b}_l e^{-i2\phi} + h.c.).
 \end{aligned} \tag{5.2}$$

We study the CTQW of interacting bosons initially located at the central rung of the ladder following the standard protocol of unitary time evolution as

$$|\Psi(t)\rangle = \mathcal{U}(t, t_0) |\Psi(t_0)\rangle, \tag{5.3}$$

where  $\mathcal{U}(t, t_0) = e^{-iH_{u,s}(t-t_0)/\hbar}$ . The analysis is done by exactly solving the models shown in Eq. 5.1 and Eq. 5.2 with different system sizes.

Note that the dynamics of two interacting bosons in the context of the uniform flux model given by Eq. (5.1) has recently been studied in detail and experimentally observed in systems of ultracold atoms in optical lattices [194]. In the case of only one particle at the central rung, the chiral motion has been observed by tracking the center of mass coordinate along the  $y$ -direction of the ladder. It has been shown that for values of flux between  $0 < \phi < \pi$  the particle moves with finite probabilities in both the rungs in the opposite direction. However, the presence of two-particle state in the central rung exhibits different features for both zero and non-zero interaction strength  $U$ . While in the case of vanishing interaction, no chiral motion was observed, the presence of finite interaction introduces the chiral motion in the dynamics. While the role of interaction and large rung hopping situation have been studied in detail in the presence of uniform flux, the dynamics of the bosonic particle in the presence of non-uniform flux, strong interaction and with respect to different initial conditions has not yet been discussed.

Taking the idea discussed in [194] further, in this work we investigate the role of staggered nature of flux on the dynamics of two interacting bosons on a ladder and make a comparative investigation with the already well-studied case of the uniform flux [194]. Moreover, we extend our investigation by considering a different initial state where two particles are located at a single site on the central rung. In our calculations, we use the hopping strength  $J = 1$  and  $K = 3$  as considered in the

experiment of Ref. [194] and study the quantum walk by varying  $U$  and  $\phi$ . We explore the scenario with equal hopping i.e.  $J = K$  and a different initial state where atoms are located at a single site of the central rung.

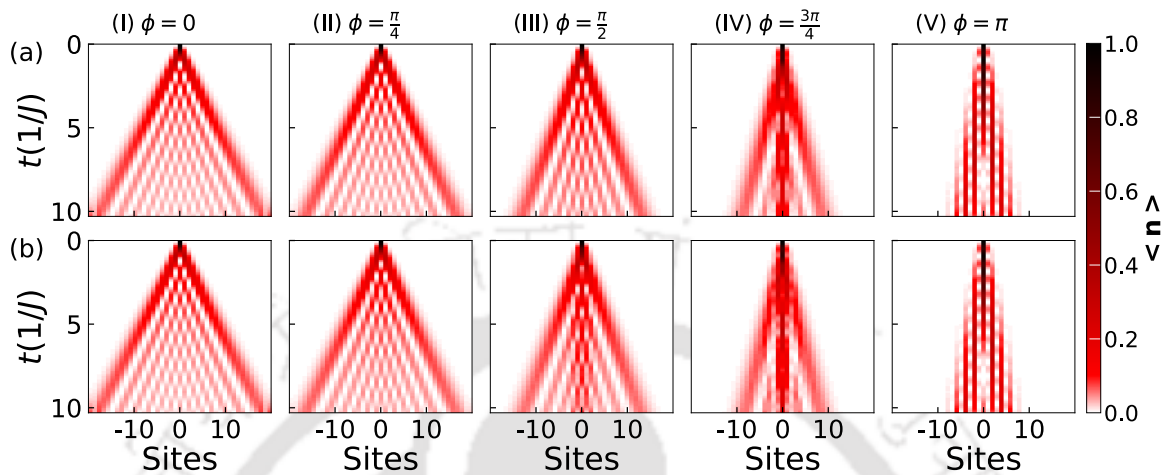


**Figure 5.3:** The figure shows the single-particle QW in the two-leg ladder system of length  $L = 41$ . Panel (a) and (b) correspond to the uniform and staggered flux, respectively. Here we consider  $J = 1$  and  $K = 3$ .

## 5.3 Results

In this section we discuss our main findings in detail. Before proceeding to the interacting case, we first discuss the CTQW of a single-particle initial state in the presence of both uniform and staggered flux.

### 5.3.1 Single-particle Quantum walk

For the single-particle case we consider an initial state given as

$$|\Psi_0\rangle = \frac{1}{\sqrt{2}}(|a, 0\rangle + |b, 0\rangle), \quad (5.4)$$

which corresponds to a boson delocalised at the central rung of the ladder and analyse the CTQW for different values of flux  $\phi$ . In Fig. 5.3, we show the time evolution of the particle density  $\langle n_i \rangle$  for different values of uniform flux (Fig. 5.3(a)) as well as the staggered flux (Fig. 5.3(b)), which clearly display the light-cone type spreading corresponding to the ballistic expansion. We find that the overall spreading slows down with the increase in the flux strength in both the cases, indicating an increased localization of particles around the initial position with an increase in the magnetic

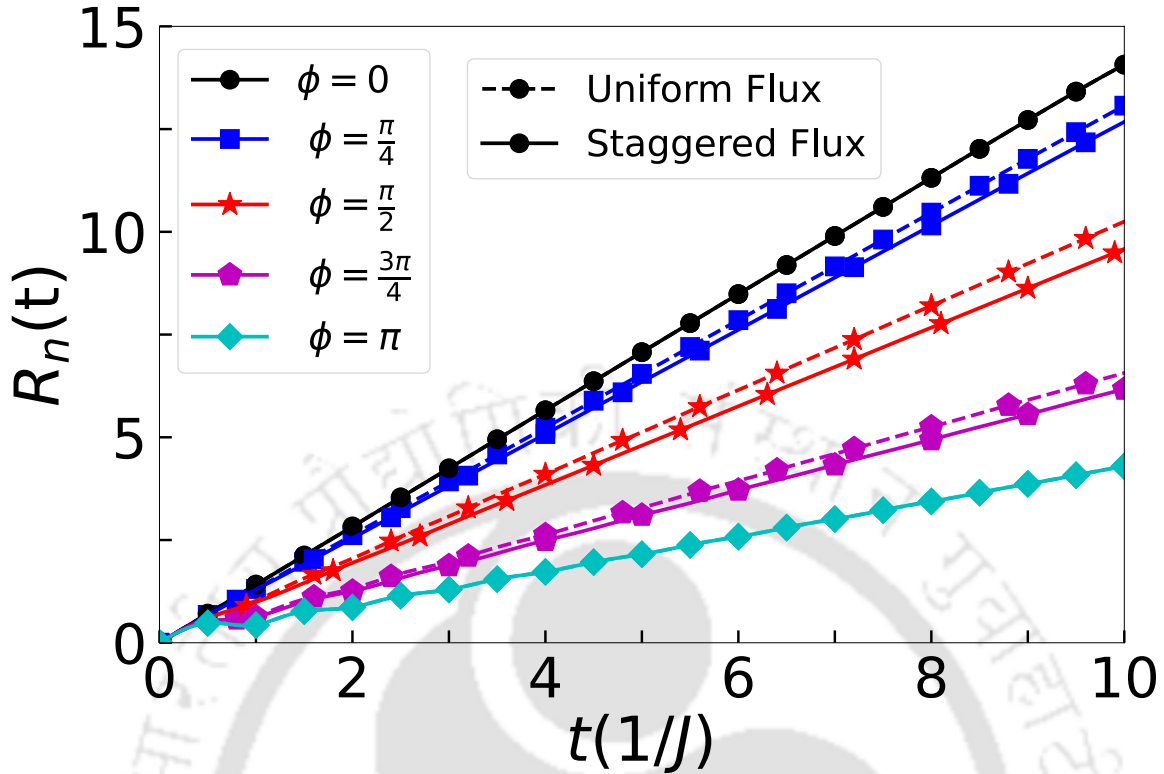


**Figure 5.4:** The figure shows the radius of propagation  $R_n(t)$  in the presence of the uniform (dashed line) and staggered (solid line) flux in a two-leg ladder system of length  $L = 41$ . Here we consider  $J = 1$  and  $K = 3$ .

field. Interestingly, the slowing down is stronger for the case of staggered flux when compared to the uniform flux case. This behaviour can be clearly distinguished by looking at the radius of expansion  $R_n(t)$  defined as

$$R_n(t) = \sqrt{\sum_{i=1}^L (i - i_0)^2 n_i(t)} \quad (5.5)$$

where  $i_0 = L/2$  and  $L$  is the length of the ladder. We plot  $R_n(t)$  as a function of time  $t$  for different values of  $\phi$  for both uniform (dashed line) and staggered (solid line) flux cases as shown in Fig. 5.4. The overall ballistic expansion can be seen from the behaviour of  $R_n(t) \propto t$ . There is also a clear signature of reduction in radial velocity (increase in slope of  $R_n(t)$ ) with respect to an increase in magnetic flux  $\phi$ . Moreover, we report that for each value of  $\phi$ , the radial velocity due to the uniform flux is comparatively higher than that for the staggered flux case. This can be understood from the dispersion relation of the Bloch bands shown in Fig. 5.5. Since the velocity of the walker depends on the slope of the dispersion band, the

enhanced flattening of the band for staggered flux (Fig. 5.5(b)) compared to the uniform flux (Fig. 5.5(a)) case leads to the suppression of the radial velocity for the former case.

As already discussed in Ref [194], the single-particle in a HH ladder (uniform flux

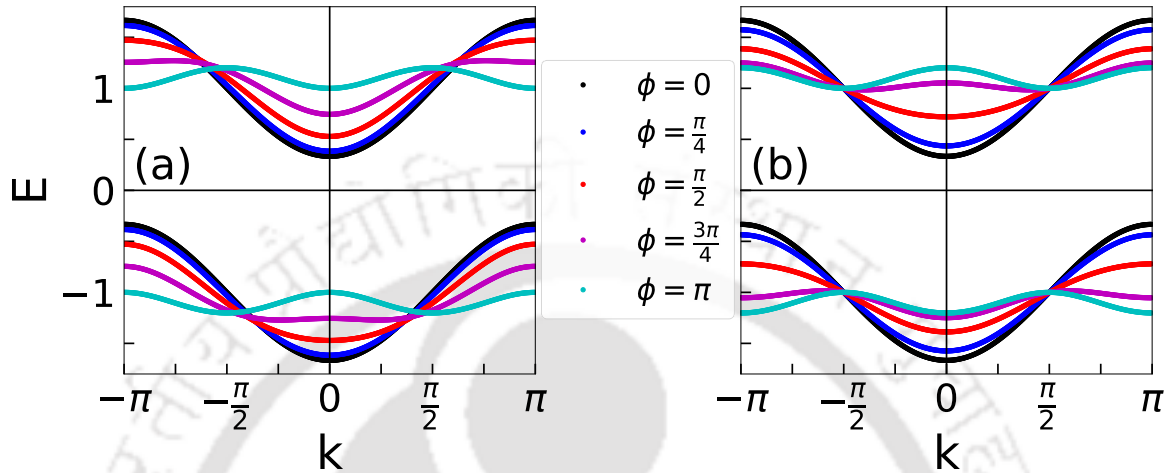


**Figure 5.5:** The figure shows the dispersion curve for different  $\phi$  values. Figures (a) and (b) correspond to the uniform and staggered flux, respectively. Here we consider  $J = 1$  and  $K = 3$ .

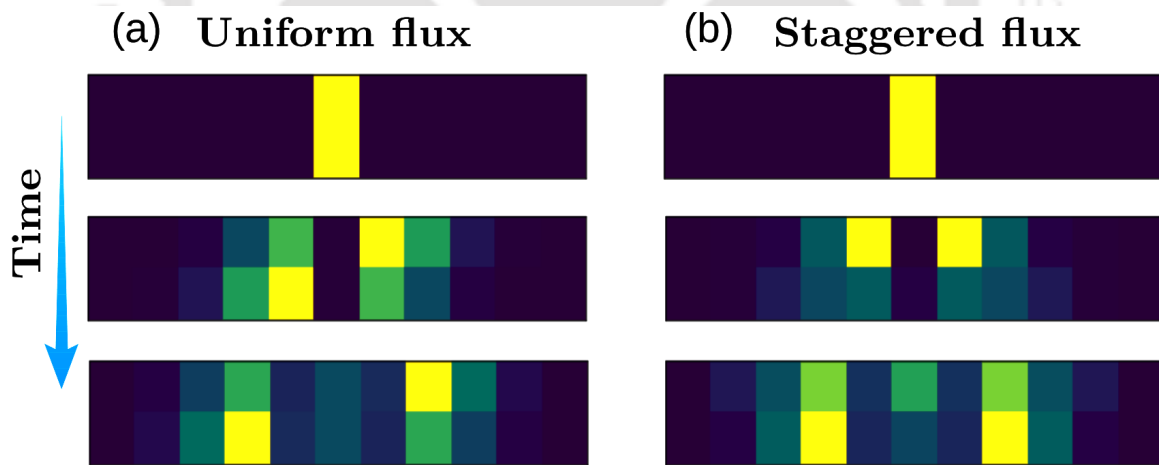


**Figure 5.6:** The figure shows the single-particle QW in the presence of (a) the uniform flux and (b) the staggered flux. Left: In the uniform flux, chiral motion is present in QW. Right: In the staggered flux, chiral motion is absent in QW.

case) possess chiral motion along the legs of the ladder which can be understood from the QW shown in Fig. 5.6 (left panel). However, this chiral motion disappears in the presence of staggered flux and the particle density oscillates between the legs of the ladder as shown in Fig. 5.6 (right panel). Further insight into the difference in

particle dynamics and the chiral motion can be obtained by calculating the difference in number densities between the legs on the two sides of the central rung as ;

$$\begin{aligned} C_{nR} &= \langle n_{b,1} \rangle - \langle n_{a,1} \rangle \\ C_{nL} &= \langle n_{b,-1} \rangle - \langle n_{a,-1} \rangle \end{aligned} \quad (5.6)$$

Here  $C_{nR}$  ( $C_{nL}$ ) denotes the density difference between the legs to the right (left) from the central rung located at the  $0^{\text{th}}$  site. We plot  $C_{nR}$  and  $C_{nL}$  in Fig. 5.7

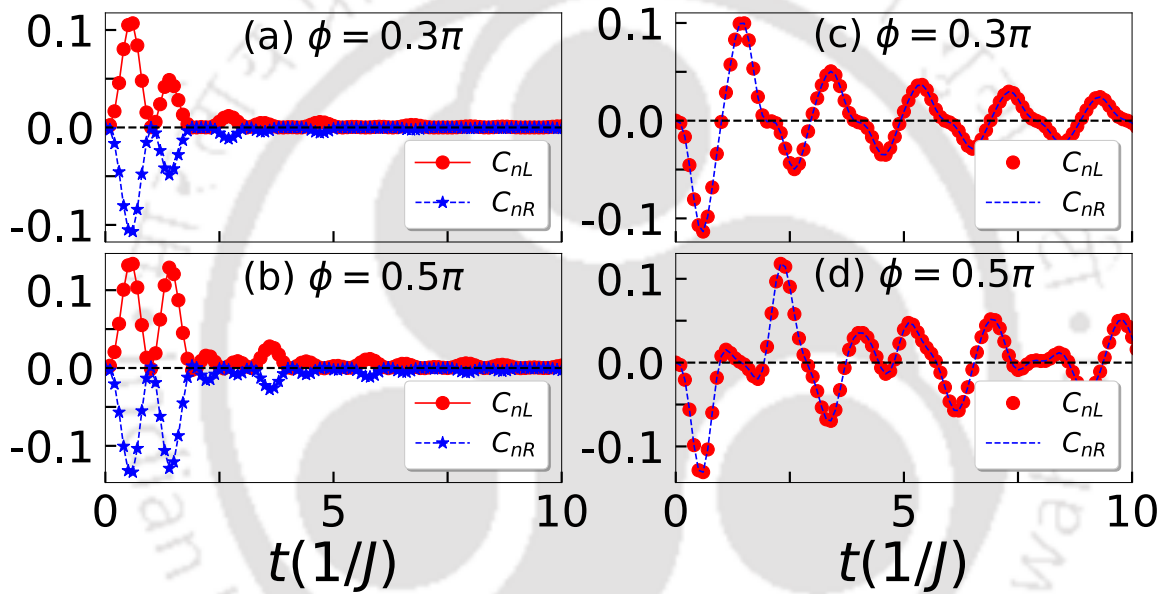


**Figure 5.7:** This figure shows the chirality defined in Eq. 5.6. (a)-(b) correspond to the uniform flux case and (c)-(d) corresponds to the staggered flux case. Here we consider  $J = 1$ ,  $K = 3$  and flux values  $\phi = (0.3\pi, 0.5\pi)$ .

for both the uniform (Fig. 5.7 (a, b)) and staggered flux (Fig. 5.7 (c, d)) cases for two different values of  $\phi = 0.3\pi$  and  $0.5\pi$  for each cases. The equal distribution of the particle's probability in both the legs during the chiral motion ensures that  $C_{nR} = -C_{nL}$  for the case of uniform flux (Fig. 5.7 (a, b)). However, for the case of staggered flux,  $C_{nR} = C_{nL}$  indicates the absence of the chiral motion as shown in Fig. 5.7 (c, d). These features associated to chirality can be understood from the chirality of the Bloch bands quantified in Ref. [194] as

$$C^\tau(k) = \text{sign}(v_g^\tau(k)) \times (p_b^\tau(k) - p_a^\tau(k)), \quad (5.7)$$

for any quasi-momentum  $k$ . Where  $sign(v_g^\tau(k))$  denotes the sign of the group velocity,  $p_{b,a}^\tau(k)$  probability amplitudes for a particle to reside on the leg-b or leg-a of the ladder and  $\tau = \pm$  represents the two band of the ladder. We plot  $C(k)$  (as color code) along with the Bloch bands in Fig. 5.8 (a,b) and (c,d) for uniform and staggered flux, respectively. In order to have the chiral nature, the upper and the lower

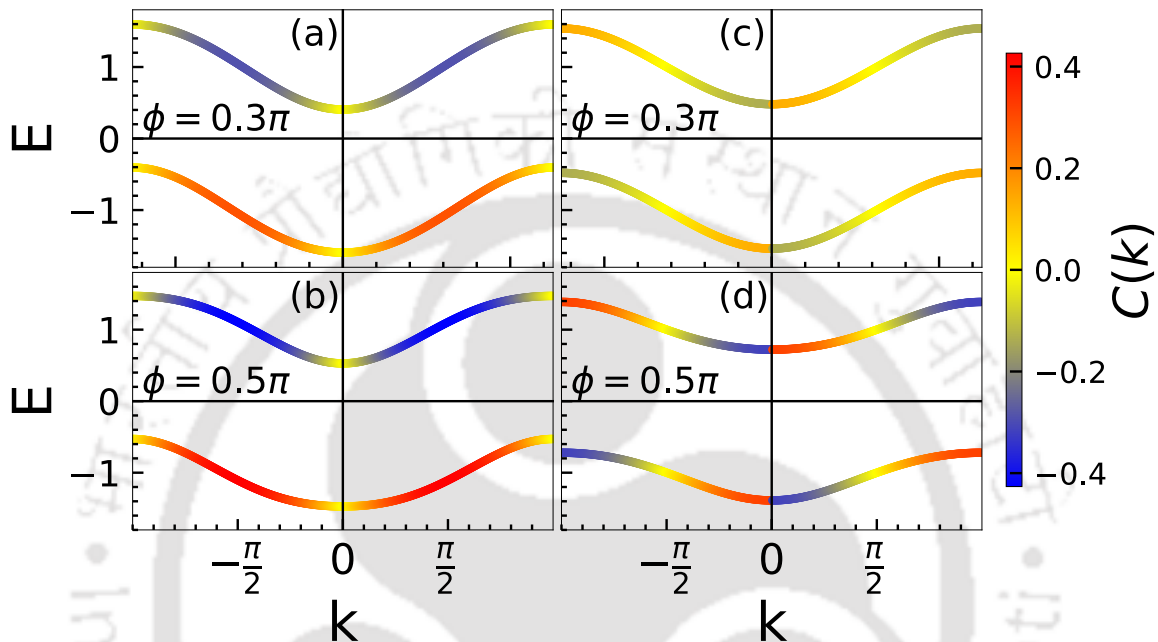


**Figure 5.8:** The figures show the chirality of the Bloch bands. The dispersion relations of the two Bloch bands are plotted for  $J = 1$  and  $K = 3$ . (a)-(b) correspond to the uniform flux, and (c)-(d) corresponds to the staggered flux. The color code indicates the chirality  $C(k)$  of the two bands. For each case we have considered  $\phi = 0.3\pi$  and  $\phi = 0.5\pi$ .

bands must have opposite chirality with respect to the positive ( $+k$ ) and negative ( $-k$ ) quasi-momentum. For example, in Fig. 5.8(b), for  $k = \pi/2$ , the upper band possesses negative chirality while for  $k = -\pi/2$ , the lower band possesses positive chirality. Similarly, in Fig. 5.8 (c) and (d), for positive and negative momentum, the upper and lower bands have identical chirality which indicates the absence of any chirality in the staggered flux case. Besides the chirality, we also compare the total leg density defined as

$$n_a = \sum_{-L/2}^{L/2} n_{a,i} \quad \text{and} \quad n_b = \sum_{-L/2}^{L/2} n_{b,i} \quad (5.8)$$

on leg- $a$  and leg- $b$  respectively in Fig. 5.9. Since initially the single-particle is located along the central rung, the effective density on each leg of the ladder is 0.5. Inter-

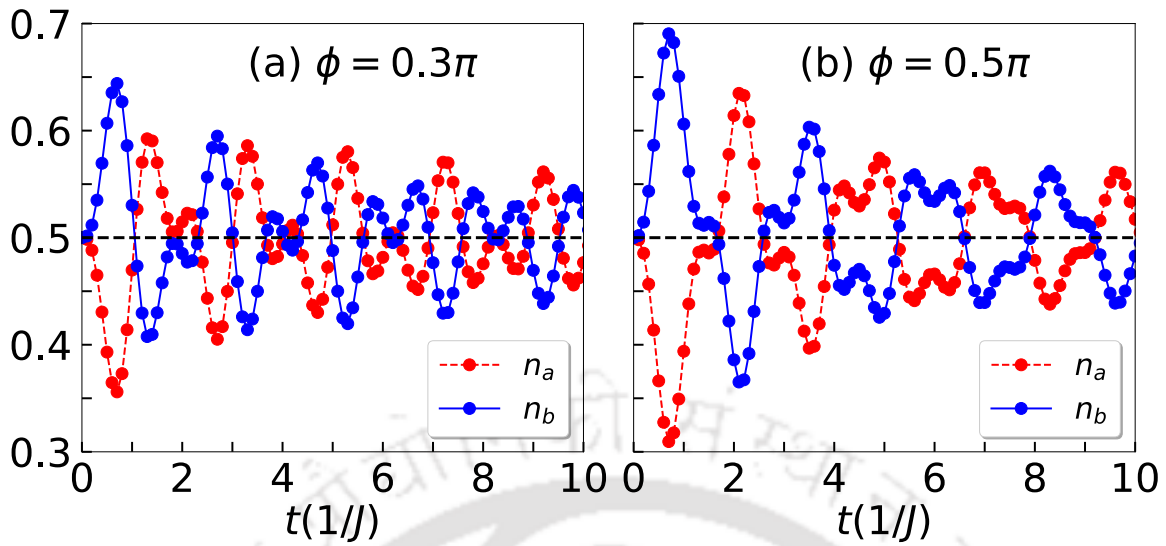


**Figure 5.9:** The figure shows the evolution of  $n_a$  and  $n_b$  defined in Eq. 5.8. (a) and (b) correspond to  $\phi = 0.3\pi$  and  $0.5\pi$ , respectively. The symbols are for staggered flux case and the black dashed line is for uniform flux case. Here we consider  $J = 1$  and  $K = 3$ .

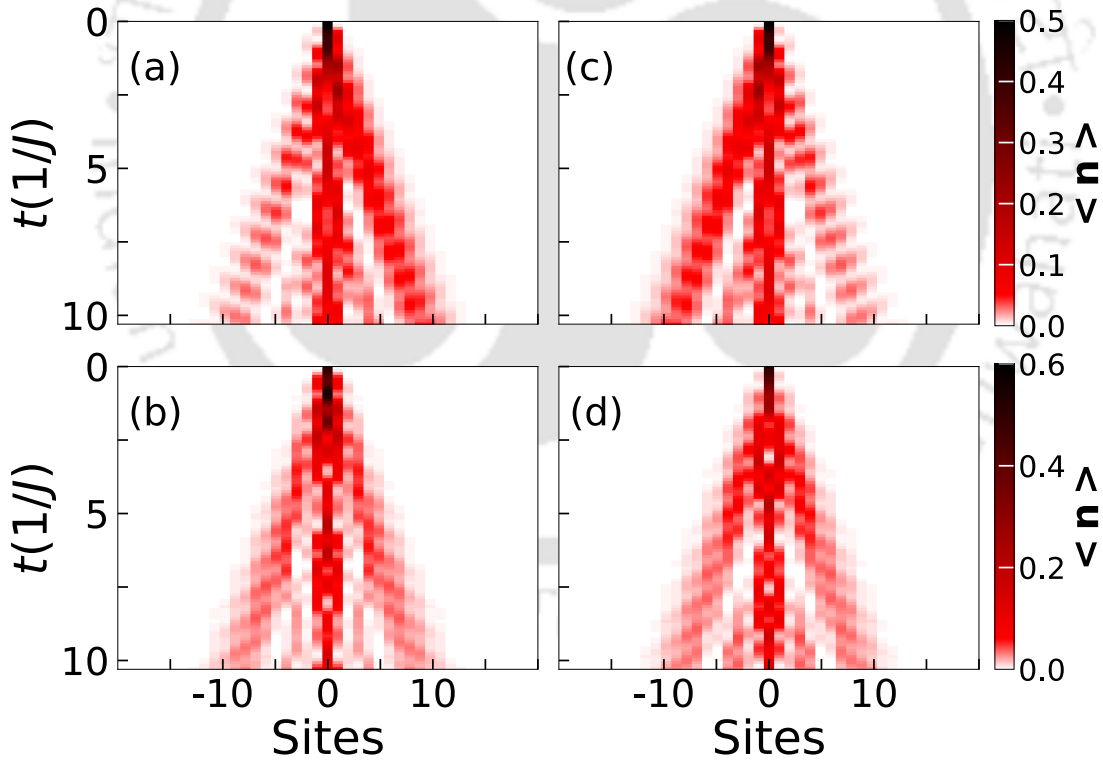


**Figure 5.10:** Figures (a) and (c) show the density evolution of leg-a and leg-b in the presence of the uniform flux, respectively. Figures (b) and (d) show the density evolution of leg-a and leg-b in the presence of the staggered flux, respectively. Here  $J = 1$ ,  $K = 3$  and flux value is  $\phi = \frac{3\pi}{4}$ .

estingly, we find that in the presence of uniform flux, due to fixed chiral motion, the densities on each leg remain constant during the time evolution i.e.,  $n_a = n_b = 0.5$  which are shown as the black dashed lines in Fig. 5.9 (a) and (b) respectively.

However, in the presence of staggered flux, both  $n_a$  (red circles) and  $n_b$  (blue circles) oscillate symmetrically around the mean value 0.5 and the oscillation amplitude decays during the time evolution as the particle densities get distributed throughout the lattice during the QW. We can also see this behaviour from the evolution of onsite densities of the individual legs. In Fig. 5.10(a) and (c), we plot  $\langle n_i \rangle$  of leg- $a$  and leg- $b$  respectively for uniform flux of strength  $\phi = \frac{3\pi}{4}$ . It can be seen that the leg- $a$  (leg- $b$ ) density evolution is biased towards the right (left) side of the lattice and there is no change in total density in each leg from its average value. Similarly in Fig. 5.10(b) and (d), we plot the evolution of density of leg- $a$  and leg- $b$  respectively for the case of staggered flux of strength  $\phi = \frac{3\pi}{4}$ . In this case, however, the densities spread symmetrically around the initial position in both the legs. In the following, we extend these analysis for the case of interacting particles and study the interplay and combined role of interaction and flux strength.

### 5.3.2 Two-particle Quantum Walk

In this section we present the study of the physics of two interacting particles on the HH ladder for both uniform and staggered flux cases. Starting with an initial state

$$|\Psi_0\rangle = a_{a,0}^\dagger a_{b,0}^\dagger |vac\rangle, \quad (5.9)$$

we particularly investigate the influence of the onsite interaction strength  $U$  and the flux strength  $\phi$  on the QW. The initial state  $|\Psi_0\rangle$  corresponds to a two-particle state created at the central rung with one particle at each site of the rung. It is to be noted that the dynamics of this state under the influence of uniform flux  $\phi$  and finite onsite interaction strength  $U$  has been discussed in detail in Ref.[194], where the focus was primarily on the chiral motion of the particles. The experimental and theoretical analysis in the presence of uniform flux reveals the non-chiral (chiral) motion in the absence (presence) of interaction. The absence of chirality in the non-interacting regime has been attributed to the symmetric population of the chiral bands which gets broken when the onsite interaction  $U$  is finite. However, a detailed analysis of the QW with respect to varying interaction strength and flux patterns is yet to be fully explored, and we present our detailed study as follows. In the following, we study the influence of the interaction strength  $U$  and flux strength  $\phi$  (for both

the uniform and staggered flux cases) on the QW with an initial state  $|\Psi_0\rangle$  given in Eq. 5.9. We first examine the onsite density evolution of the two particles in

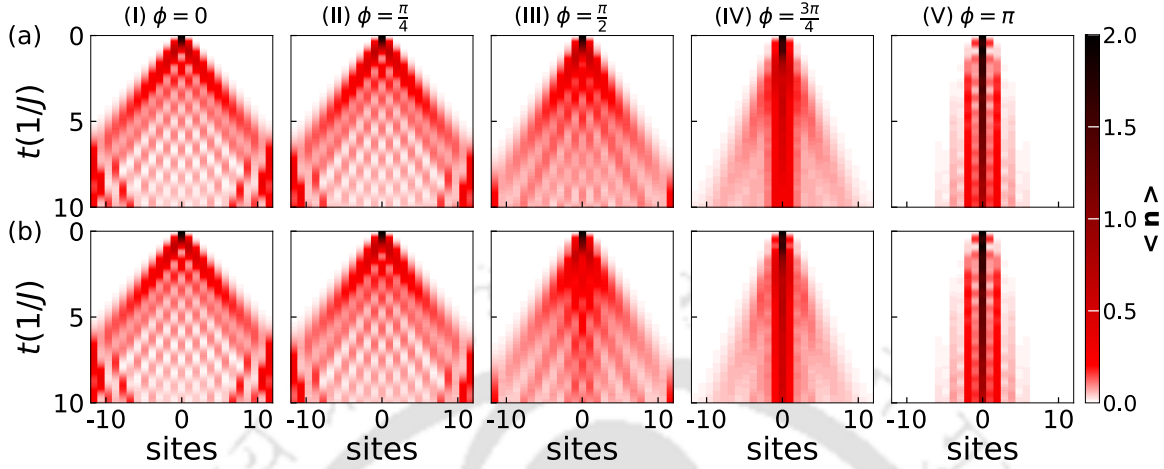


**Figure 5.11:** Figure shows the density evolution of the two particles with the initial state  $|\Psi_0\rangle = a_{a,0}^\dagger a_{b,0}^\dagger |vac\rangle$  in a ladder system of length  $L = 25$ . Panel (a) and (b) show the density evolution in the presence of the uniform flux and the staggered flux, respectively. Here we consider  $U = 4$ ,  $J = 1$ ,  $K = 3$  and the length of the ladder is  $L = 25$ .

the presence of uniform flux and staggered flux for  $U = 4$  in panel (a) and (b) respectively in Fig. 5.11 for different values of  $\phi$ . Similar to the single-particle case, we find that for both the types of flux, the spreading of density comes out to be generally suppressed with increase in flux strengths, and the suppression is relatively stronger for the case of staggered flux when compared to the uniform flux case. Furthermore, in order to understand the combined effect of the interaction strength  $U$  and the flux strength  $\phi$ , we plot the radius of propagation  $R_n(t)$  (Eq. 5.5) for different values of the interaction strengths  $U = 0$ ,  $U = 6$ , and  $U = 20$  for a fixed flux strength  $\phi = 3\pi/4$  in Fig. 5.12. The solid lines with circles and solid lines with stars denote the uniform and staggered flux cases, respectively. For comparison we have shown the curves for the flux strength  $\phi = 0$  (dashed) for all the considered values of interaction strengths. It can be clearly seen that for the non-interacting case ( $U = 0$ ), the suppression of the radius of propagation is stronger for the case of staggered flux as compared to the uniform flux. As already discussed in Ref. [194], increasing the interaction strength also reduces the radial distance. Interestingly, we find that after a particular value of the interaction strength  $U$ , the  $R_n(t)$  increases again with time and it is clearly demonstrated in Fig. 5.12. Similar features are observed for the staggered flux case as well. However, the slowing down of expansion is more prominent here when compared with the uniform flux case (see Fig. 5.12). To quantify this behaviour further, we plot the radial velocity  $V$ , as a function of

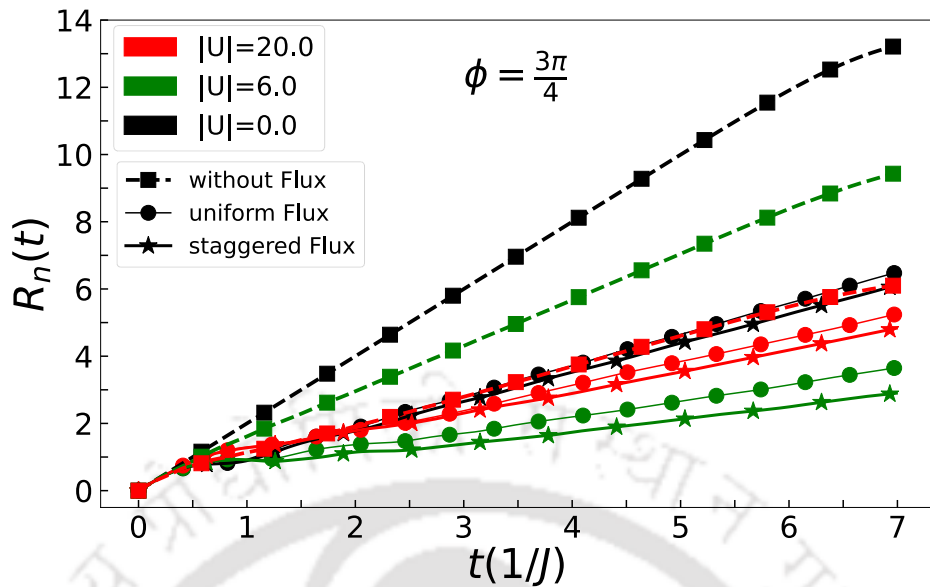


**Figure 5.12:** The figure shows the radius of propagation  $R_n(t)$  in the presence of the uniform and staggered flux in a ladder system of length  $L = 25$ . Here we consider  $J = 1$  and  $K = 3$ .

the onsite interaction strength  $U$  for both the uniform and staggered flux case in Fig. 5.13 (a) and (b) respectively at a particular time of evolution. It can be seen that in both the cases, for zero interaction strength,  $V$  falls down as  $\phi$  increases. However, as the interaction strength  $U$  increases,  $V$  initially falls down and then increases, exhibiting an interesting re-entrant feature. This is true for all the values

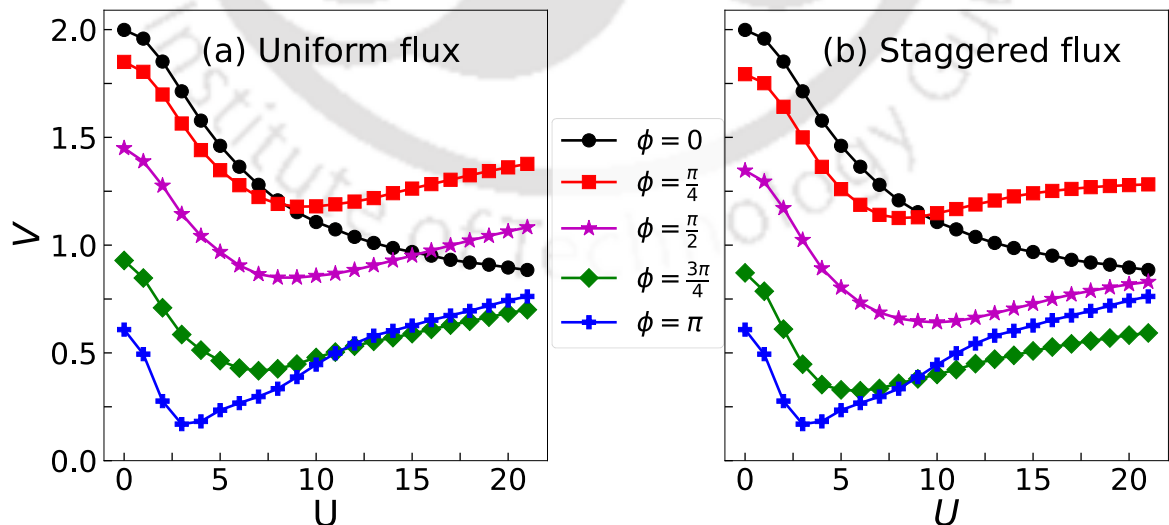


**Figure 5.13:** The figure shows the radial velocity  $V$  of the wavefunction as a function of  $U$  in the presence of (a) the uniform flux and (b) the staggered flux. Here we consider  $J = 1$ ,  $K = 3$  and the length of the ladder is  $L = 25$ .

of flux strength  $\phi$  (see Fig. 5.13). As already inferred from Fig. 5.11, the overall slowing down of expansion is more significant in the case of staggered flux which can be seen from Fig. 5.13(b). For comparison we have also shown the case of  $\phi = 0$  in both Fig. 5.13 (a) and (b) where the curves don't exhibit any re-entrant behaviour. Interestingly, for very strong values of  $U$ , we see another re-entrant behaviour of  $V$  as a function of  $\phi$  in Fig. 5.13 for both the uniform and staggered flux cases. To clearly depict this behaviour, we plot  $V$  as a function of  $\phi/\pi$  for

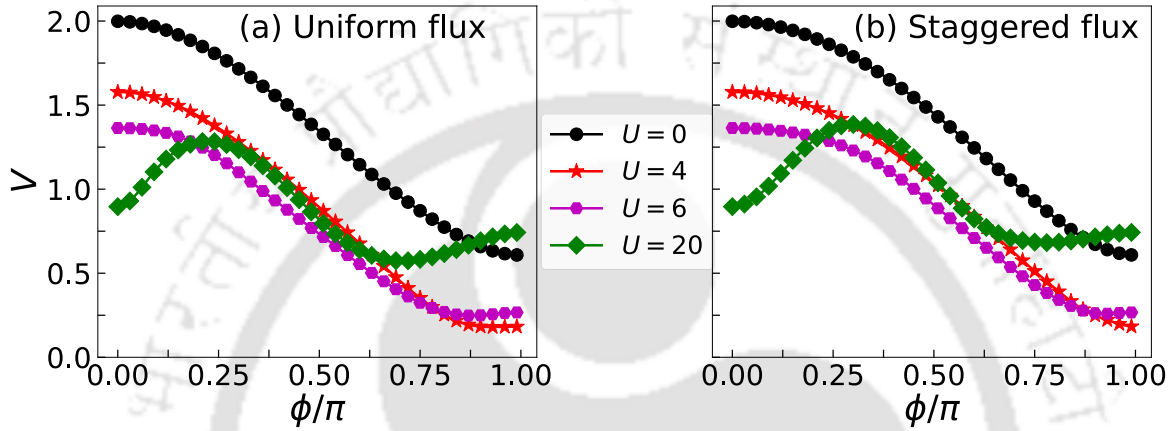


**Figure 5.14:** The figure shows the radial velocity  $V$  of the wavefunction as a function of  $\phi$  in the presence of (a) the uniform flux and (b) the staggered flux for different values of  $U$ . Here we consider  $J = 1$ ,  $K = 3$  and length of the ladder is  $L = 25$ .

different values of  $U$  in Fig. 5.14 (a) and (b) for both the uniform and staggered flux cases, respectively. It can be seen that while in the case of weak interaction, the radial velocity  $V$  decreases smoothly with flux strength  $\phi$ ; for stronger interaction strength i.e.  $U > 10$ , it first increases then falls down and then again rises up further with the flux strength  $\phi$ . This re-entrant feature can be attributed to the fermionization of the bosonic particles in the limit of strong interactions. Initially, in the limit of vanishing interaction, the particles are localized on the rung, where they are created due to the large rung hopping  $K$  and perform independent particle QW. For weak interactions, due to the finite overlap of the individual wavepackets at a single site, a weak repulsively bound pair can be formed which exhibits a slow spreading of density around the initial position [3, 27]. This behaviour is indicated by a bimodal distribution of density in Fig. 5.11 (IV-V) for both the uniform and staggered flux cases. From this analysis we confirm that the spreading of the density is suppressed due to increasing flux strength as well as the interaction strength, and it is dominant for the case of staggered flux. Note that this analysis is valid for both repulsive and attractive interactions (not shown).

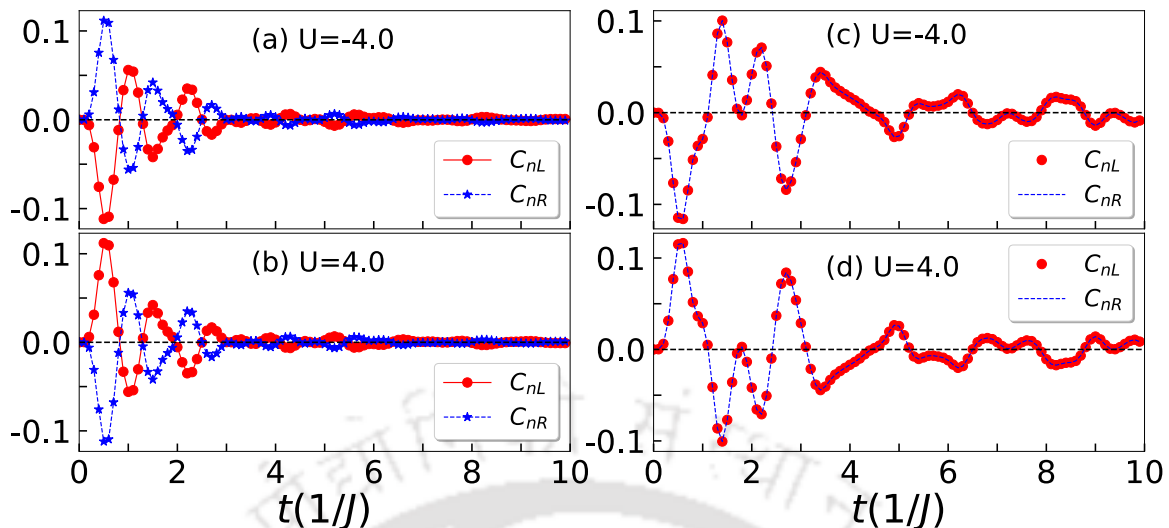


**Figure 5.15:** The chirality is plotted as a function of time. Figures (a) and (b) correspond to the uniform flux. Figures (c) and (d) correspond to the staggered flux. Here  $J = 1$ ,  $K = 3$ ,  $\phi = \frac{\pi}{4}$  and the length of the ladder is  $L = 25$ .

We now move ahead with the analysis of the chiral nature of the two-particle dynamics. As already discussed in Ref.[144], the two non-interacting particles ( $U = 0$ ) do not exhibit chiral motion in their QW due to the symmetric population in the chiral bands. In contrast, finite interactions break this symmetry and the chiral motion sets in. We calculate the chirality of the walker sitting on either side of the central rung using Eq. 5.6 similar to the case of single-particle QW and plot it in Fig. 5.15. Interestingly, this chiral motion of the particles moving to the left and to the right is not valid for both the types of flux. The chirality is present only when the uniform flux threading the ladder, and vanishes in the case of staggered flux. Note that the quantities  $C_{nR}$  and  $C_{nL}$  change their phase by  $\pi$ , depending on the sign of  $U$  [195]. To quantify the chirality in the presence of uniform flux, we calculate the shearing along the y-direction of the ladder  $Y_{CM}$  [3, 195] which is defined as;

$$Y_{CM} = N_R - N_L, \quad (5.10)$$

where

$$N_R = \frac{\sum_{i>0} n_{b,i} - n_{a,i}}{\sum_{i>0} n_{b,i} + n_{a,i}}, \quad (5.11)$$

$$N_L = \frac{\sum_{i<0} n_{b,i} - n_{a,i}}{\sum_{i<0} n_{b,i} + n_{a,i}}. \quad (5.12)$$

We plot  $Y_{CM}$  as a function of time for the case of repulsive and attractive  $U$  in the right and left panel respectively in Fig. 5.16. This shows that  $Y_{CM} = 0$  for

$U = 0$  (black circle), indicating that there is no chirality in the system. However, for  $U \neq 0$ , a finite value of  $Y_{CM}$  indicates the appearance of chirality in the system. On increasing the value of  $U$ , the amplitude of  $Y_{CM}$  gradually increases. There is a symmetry in  $Y_{CM}$  (i.e.  $Y_{CM}|_{+U} = -Y_{CM}|_{-U}$ ) is known as the symmetry protected dynamical symmetry [195].

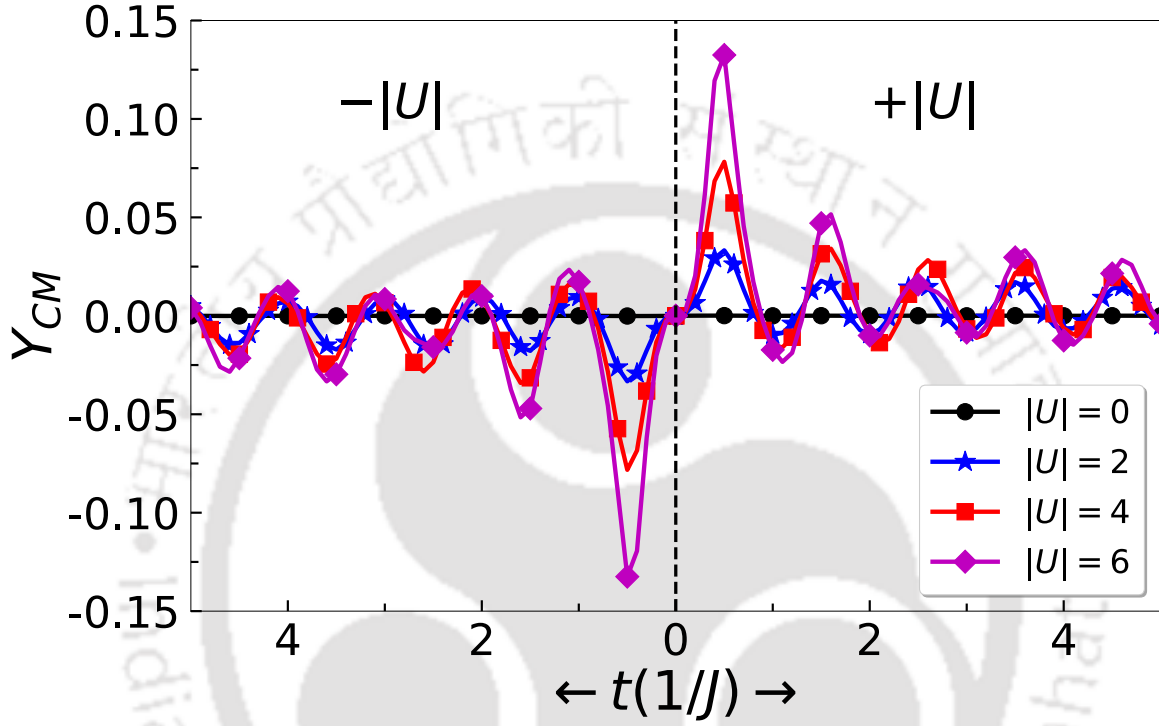


**Figure 5.16:** The shearing,  $Y_{CM}$  is plotted as a function of time for different repulsive and attractive interaction strengths. Here  $J = 1$ ,  $K = 3$ ,  $\phi = \frac{\pi}{4}$  and the length of the ladder is  $L = 25$ .

We investigate further on the change in the total particle density of the two legs compared to its average value. Our initial state defined in Eq. 5.9 is such that  $n_a = n_b = 1$ . Similar to the single-particle case, in this case also, we find a finite amount of fluctuation in the time evolution of total density for the staggered flux case which is absent in the case of uniform flux as depicted in Fig. 5.17. Note that similar to the behaviour of  $Y_{CM}$ , the particle densities  $n_a$  and  $n_b$  also possess symmetries with respect to  $U$  as

$$n_a|_{+U} = -n_a|_{-U} \quad \text{and} \quad n_b|_{+U} = -n_b|_{-U}. \quad (5.13)$$

In summary up to this point, we find that the staggered flux creates an imbalance in the particle density between the two legs of the ladder, whereas the uniform flux

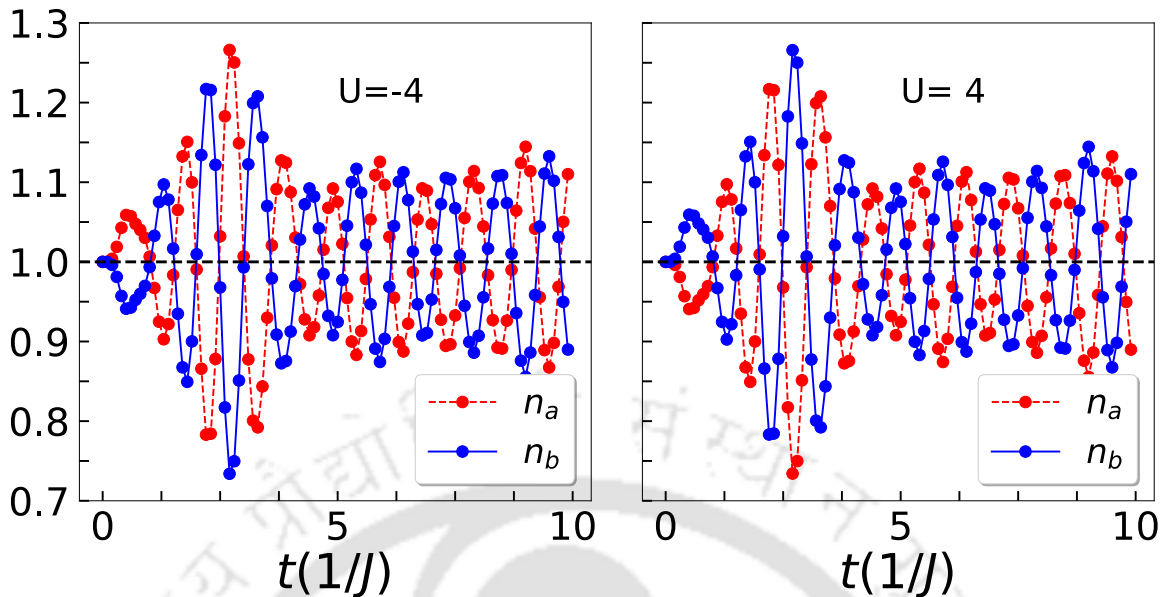


**Figure 5.17:** The figure shows the evolution of  $n_a$  and  $n_b$  defined in Eq. 5.8 for attractive and repulsive interaction strength. The symbols are for staggered flux case and the black dashed line is for uniform flux cases. Here  $J = 1$ ,  $K = 3$ ,  $\phi = \frac{\pi}{4}$  and the length of the ladder is  $L = 25$ .

creates chiral dynamics. The spreading of the walker for the staggered flux case slows down significantly as compared to the case of uniform flux.

To understand the dynamical behaviour due to the combined effect of the interaction and flux we analyse the energy eigenstates of the system in Fig. 5.18(a-c) and Fig. 5.18(d-f) for uniform and staggered flux cases, respectively. We also calculate the overlap of the initial state given in Eq. 5.9 with all the two particles energy eigenstates ( $\{|\chi_i\rangle\}$ ) of the Hamiltonian defined as

$$Overlap = \sum_i \langle \chi_i | \Psi_0 \rangle \quad (5.14)$$

and plot it as a function of  $\phi$  in Fig. 5.18. For  $U = 0$ , we get the continuum bands (S1, S2 and S3) for both uniform and staggered flux cases (Fig. 5.18 (a) and (d)). However, for finite interaction ( $U = 4$ ), three bound states (B1, B2 and B3) appear as a function of  $\phi$  among which B1 and B3 exhibit finite overlap with the initial state as shown in Fig. 5.18 (b) and (e). Note that B1 (B3) emerges at a small (large) value of  $\phi$  in the case of staggered flux as compared to the uniform flux. When the interaction is very strong, i.e.,  $U = 10$ , B3 completely get separated from the continuum for both the cases of flux and B1 appears at small values of  $\phi$  (Fig. 5.18 (c) and (f)). Due to the appearance of these bound states having finite

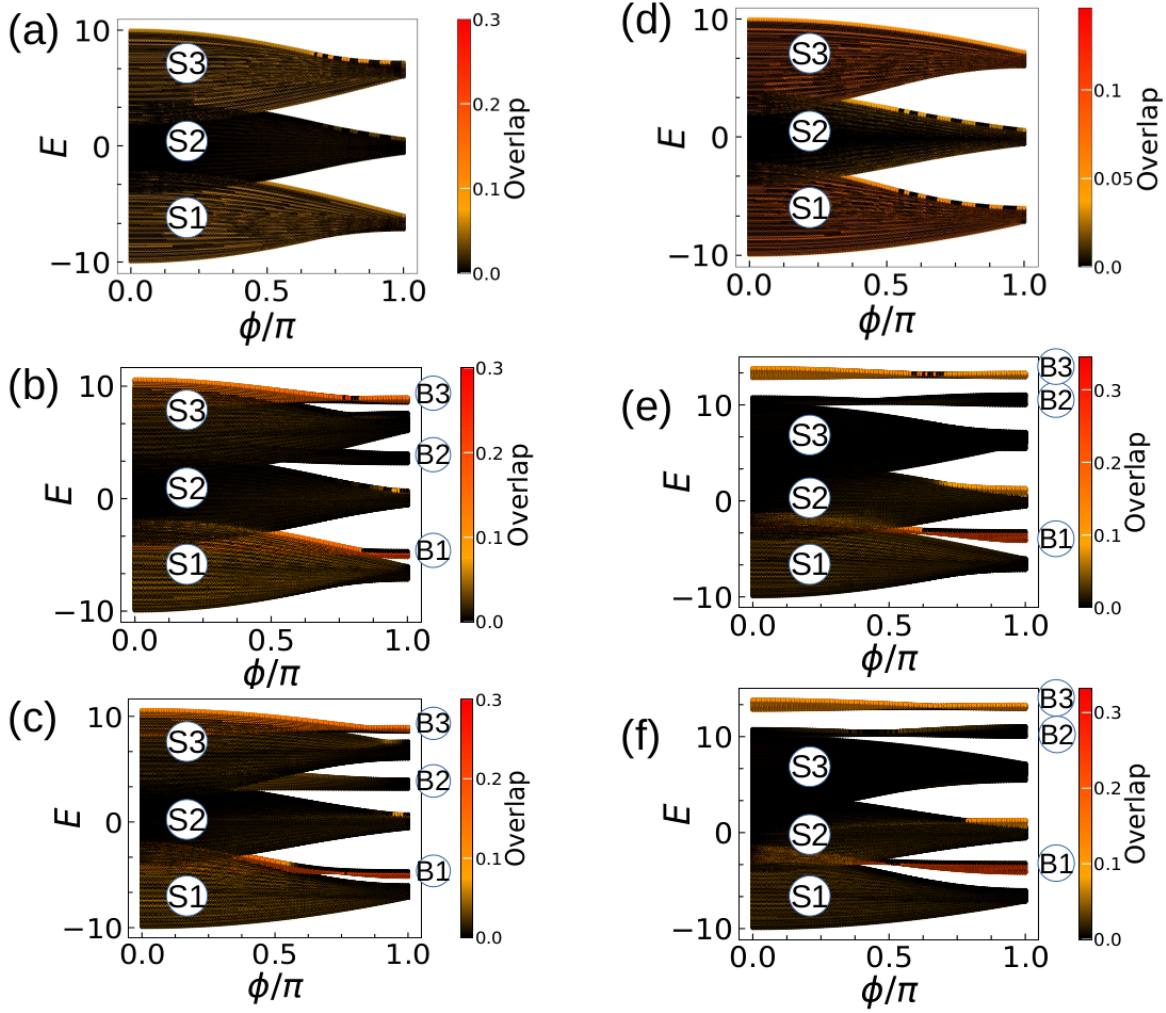


**Figure 5.18:** The figure shows the entire two particles energy spectrum of the ladder as a function of flux. The color scale represents the overlap of the initial state  $|\Psi_0\rangle = a_{a,0}^\dagger a_{b,0}^\dagger |vac\rangle$  with all the energy eigenstates of the system. Figures (a), (b) and (c) correspond to the uniform flux with  $U = 0, 4$  and  $10$ , respectively. Figures (c), (d) and (e) correspond to the staggered flux with  $U = 0, 4$  and  $10$ , respectively. Here we consider  $J = 1$ ,  $K = 3$  and length of the ladder is  $L = 25$ .

overlap with the initial state we get a slower dynamics in the QW of two interacting particles. This situation is similar to the one analyzed in Ref. [144].

## 5.4 Effect on Repulsively Bound Pairs

In this section, we perform the study of the effect of flux on the onsite bound pairs known as repulsively bound pairs (RBP) [2], which are usually seen at a large interaction limit (compared to the hopping strength) in standard Bose-Hubbard model. When the interaction strength is comparable to the hopping strength, there

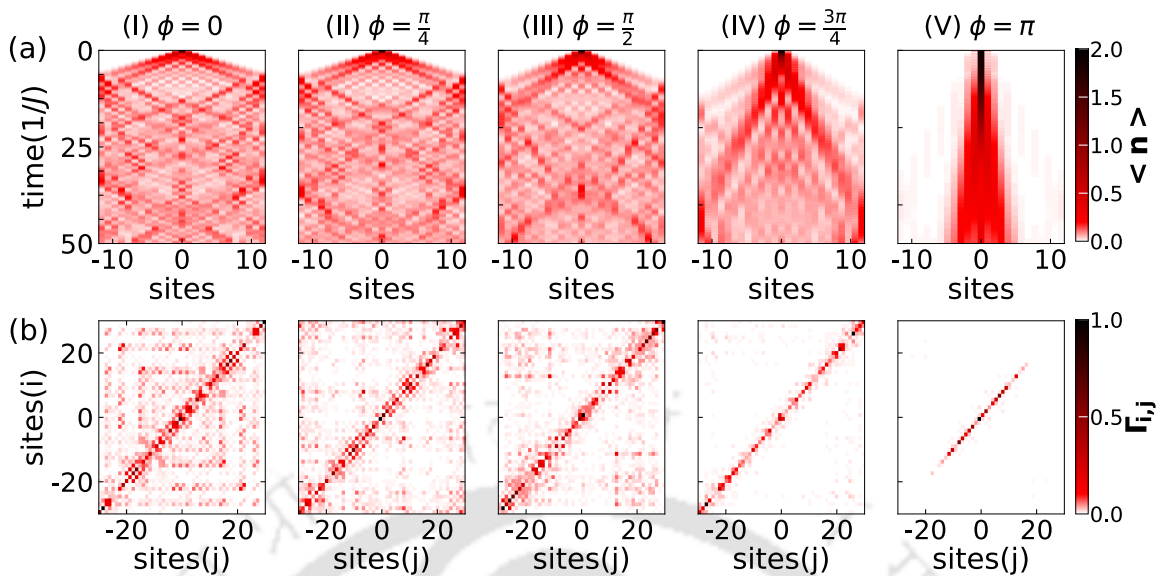


**Figure 5.19:** Panel (a) figure shows the density evolution of the initial state,  $|\Psi_0\rangle = (a_{a,0}^\dagger)^2|vac\rangle$  in the presences of the uniform flux. Panel (b) shows the corresponding two-particle correlation at time,  $t = 50(1/J)$ . Here  $J = 1$ ,  $K = 5$ ,  $U = 2$  and length of the ladder is  $L = 25$ .

is generally a small probability of forming the RBP [148]. However, similar to the lattice case, in the presence of the flux in the ladder, we see a significant increment in the probability of RBP formation. The interplay of flux and rung hopping plays an important role in the formation of RBP. The underlying physics behind this non-trivial effect on RBP is the separation of the band of bound states from the continuum band at large values of flux and rung hopping strength.

In the following we present our study on this intriguing physics by looking at the time evolution of the initial state and the energy spectrum of the Hamiltonian for the uniform flux case. The effect of staggered flux is qualitatively similar to the time evolution of the initial state for the case when two particles are sitting on a single site. The initial state is given by

$$|\psi_0\rangle = (a_{a,0}^\dagger)^2|vac\rangle \quad (5.15)$$

and the evolution of two-particle correlation can be written as

$$\Gamma_{i,j} = \langle a_i^\dagger a_j^\dagger a_j a_i \rangle \quad (5.16)$$

In this regard, we consider the onsite interaction strength  $U = 2$  which is comparable to the hopping strengths  $J = 1$  and  $K = 5$  and perform the evolution of the

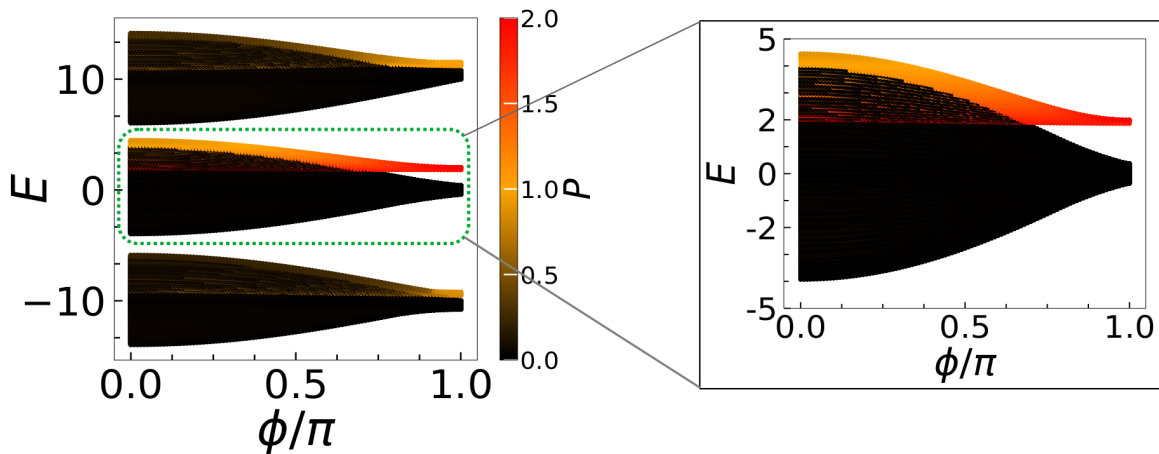


**Figure 5.20:** (a) The figure shows the energy spectrum as a function  $\phi/\pi$ . Here we consider  $J = 1$ ,  $K = 5$ ,  $U = 2$  and length of the ladder is  $L = 25$ .

state given in Eq. 5.15 for varying values of flux strength  $\phi$ . The evolution of the density with time and the two-particle correlation  $\Gamma_{i,j}$  at time  $t = 50$  are shown in Fig. 5.19 (a) and (b), respectively. The density evolution clearly shows that the evolution gets slower with the increase in flux strength. The two-particle correlation  $\Gamma_{i,j}$  plots indicate that there is a clear enhancement of the RBP at flux strengths  $\phi = \frac{3\pi}{4}$  and  $\phi = \pi$ , which can be inferred from the dominating diagonal elements of the correlation matrix.

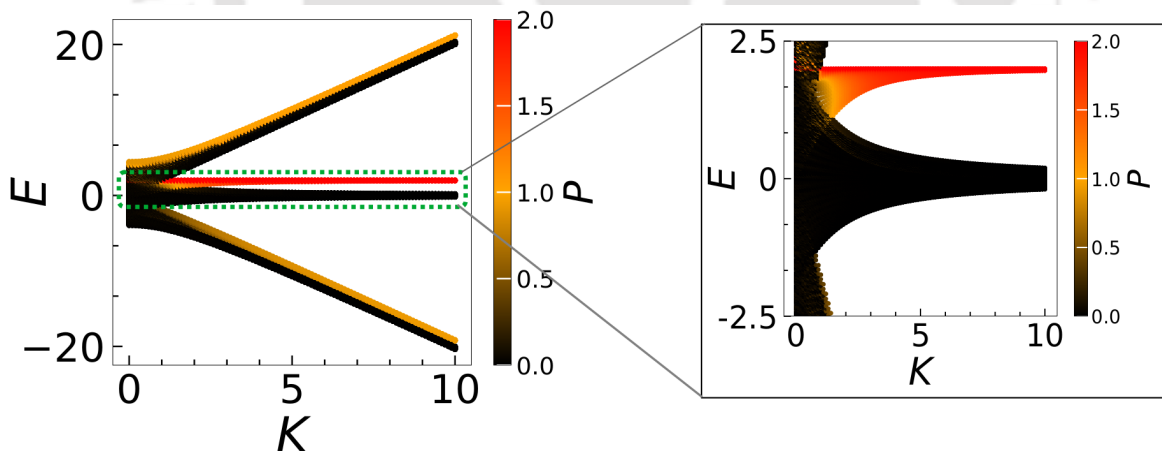


**Figure 5.21:** The figure shows the energy spectrum as a function of  $K$  at a flux strength,  $\phi = \pi$ . Here we consider  $J = 1$ ,  $U = 2$  and length of the ladder is  $L = 25$ .

The nontrivial effect on the formation of RBP can be further analyzed from the spectrum of the two-particle Hamiltonian (Eq. 5.1). In Fig. 5.20 we plot the energy spectrum with varying flux strength  $\phi$  by considering the onsite interaction strength  $U = 2$  and the rung hopping strength  $K = 5$ . We superimpose the spectrum with

the quantity

$$P = \sum_i \Gamma_{i,i} \quad (5.17)$$

which is the sum over the diagonal elements of the two-particle correlation matrix  $\Gamma_{i,j}$  for each eigenstates. Note that for completely paired states,  $P = 2$  and for scattered states,  $P = 0$ . It can be seen that there is a separation between the bound states and the scattered states for large values of flux strength  $\phi \sim \pi$ . The band-gap becomes of the order of the onsite interaction strength  $\sim U$ . This splitting of the spectrum results in the robustness of the RBP formation. We can also see that the bandwidth of the spectrum becomes smaller with flux strength  $\phi$  which is responsible for the slower density evolution in Fig. 5.19. Further to study the effect

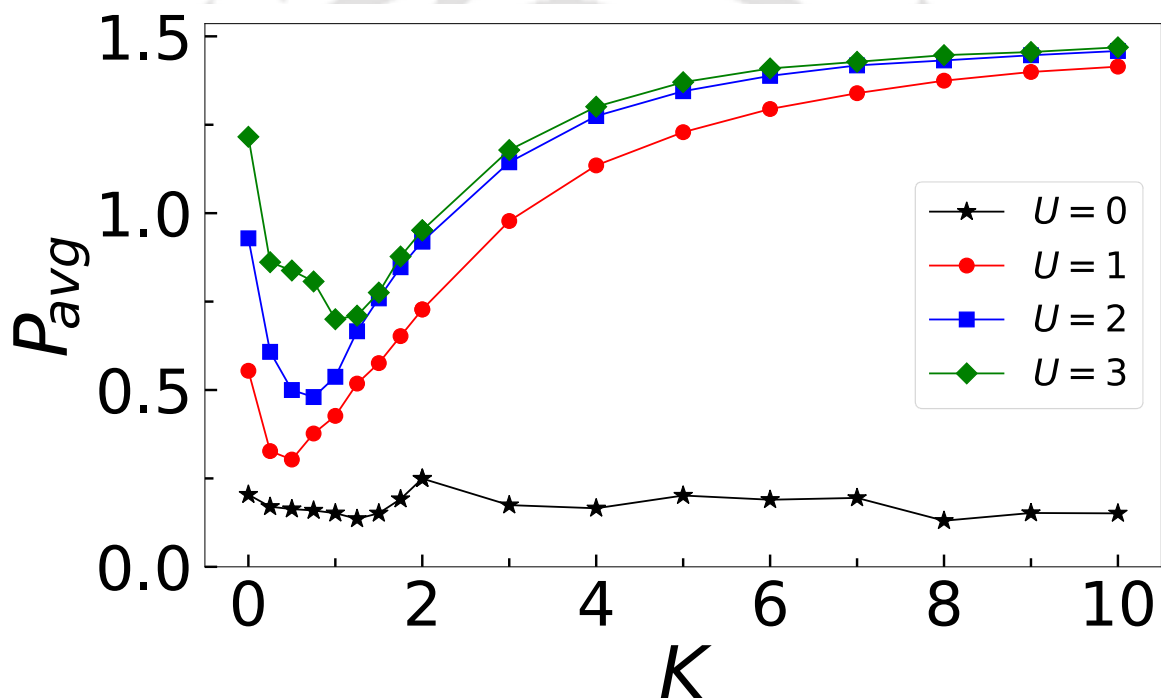


**Figure 5.22:** The figure shows  $P_{avg}$  plotted as a function of  $K$  for the initial state,  $|\Psi_0\rangle = (a_{a,0}^\dagger)^2|vac\rangle$  by taking the average of time between  $t = 90(1/J)$  and  $t = 100(1/J)$ . Here  $J = 1$ ,  $\phi = \pi$  and length of the ladder  $L = 25$ .

of the rung hopping strength  $K$  on the separation of the RBP band, we plot the energy spectrum at flux strength  $\phi = \pi$  with  $K$  for  $U = 2$  as shown in Fig. 5.21. With the increase in the rung hopping strength  $K$ , a band of bound states get separated from the scattered states with a band-gap  $\sim U$ . We also study the time evolution of the initial state shown in Eq. 5.15 for this case. In this context we plot  $P_{avg}$  as function of  $K$  for different values of  $U$  in Fig. 5.22 by taking the time average of  $P$  during the time evolution. We can clearly see that even for smaller values of  $U$ ,

$P_{avg}$  increases with an increase in  $K$  indicating that a large rung hopping strength  $K$  is crucial for enhancing the formation of RBP. Interestingly, for higher values of  $U$  (e.g.  $U = 3$ ), the formation of RBP is more favourable.

## 5.5 Conclusion

In this chapter, we have studied the CTQW for single and two particles in a two-leg ladder in the presence of a magnetic field. We consider two types of magnetic fields: the uniform flux and staggered flux threading the ladder. In the single-particle QW, the walker's speed slows down on increasing the flux strength. In the presence of the staggered flux, the slowing down is more significant as compared to the uniform flux. We have analyzed the QW of two interacting particles with an initial state where the two particles are located at the central rung and each site of the rung is occupied by one particle. We have found that the chiral motion present in the case of uniform flux vanishes when staggered flux threads the ladder. Besides the flux, we have shown that the interaction plays a crucial role in slowing down the walker speed in the two-particle QWs. Moreover, we have shown that the flux favours the formation of a repulsively bound pair when the initial state consists of two particles at the same site. Our work advances this emerging field by providing a general framework for studying chiral motion, particle fluctuation, and RBP in a wide variety of available experimental systems, including cold atoms, trapped ions, and photons.

## Chapter 6

# Summary and Outlook

In the thesis, we have studied the continuous time quantum walk (CTQW) to investigate various exciting physics in one-dimensional two-component systems.

In Chapter 1, first we provide a brief introduction to the QW, including the formal definition and explanation of both the discrete time as well as continuous time QW. Then we discuss the probability distribution of CTQW and CTRW in one-dimensional lattice. The probability distribution displays that the quantum walk is no longer a stochastic process like the classical random walk. The quantum walker's speed is also quadratically faster than its classical counterpart. We also discuss the multi-particle QW. Subsequently, we also discuss experimental possibilities to observe the QW for single and two-particle levels. At last, we discuss some of the relevant experimental progress in QW.

In Chapter 2, we provide the details of the numerical methods utilised to perform the thesis work. We employed the exact diagonalization (ED) method and the time-evolving block decimation (TEBD) methods for time evolution of a state.

In Chapter 3, we have studied the QW of a two-component system in the presence of interaction and hopping imbalance in a one-dimensional lattice. By considering different initial states depending on the positions of the particles ( $\uparrow$  and  $\downarrow$  where the  $\uparrow$  particle has higher hopping strength), we have analyzed the combined effect of hopping imbalance and inter-component interaction on the two-particle QW. We have found that when the two particles initially start from the central site of the lattice, the QW exhibits independent particle QWs to a QW of composite particles or doublon as a function of repulsive interactions. However, for the initial state with two particles at two different sites (a few sites apart), the  $\uparrow$  particle wave function is reflected from the  $\downarrow$  particle's wave function for large enough interactions, with no doublon is formed. On the other hand, when the two particles start from the opposite

ends of the lattice, the situation is completely different for strong interactions. In this case, both the  $\uparrow$  and  $\downarrow$  particle wave functions significantly reflect from each other at a point close to the initial position of the  $\downarrow$  particle. While we obtain different behavior compared to the many-body limit depending upon the parameters of the model Hamiltonian, the phenomenon of zero transmission in the limit of large inter-component interaction resembles the phase separation. These findings provide insights into the dynamical behavior of a mixture of two-component systems in periodic potential at the few particle levels.

In Chapter 4, we have studied the QW of two-component bosons with more than two particles in a one-dimensional lattice. We discuss the formation of the local bound states in the QWs of initially non-local bosons with only local interactions in the context of the two-component Bose-Hubbard model. We have shown that the non-trivial inter-component bound states called as doublon ( $\uparrow\downarrow$ ) can be formed at certain critical ratios of inter and intra-component interaction strengths. By considering three particles in total, an inter-component bound pair is formed when both intra- and inter-component interactions are of equal strength. However, when two particles from each component are considered, a stable triplon ( $\uparrow\downarrow\downarrow$ ) is formed when the inter-species interaction is half of the intra-species ones. Moreover, we have obtained that a finite hopping asymmetry between the components plays an important role in favouring a more stable inter-component bound pair. We have also shown that the QWs exhibit a re-entrant phenomenon as a function of the inter-component interaction.

In Chapter 5, we have studied the CTQW for single and two particles in a two-leg ladder in the presence of a magnetic field. We consider two types of magnetic fields: the uniform flux and staggered flux threading the ladder. In the single-particle QW, the walker's speed slows down on increasing the flux strength. In the presence of the staggered flux, the slowing down is more significant as compared to the uniform flux. We have analyzed the QW of two interacting particles with an initial state where the two particles are located at the central rung and each site of the rung is occupied by one particle. We have found that the chiral motion present in the case of uniform flux vanishes when staggered flux threads the ladder. Besides the flux, we have shown that the interaction plays a crucial role in slowing down the walker speed in the two-particle QWs. Moreover, we have shown that the flux favours the formation of repulsively bound pair when the initial state consists of two particles at the same site.

## 6.1 Outlook

The studied performed in this thesis work opens up new directions in the context of multi-component QW as well as the QW in presence of other perturbations such as magnetic field. All these findings are relevant in the context of quantum simulations of multi-component systems and due to the recent advancements in observing two-component dynamics and flux lattices can in principle lead to the successful observation of such findings. Moreover, these studies can be extended to various other scenarios where novel physics can be explored. Some of the possibilities as highlighted below.

It will be interesting to study the two component quantum walk of fermions in place of bosons and Bose-Fermi mixtures in one dimension. This will enable to investigate the combined effect of interaction and individual particle statistics in such complex systems. One can also extend these studies to explore the role of nearest neighbour interaction or disorder on the two component bound pair formation.

Another possibilities is to investigate the symmetry protected topological phase transitions in the two component systems such as Bose or Fermi Hubbard models using the QW. This will further enhance our understanding of the complex physics at the few particle level.

In recent years, the study of QW using the quantum computers have attracted a great deal of attention. Hence, it will be interesting to implement the two component QW discussed in the thesis to simulate them in the existing quantum devices.

Disorder induced phase transitions such as many-body localization can be understood from the wavepacket dynamics. While it is difficult to access the full many-body dynamics for a two-component system in presence of disorder, our studies on the two-component QW may be useful to have important insights on this.



# Bibliography

- [1] M. Greiner, O. Mandel, T. Esslinger, T. W. Hänsch, and I. Bloch, *Nature* **415**, 39 (2002).
- [2] K. Winkler et al., *Nature* **441**, 853 (2006).
- [3] P. M. Preiss et al., *Science* **347**, 1229 (2015).
- [4] L. E. Sadler, J. M. Higbie, S. R. Leslie, M. Vengalattore, and D. M. Stamper-Kurn, *Nature* **443**, 312 (2006).
- [5] J. P. Ronzheimer et al., *Phys. Rev. Lett.* **110**, 205301 (2013).
- [6] M. Cramer, A. Flesch, I. P. McCulloch, U. Schollwöck, and J. Eisert, *Phys. Rev. Lett.* **101**, 063001 (2008).
- [7] K. Sengupta, S. Powell, and S. Sachdev, *Phys. Rev. A* **69**, 053616 (2004).
- [8] C. Kollath, A. M. Läuchli, and E. Altman, *Phys. Rev. Lett.* **98**, 180601 (2007).
- [9] L. Vidmar, S. Langer, I. P. McCulloch, U. Schneider, U. Schollwöck, and F. Heidrich-Meisner, *Phys. Rev. B* **88**, 235117 (2013).
- [10] S. Langer, M. J. A. Schuetz, I. P. McCulloch, U. Schollwöck, and F. Heidrich-Meisner, *Phys. Rev. A* **85**, 043618 (2012).
- [11] K. Sengupta, D. Sen, and S. Mondal, *Phys. Rev. Lett.* **100**, 077204 (2008).
- [12] J. Ren, Y.-Z. Wu, and X.-F. Xu, *Scientific Reports* **5**, 14743 (2015).
- [13] E. Guardado-Sanchez, P. T. Brown, D. Mitra, T. Devakul, D. A. Huse, P. Schauß, and W. S. Bakr, *Phys. Rev. X* **8**, 021069 (2018).
- [14] Y. Aharonov, L. Davidovich, and N. Zagury, *Phys. Rev. A* **48**, 1687 (1993).
- [15] S. E. Venegas-Andraca, *Quantum Information Processing* **11**, 1015 (2012).
- [16] A. M. Childs, D. Gosset, and Z. Webb, *Science* **339**, 791 (2013).
- [17] A. M. Childs, *Phys. Rev. Lett.* **102**, 180501 (2009).
- [18] A. Ambainis, A. Bačkurs, N. Nahimovs, R. Ozols, and A. Rivosh, Search by quantum walks on two-dimensional grid without amplitude amplification, in *Theory of Quantum Computation, Communication, and Cryptography*, edited by K. Iwama, Y. Kawano, and M. Murao, pages 87–97, Berlin, Heidelberg, 2013, Springer Berlin Heidelberg.
- [19] A. Ambainis, A. Backurs, N. Nahimovs, R. Ozols, and A. Rivosh, arXiv e-prints , arXiv:1112.3337 (2011).
- [20] N. B. Lovett, S. Cooper, M. Everitt, M. Trevers, and V. Kendon, *Phys. Rev. A* **81**, 042330 (2010).

## BIBLIOGRAPHY

---

- [21] M. S. Underwood and D. L. Feder, *Phys. Rev. A* **82**, 042304 (2010).
- [22] E. Farhi and S. Gutmann, *Phys. Rev. A* **58**, 915 (1998).
- [23] A. Ambainis, Quantum walk algorithm for element distinctness, in *45th Annual IEEE Symposium on Foundations of Computer Science*, pages 22–31, 2004.
- [24] A. Ambainis, *International Journal of Quantum Information* **01**, 507 (2003).
- [25] N. Shenvi, J. Kempe, and K. B. Whaley, *Phys. Rev. A* **67**, 052307 (2003).
- [26] R. Yao and J. Zakrzewski, arXiv:2007.04745 (2020).
- [27] D. Wiater, T. Sowiński, and J. Zakrzewski, *Phys. Rev. A* **96**, 043629 (2017).
- [28] P. M. Preiss et al., *Science* **347**, 1229 (2015).
- [29] D. L. Shepelyansky, *Phys. Rev. Lett.* **73**, 2607 (1994).
- [30] H. Schmitz, R. Matjeschk, C. Schneider, J. Glueckert, M. Enderlein, T. Huber, and T. Schaetz, *Phys. Rev. Lett.* **103**, 090504 (2009).
- [31] F. Zähringer, G. Kirchmair, R. Gerritsma, E. Solano, R. Blatt, and C. F. Roos, *Phys. Rev. Lett.* **104**, 100503 (2010).
- [32] M. Karski, L. Förster, J.-M. Choi, A. Steffen, W. Alt, D. Meschede, and A. Widera, *Science* **325**, 174 (2009).
- [33] T. Fukuhara, P. Schauß, M. Endres, S. Hild, M. Cheneau, I. Bloch, and C. Gross, *Nature* **502**, 76 EP (2013).
- [34] K. Manouchehri and J. Wang, *Physical Implementation of Quantum Walks*, Springer (2014).
- [35] S. Hoyer, M. Sarovar, and K. B. Whaley, *New Journal of Physics* **12**, 065041 (2010).
- [36] M. Mohseni, P. Rebentrost, S. Lloyd, and A. Aspuru-Guzik, *The Journal of Chemical Physics* **129**, 174106 (2008).
- [37] A. F. Ghoniem and F. S. Sherman, *Journal of Computational Physics* **61**, 1 (1985).
- [38] H. C. Berg, *Random Walks in Biology*, 1993.
- [39] E. F. Fama, *Financial Analysts Journal* **51**, 75 (1995).
- [40] R. Motwani and P. Raghavan, *Randomized algorithms*, Cambridge university press, 1995.
- [41] A. Ambainis, *International Journal of Quantum Information* **01**, 507 (2003).
- [42] J. Kempe, *Contemporary Physics* **44**, 307–327 (2003).
- [43] A. M. Childs and J. Goldstone, *Phys. Rev. A* **70**, 022314 (2004).
- [44] M. Schuld, I. Sinayskiy, and F. Petruccione, *Quantum Information Processing* **13**, 2567 (2014).
- [45] E. Sánchez-Burillo, J. Duch, J. Gómez-Gardeñes, and D. Zueco, *Scientific Reports* **2**, 605 (2012).
- [46] O. Mülken and A. Blumen, *Physics Reports* **502**, 37 (2011).
- [47] O. Mülken and A. Blumen, *Phys. Rev. E* **73**, 066117 (2006).
- [48] R. Portugal, *Quantum Walks and Search Algorithms*, Quantum Science and Technology, Springer New York, 2013.
- [49] K. Manouchehri and J. Wang, *Physical Implementation of Quantum Walks*, Quantum Science and Technology, Springer Berlin Heidelberg, 2013.
- [50] S. Chakraborty, L. Novo, A. Ambainis, and Y. Omar, *Phys. Rev. Lett.* **116**, 100501

- (2016).
- [51] T. G. Wong, L. Tarrataca, and N. Nahimov, *Quantum Information Processing* **15**, 4029 (2016).
- [52] G. ABAL, R. DONANGELO, F. L. MARQUEZINO, and R. PORTUGAL, *Mathematical Structures in Computer Science* **20**, 999–1009 (2010).
- [53] I. Foulger, S. Gnutzmann, and G. Tanner, *Phys. Rev. A* **91**, 062323 (2015).
- [54] A. M. Childs and Y. Ge, *Phys. Rev. A* **89**, 052337 (2014).
- [55] G. S. Engel et al., *Nature* **446**, 782 (2007).
- [56] N. Lambert, Y.-N. Chen, Y.-C. Cheng, C.-M. Li, G.-Y. Chen, and F. Nori, *Nature Physics* **9**, 10 (2013).
- [57] M. Christandl, N. Datta, A. Ekert, and A. J. Landahl, *Phys. Rev. Lett.* **92**, 187902 (2004).
- [58] V. M. Kendon and C. Tamon, *Journal of Computational and Theoretical Nanoscience* **8**, 422 (2011).
- [59] R. Alvir, S. Dever, B. Lovitz, J. Myer, C. Tamon, Y. Xu, and H. Zhan, *J. Algebraic Comb.* **43**, 801–826 (2016).
- [60] A. Joye and M. Merkli, *Journal of Statistical Physics* **140**, 1025 (2010).
- [61] Y. Shikano and H. Katsura, *Phys. Rev. E* **82**, 031122 (2010).
- [62] C. M. Chandrashekar, *Phys. Rev. A* **83**, 022320 (2011).
- [63] A. P. Schnyder, S. Ryu, A. Furusaki, and A. W. W. Ludwig, *Phys. Rev. B* **78**, 195125 (2008).
- [64] T. Kitagawa, M. S. Rudner, E. Berg, and E. Demler, *Phys. Rev. A* **82**, 033429 (2010).
- [65] J. K. Asbóth and H. Obuse, *Phys. Rev. B* **88**, 121406 (2013).
- [66] Y. Lahini, M. Verbin, S. D. Huber, Y. Bromberg, R. Pugatch, and Y. Silberberg, *Phys. Rev. A* **86**, 011603 (2012).
- [67] A. Ahlbrecht, A. Alberti, D. Meschede, V. B. Scholz, A. H. Werner, and R. F. Werner, *New Journal of Physics* **14**, 073050 (2012).
- [68] A. Crespi et al., *Nature Photonics* **7**, 322 (2013).
- [69] K. Manouchehri and J. B. Wang, *Journal of Physics A: Mathematical and Theoretical* **40**, 13773 (2007).
- [70] J. Du, H. Li, X. Xu, M. Shi, J. Wu, X. Zhou, and R. Han, *Phys. Rev. A* **67**, 042316 (2003).
- [71] R. Côté, A. Russell, E. E. Eyler, and P. L. Gould, *New Journal of Physics* **8**, 156 (2006).
- [72] A. Peruzzo et al., *Science* **329**, 1500 (2010).
- [73] K. Poulios et al., *Phys. Rev. Lett.* **112**, 143604 (2014).
- [74] H. Tang et al., *Science Advances* **4**, eaat3174 (2018).
- [75] Q.-P. Su et al., *npj Quantum Information* **5**, 40 (2019).
- [76] Y. Ye et al., *Phys. Rev. Lett.* **123**, 050502 (2019).
- [77] Z. Yan et al., *Science* **364**, 753 (2019).
- [78] M. P. A. Fisher, P. B. Weichman, G. Grinstein, and D. S. Fisher, *Phys. Rev. B* **40**,

## BIBLIOGRAPHY

---

- 546 (1989).
- [79] D. Jaksch, C. Bruder, J. I. Cirac, C. W. Gardiner, and P. Zoller, *Phys. Rev. Lett.* **81**, 3108 (1998).
- [80] H. Feshbach, *Annals of Physics* **5**, 357 (1958).
- [81] E. A. Donley, N. R. Claussen, S. T. Thompson, and C. E. Wieman, *Nature* **417**, 529 (2002).
- [82] K. Xu, T. Mukaiyama, J. Abo-Shaeer, J. K. Chin, D. Miller, and W. Ketterle, *Physical review letters* **91**, 210402 (2003).
- [83] C. A. Regal, C. Ticknor, J. L. Bohn, and D. S. Jin, *Nature* **424**, 47 (2003).
- [84] C. Chin, R. Grimm, P. Julienne, and E. Tiesinga, *Rev. Mod. Phys.* **82**, 1225 (2010).
- [85] L. Bonnes and S. Wessel, *Phys. Rev. Lett.* **106**, 185302 (2011).
- [86] Y. Bromberg, Y. Lahini, R. Morandotti, and Y. Silberberg, *Phys. Rev. Lett.* **102**, 253904 (2009).
- [87] L. Sansoni, F. Sciarrino, G. Vallone, P. Mataloni, A. Crespi, R. Ramponi, and R. Osellame, *Phys. Rev. Lett.* **108**, 010502 (2012).
- [88] M. A. Broome, A. Fedrizzi, S. Rahimi-Keshari, J. Dove, S. Aaronson, T. C. Ralph, and A. G. White, *Science* **339**, 794 (2013).
- [89] J. B. Spring et al., *Science* **339**, 798 (2013).
- [90] M. Tillmann, B. Dakic, R. Heilmann, S. Nolte, A. Szameit, and P. Walther, *Nature Photonics* **7**, 540 EP (2013).
- [91] A. Crespi et al., *Nature Photonics* **7**, 545 EP (2013).
- [92] X. Qin, Y. Ke, X. Guan, Z. Li, N. Andrei, and C. Lee, *Phys. Rev. A* **90**, 062301 (2014).
- [93] A. Ahlbrecht, A. Alberti, D. Meschede, V. B. Scholz, A. H. Werner, and R. F. Werner, *New Journal of Physics* **14**, 073050 (2012).
- [94] S. Mondal and T. Mishra, *Phys. Rev. A* **101** (2020).
- [95] I. Siloi, C. Benedetti, E. Piccinini, J. Piilo, S. Maniscalco, M. G. A. Paris, and P. Bordone, *Phys. Rev. A* **95**, 022106 (2017).
- [96] Y. Lahini, M. Verbin, S. D. Huber, Y. Bromberg, R. Pugatch, and Y. Silberberg, *Phys. Rev. A* **86**, 011603 (2012).
- [97] F. Zähringer, G. Kirchmair, R. Gerritsma, E. Solano, R. Blatt, and C. Roos, *Phys. Rev. Lett.* **104**, 100503 (2010).
- [98] J. Vijayan et al., *Science* **367**, 186 (2020).
- [99] T. Kitagawa et al., *Nature Communications* **3**, 882 (2012).
- [100] I. Dimitrova, N. Jepsen, A. Buyskikh, A. Venegas-Gomez, J. Amato-Grill, A. Daley, and W. Ketterle, *Phys. Rev. Lett.* **124**, 043204 (2020).
- [101] P. Wrzosek, K. Wohlfeld, D. Hofmann, T. Sowiński, and M. A. Sentef, *Phys. Rev. B* **102**, 024440 (2020).
- [102] M. Taglieber, A.-C. Voigt, T. Aoki, T. W. Hänsch, and K. Dieckmann, *Phys. Rev. Lett.* **100**, 010401 (2008).
- [103] E. Wille et al., *Phys. Rev. Lett.* **100**, 053201 (2008).

- [104] S. Ospelkaus, C. Ospelkaus, O. Wille, M. Succo, P. Ernst, K. Sengstock, and K. Bongs, *Phys. Rev. Lett.* **96**, 180403 (2006).
- [105] K. Günter, T. Stöferle, H. Moritz, M. Köhl, and T. Esslinger, *Phys. Rev. Lett.* **96**, 180402 (2006).
- [106] T. Best, S. Will, U. Schneider, L. Hackermüller, D. van Oosten, I. Bloch, and D.-S. Lühmann, *Phys. Rev. Lett.* **102**, 030408 (2009).
- [107] J. Catani, L. De Sarlo, G. Barontini, F. Minardi, and M. Inguscio, *Phys. Rev. A* **77**, 011603 (2008).
- [108] B. Gadway, D. Pertot, R. Reimann, and D. Schneble, *Phys. Rev. Lett.* **105**, 045303 (2010).
- [109] E. Altman, W. Hofstetter, E. Demler, and M. D. Lukin, *New Journal of Physics* **5**, 113 (2003).
- [110] A. Isacsson, M.-C. Cha, K. Sengupta, and S. M. Girvin, *Phys. Rev. B* **72**, 184507 (2005).
- [111] L.-M. Duan, E. Demler, and M. D. Lukin, *Phys. Rev. Lett.* **91**, 090402 (2003).
- [112] P. P. Orth, I. Stanic, and K. Le Hur, *Phys. Rev. A* **77**, 051601 (2008).
- [113] W. Wang, V. Penna, and B. Capogrosso-Sansone, *New Journal of Physics* **18**, 063002 (2016).
- [114] L. Mathey, *Phys. Rev. B* **75**, 144510 (2007).
- [115] T. Mishra, R. V. Pai, and B. P. Das, *Phys. Rev. A* **76**, 013604 (2007).
- [116] M. Singh, S. Mondal, B. K. Sahoo, and T. Mishra, *Phys. Rev. A* **96**, 053604 (2017).
- [117] N. H. Le, A. J. Fisher, N. J. Curson, and E. Ginossar, *npj Quantum Information* **6**, 24 (2020).
- [118] L. Barbiero, L. Santos, and N. Goldman, *Phys. Rev. B* **97**, 201115 (2018).
- [119] S. Mondal, S. Greschner, L. Santos, and T. Mishra, *arXiv:2008.07224* (2020).
- [120] B.-T. Ye, L.-Z. Mu, and H. Fan, *Phys. Rev. B* **94**, 165167 (2016).
- [121] O. Mandel, M. Greiner, A. Widera, T. Rom, T. W. Hänsch, and I. Bloch, *Phys. Rev. Lett.* **91**, 010407 (2003).
- [122] P. Soltan-Panahi et al., *Nature Physics* **7**, 434 (2011).
- [123] B. Yang, H.-N. Dai, H. Sun, A. Reingruber, Z.-S. Yuan, and J.-W. Pan, *Phys. Rev. A* **96**, 011602 (2017).
- [124] G. Jotzu, M. Messer, F. Görg, D. Greif, R. Desbuquois, and T. Esslinger, *Phys. Rev. Lett.* **115**, 073002 (2015).
- [125] N. D. Oppong, G. Pasqualetti, O. Bettermann, P. Zechmann, M. Knap, I. Bloch, and S. Fölling, *arXiv:2011.12411* (2020).
- [126] C. F. Roos, A. Alberti, D. Meschede, P. Hauke, and H. Häffner, *Phys. Rev. Lett.* **119**, 160401 (2017).
- [127] L. Sansoni, F. Sciarrino, G. Vallone, P. Mataloni, A. Crespi, R. Ramponi, and R. Osellame, *Phys. Rev. Lett.* **108**, 010502 (2012).
- [128] M. Aidelsburger, *Journal of Physics B: Atomic, Molecular and Optical Physics* **51**, 193001 (2018).

## BIBLIOGRAPHY

---

- [129] S. Sarkar and T. Sowiński, arXiv (2020).
- [130] J. M. Zhang and R. X. Dong, *European Journal of Physics* **31**, 591 (2010).
- [131] G. Vidal, *Phys. Rev. Lett.* **93**, 040502 (2004).
- [132] U. Schollwöck, *Annals of Physics* **326**, 96 (2011).
- [133] M. Suzuki, *Progress of Theoretical Physics* **56**, 1454 (1976).
- [134] H. F. Trotter, *P. Am. Math. Soc* **10**, 545 (1959).
- [135] P. Calabrese and J. Cardy, *Journal of Statistical Mechanics: Theory and Experiment* **2005**, P04010 (2005).
- [136] M. L. Wall and L. D. Carr, *New Journal of Physics* **14**, 125015 (2012).
- [137] D. Jaschke, M. L. Wall, and L. D. Carr, *Computer Physics Communications* **225**, 59–91 (2018).
- [138] J. Kempe, *Contemporary Physics* **44**, 307–327 (2003).
- [139] A. M. Childs, E. Farhi, and S. Gutmann, *Quantum Information Processing* **1**, 35–43 (2002).
- [140] J. Ren, Y.-Z. Wu, and X.-F. Xu, *Scientific Reports* **5**, 14743 (2015).
- [141] T. Sowiński and M. Á. García-March, *Reports on Progress in Physics* **82**, 104401 (2019).
- [142] R. M. Kalas, A. V. Balatsky, and D. Mozyrsky, *Phys. Rev. B* **78**, 184513 (2008).
- [143] L.-M. Duan, E. Demler, and M. D. Lukin, *Phys. Rev. Lett.* **91**, 090402 (2003).
- [144] W. S. Bakr et al., *Science* **329**, 547 (2010).
- [145] H. Cayla et al., *Phys. Rev. Lett.* **125**, 165301 (2020).
- [146] Z. Yan et al., *Science* **364**, 753 (2019).
- [147] W. S. Dias, E. M. Nascimento, M. L. Lyra, and F. A. B. F. de Moura, *Phys. Rev. B* **76**, 155124 (2007).
- [148] M. K. Giri, S. Mondal, B. P. Das, and T. Mishra, *Scientific Reports* **11**, 22056 (2021).
- [149] A. Peixoto and W. Dias, *Solid State Communications* **242**, 68 (2016).
- [150] G. Vidal, *Phys. Rev. Lett.* **91**, 147902 (2003).
- [151] G. Vidal, *Phys. Rev. Lett.* **93**, 040502 (2004).
- [152] A. B. Kuklov and B. V. Svistunov, *Phys. Rev. Lett.* **90**, 100401 (2003).
- [153] S. Mondal, S. Greschner, L. Santos, and T. Mishra, *Phys. Rev. A* **104**, 013315 (2021).
- [154] F. H. L. Essler, H. Frahm, F. Göhmann, A. Klümper, and V. E. Korepin, *The One-Dimensional Hubbard Model*, Cambridge University Press, 2005.
- [155] M. Gärttner, A. Safavi-Naini, J. Schachenmayer, and A. M. Rey, *Phys. Rev. A* **100**, 053607 (2019).
- [156] S. Scherg et al., *Phys. Rev. Lett.* **121**, 130402 (2018).
- [157] M. Azuma, Z. Hiroi, M. Takano, K. Ishida, and Y. Kitaoka, *Phys. Rev. Lett.* **73**, 3463 (1994).
- [158] E. Dagotto, *Reports on Progress in Physics* **62**, 1525 (1999).
- [159] M. Atala, M. Aidelsburger, M. Lohse, J. T. Barreiro, B. Paredes, and I. Bloch, *Nature Physics* **10**, 588 (2014).

- [160] X. Li, E. Zhao, and W. Vincent Liu, *Nature Communications* **4**, 1523 (2013).
- [161] E. Orignac and T. Giamarchi, *Phys. Rev. B* **57**, 11713 (1998).
- [162] E. Orignac and T. Giamarchi, *Phys. Rev. B* **64**, 144515 (2001).
- [163] P. Donohue and T. Giamarchi, *Phys. Rev. B* **63**, 180508 (2001).
- [164] I. Danshita, C. A. R. Sá de Melo, and C. W. Clark, *Phys. Rev. A* **77**, 063609 (2008).
- [165] M. S. Luthra, T. Mishra, R. V. Pai, and B. P. Das, *Phys. Rev. B* **78**, 165104 (2008).
- [166] Y.-J. Lin, R. L. Compton, K. Jiménez-García, J. V. Porto, and I. B. Spielman, *Nature* **462**, 628 (2009).
- [167] A. Celi, P. Massignan, J. Ruseckas, N. Goldman, I. B. Spielman, G. Juzeliūnas, and M. Lewenstein, *Phys. Rev. Lett.* **112**, 043001 (2014).
- [168] M. Aidelsburger, M. Atala, S. Nascimbène, S. Trotzky, Y.-A. Chen, and I. Bloch, *Phys. Rev. Lett.* **107**, 255301 (2011).
- [169] M. Aidelsburger, M. Atala, M. Lohse, J. T. Barreiro, B. Paredes, and I. Bloch, *Phys. Rev. Lett.* **111**, 185301 (2013).
- [170] H. Miyake, G. A. Siviloglou, C. J. Kennedy, W. C. Burton, and W. Ketterle, *Phys. Rev. Lett.* **111**, 185302 (2013).
- [171] M. Aidelsburger et al., *Nature Physics* **11**, 162 (2015).
- [172] S. T. Carr, B. N. Narozhny, and A. A. Nersesyan, *Phys. Rev. B* **73**, 195114 (2006).
- [173] M. Iskin, *The European Physical Journal B* **85**, 1 (2012).
- [174] M. Iskin, *Physical Review A* **93**, 033632 (2016).
- [175] M. Iskin, *Phys. Rev. A* **96**, 043628 (2017).
- [176] N. Goldman, J. Beugnon, and F. Gerbier, *Phys. Rev. Lett.* **108**, 255303 (2012).
- [177] N. Goldman, J. Dalibard, A. Dauphin, F. Gerbier, M. Lewenstein, P. Zoller, and I. B. Spielman, *Proceedings of the National Academy of Sciences* **110**, 6736 (2013).
- [178] D. Hugel and B. Paredes, *Physical Review A* **89**, 023619 (2014).
- [179] A. Sterdyniak, B. A. Bernevig, N. R. Cooper, and N. Regnault, *Physical Review B* **91**, 035115 (2015).
- [180] A. Dhar, M. Maji, T. Mishra, R. V. Pai, S. Mukerjee, and A. Paramekanti, *Phys. Rev. A* **85**, 041602 (2012).
- [181] A. Dhar, T. Mishra, M. Maji, R. V. Pai, S. Mukerjee, and A. Paramekanti, *Phys. Rev. B* **87**, 174501 (2013).
- [182] A. Petrescu and K. Le Hur, *Physical Review Letters* **111**, 150601 (2013).
- [183] A. Petrescu and K. Le Hur, *Physical Review B* **91**, 054520 (2015).
- [184] A. Tokuno and A. Georges, *New Journal of Physics* **16**, 073005 (2014).
- [185] T. Mishra, S. Greschner, and L. Santos, *New Journal of Physics* **18**, 045016 (2016).
- [186] R. Sachdeva, F. Metz, M. Singh, T. Mishra, and T. Busch, *Phys. Rev. A* **98**, 063612 (2018).
- [187] M. P. Zaletel, S. Parameswaran, A. Rüegg, and E. Altman, *Physical Review B* **89**, 155142 (2014).
- [188] S. Greschner, G. Sun, D. Poletti, and L. Santos, *Physical review letters* **113**, 215303 (2014).
- [189] S. Greschner, D. Huerga, G. Sun, D. Poletti, and L. Santos, *Physical Review B* **92**,

## BIBLIOGRAPHY

---

- 115120 (2015).
- [190] S. Greschner, M. Piraud, F. Heidrich-Meisner, I. McCulloch, U. Schollwöck, and T. Vekua, *Physical Review A* **94**, 063628 (2016).
- [191] R. Sachdeva, M. Singh, and T. Busch, *Phys. Rev. A* **95**, 063601 (2017).
- [192] M. Piraud, F. Heidrich-Meisner, I. P. McCulloch, S. Greschner, T. Vekua, and U. Schollwoeck, *Physical Review B* **91**, 140406 (2015).
- [193] S. Mondal, A. Kshetrimayum, and T. Mishra, *Phys. Rev. A* **102**, 023312 (2020).
- [194] M. E. Tai et al., *Nature* **546**, 519 (2017).
- [195] J. Yu, N. Sun, and H. Zhai, *Phys. Rev. Lett.* **119**, 225302 (2017).



## Curriculum Vitae

### Address

Home Address : Purba Birampur, Boroj, Purba Medinipur, West Bengal, India

Phone : +91 7699795537

Email : mrinalphy333@gmail.com

### Personal profile

Date of Birth : 05/09/1994

Gender : Male

Marital Status : Unmarried

Nationality : Indian

Language : Bengali, English, Hindi

### Education

B.Sc (2011-2014) : Midnapore College, Vidyasagar University, India

B.Ed (2014-2015) : Maharshi Dayanand University, Rohtak, India

M.Sc (2016-2018) : Indian Institute of Technology - Guwahati (IIT-Guwahati), India

Ph.D (Enrolled in 2018) : Indian Institute of Technology Guwahati

Earned the Senior Research Fellowship in 2020 by Indian Institute of Technology Guwahati.

Graduate Aptitude Test in Engineering (GATE) qualified in 2018.

National Eligibility Test (NET) qualified in 2018(CSIR Fellow).